Modeling a Circulating Fluidized Bed $CaCO_3$ Calcination Reactor for Thermochemical Energy Storage in a Concentrating Solar Power System

Mayra Del Valle Alvarez Rivero

Thesis to obtain the Master of Science Degree in

Energy Engineering and Management

Supervisors: Prof. Luís Filipe Moreira Mendes

Eng. João Pereira Cardoso

Examination Committee

Chairperson: Prof. Name

Supervisor: Prof. Luís Filipe Moreira Mendes

Members of Committee: Prof. Name

: Prof. Name

December 2020

“The arrival time of a space probe traveling to Saturn can be predicted more accurately than the behavior of a fluidized bed chemical reactor!”

Geldart, 1986

Acknowledgments

I would like to thank and express my deepest appreciation to my supervisors, Prof. Filipe Mendes and Eng. João Cardoso, for their guidance, and expertise during the development of this thesis. To Prof. Filipe, I express my gratitude for his dedication, patience, and especially for his support when developing the proposed model. To Engº João Cardoso I express my gratitude for your support and search skills for finding an answer when there seems to be none. To both thank you for this time and for educating me not only on this field but in the arts of music.

I would like to thank also Prof. Carla Pinheiro, Prof. Henrique Matos, and Dr. Paula Texeira for their advice and guidance during this study. Your availability for this project and your final suggestions for improving this work are deeply appreciated.

I would like to thank InnoEnergy for supporting me financially during this journey and for the education that I have been provided at the Silesian University of Technology in Poland and Instituto Superior Técnico in Portugal. The doors that this master has opened for me are the greatest gift I have had from your institution.

Finally, I would like to thank my family and friends for their support and understanding. To Sebastian, I will be always grateful for your help with the thesis and my psychological stability during the last chapter of this journey. To my mom and dad for their words of support, optimism, and love. I owe you more than I would be able to ever repay.

Abstract

A new unidimensional, steady-state computational model was developed to simulate a calciner for the application of calcium looping as a way of thermochemical energy storage in concentrating solar power systems. The proposed reactor is an absorber tube enclosed within a reflective cylindrical cavity. The absorber tube is also the riser of a circulating fluidized bed where the calcination reaction proceeds. The proposed model heat transfer processes are based on the core-annulus model and the hydrodynamic proposed model is a modified version of the K-L model. The model considers the change in the mass flow rate of species and the density change of the phases in the axial direction of the reactor, which is usually considered constant in the available models from the literature. It was verified that assuming a constant density and a constant mass flow rate, leads to an efficiency increase up to 5% points for the studied conditions in the reference case. Simulations were performed imposing a constant wall temperature or non-uniform heat flux distribution on the reactor wall. The simulation shows that a 6 m height reactor allows achieving a calcination efficiency of 65 % for the conditions of the reference case. Higher heights do not contribute significantly to the efficiency increase. A sensitivity study shows that the decay factor, the inlet temperature of the bed, the mass fraction of CO_2 at the inlet, and the ratio between the gas and solids mass flow rates are the parameters that affect the most the efficiency of the process.

Keywords

Solar Reactor, Calciner, Circulating Fluidized Bed (CFB), Calcination, 1-D Model, Calcium Looping (CaL)

Resumo

Foi desenvolvido um novo modelo computacional unidimensional e em estado estacionário para simular um reator de calcinação a ser usado num ciclo do cálcio, como forma de armazenamento termoquímico de energia em sistemas de energia solar com concentração. O reator solar proposto consiste num tubo vertical colocado dentro de uma cavidade recetora e no seu interior existe um leito fluidizado ascendente onde se processa a reação de calcinação. Os processos de transferência de calor são baseados no modelo núcleo-ânulo e o modelo hidrodinâmico é uma versão modificada do modelo K-L. O modelo considera a alteração do caudal mássico das espécies e a alteração da densidade das fases na direção axial do reator, que são habitualmente considerados constantes nos modelos disponíveis na literatura. Verificou-se que a assunção de uma densidade constante e de um caudal mássico constante conduz a um aumento da eficiência máxima de 8 pontos percentuais para as condições de referência. Foram realizadas simulações impondo uma temperatura de parede constante ou uma distribuição não uniforme do fluxo de calor na parede do reator. Verificou-se que um reator com 6 m de altura permite alcançar uma eficiência de calcinação de 65% e que alturas superiores não contribuem significativamente para o aumento da eficiência. Um estudo de sensibilidade mostrou que o fator de decaimento, a temperatura de entrada no reator, a fração de massa de CO2 na entrada, e a relação entre os fluxos de massa de gás e sólidos são os parâmetros que mais afetam a eficiência do processo.

Palavras-chave

Reator Solar, leito fluidizado circulante, calcinação, Modelo 1-D, Ciclo do Cálcio (CaL)

Table of Contents

List of Figures

List of Tables

List of Acronyms

CFB	Circulating Fluidized Bed
CR	Cyclone Reactor
CSP	Concentrated Solar Power
FB	Fluidized bed
HT	Heat Transfer
HTC	Heat Transfer Coefficient
HTF	Heat Transfer Fluid
PCM	Phase Change Material
RK	Rotary Kiln Reactor
TCES	Thermochemical Energy Storage
TES	Thermal Energy Storage

List of Symbols

Roman Letters

A	Cross sectional area of bed/reactor, m^2
a	Decay factor, m^{-1}
C_P	Specific heat, J kg^{-1} K^{-1}
c	Concentration, mol m^{-3}
c_{eq,CO_2}	Equilibrium concentration of CO_2 in the gas phase, mol m^{-3}
d_p	Particle diameter, m
D	Diameter of the reactor, m
e_c	Emissivity of clusters, -
e_{dis}	Emissivity of the disperse phase, -
G_s	Solids circulating rate, kg m^{-2} s^{-1}
g	Gravitational acceleration constant, m s^{-2}
h	Heat transfer coefficient, W K^{-1} m^{-2}
$\tilde{H}_{calc}$	Calcination heat power, W m^{-1}
H_{dense}	Height of the dense bed, m
H_t	Total height of the reactor, m
h_{w-b}	heat transfer between the wall and the bed, W K^{-1} m^{-2}
K_{fg}	Thermal conductivity of gas, W m^{-1} K^{-1}
k_{calc}	Kinetic constant of $CaCO_3$ calcination, m^3 $kmol^{-1}$ s^{-1}
k	Thermal conductivity, W m^{-1} K^{-1}
$\dot{m}$	Mass flow rate, kg s^{-1}
m_{cv}	Mass in a control volume, kg
M	Molar mass, kg mol^{-1}
Pr	Prandtl number, -
$\dot{Q}_s$	Radiative net flux, W
$\dot{Q}_{th}$	Rate of sensible heat taken by the particle flow and air flow, W
$\dot{Q}_{ch}$	Power absorbed in the chemical process, W
R	Ideal constant gas, J kg^{-1} K^{-1}
r	Mass generation rate per unit of volume, kg m^{-3}
$\tilde{r}$	Moles generation rate of the species per unit of volume, mol m^{-3}
T_b	Temperature of the bed, K
$T_{filmavg}$	Mean gas-film temperature, K
t_c	Average residence time of clusters on the wall, s
T_c	Temperature of the cluster, K
U	Velocity, m s^{-1}
U_0	Superficial gas velocity, m s^{-1}
U_{mf}	Minimum fluidization velocity, m s^{-1}
U_t	Terminal velocity of particles, m s^{-1}
X_{calc}	Degree of calcination, -
X	Molar fraction, -
X	Mass fraction, -
Y	Solid volumetric fraction of the disperse phase in the vicinity of the wall, -
z	Height independent variable, m

Greek symbols

δ_c	Fraction of the wall that is in contact with the cluster, -

ΔH_{cal}	Molar reaction enthalpy of calcination, J mol^{-1}
ΔT_{cv}	Temperature difference of the wall with the bed for a given control volume, K
ε	Volumetric fraction, -
ε_c	Gas volumetric fraction within the clusters, -
ε_{cw}	Gas volumetric fraction near the wall, -
η_{ch}	Chemical efficiency, -
η_{th}	Thermal efficiency, -
η_{tot}	Total efficiency, -
$\eta_{receiver}$	Receiver efficiency, -
$\eta_{reactor}$	Reactor efficiency, -
$\eta_{process}$	Process efficiency, -
η_{calc}	Molar calcination efficiency, -
μ	Dynamic viscosity, Pa s^{-1}
ρ	Density, kg m^{-3}
ρ_{a+b}	Density of a mixture of species a and b, kg m^{-3}

Subscripts

c	Cluster
con	Convection
dis	Dispersed phase
$dense$	Dense zone in the riser
g	Gas
i	ith species
$lean$	Lean zone in the riser
p	Particle
rad	Radiation
s	Solid

Superscripts

*	Saturated carrying capacity conditions

Chapter 1

Introduction

In this chapter, the reader is introduced in section 1.1 to the relevance and motivation of the subject of this work, followed by an outline of the objectives and methodology pursued in this thesis in section 1.2. The structure of this work is demonstrated in section 1.3.

1.1. Motivation

Concentrating Solar Power (CSP) is unique among the renewable energy sources because it can easily be coupled with thermal energy storage (TES) making it highly dispatchable. Key categories for TES for CSP system are sensible TES (e.g. molten salts and packed beds), latent heat TES (e.g. encapsulated PCM), and Thermochemical Energy Storage (TCES) (e.g. carbonates, hydroxides, and metal redox) [1].

The major commercial solution used nowadays is molten-salt technologies accounting for 75 % of the globally installed TES capacity. The storage system is typically based on a two-tank system to use the sensible heat stored in molten salts. However, molten-salt as Heat Transfer Fluid (HTF) has several disadvantages: its corrosiveness, its maximum working temperature (~560 °C), which limits the system efficiency, and the significant energy consumption required to keep the molten salts at temperatures over 220 °C to avoid solidification [2].

In counterpart, TCES is an option that allows storing energy at higher densities than other storage solutions with the additional advantage of storing the reactant at ambient temperatures if required [1]. TCES relies on using the heat provided by CSP to carry out an endothermic reaction. The products of the reaction then can be stored and used when needed by carrying on the exothermic reaction that will release the stored energy [2].

Several reactions for TCES have been proposed: carbonates, hydroxides, metal redox, sulfur, hydrides, methanol, or ammonia. One of the most promising systems relies upon the calcination-carbonation reaction of $CaCO_3$-CaO and it is known as a Calcium Looping (CaL) process (Figure 1). In this system, the concentrated solar power is used to carry out the endothermic calcination reaction that releases CaO and CO_2 as products.

$$CaCO_3(s) \Leftrightarrow CaO(s) + CO_2(g) \quad ; \ \Delta H_{cal} = 178.4\ MJ\ kmol^{-1} \tag{1.1}$$

These products are stored separately and when needed, they are brought together to carry out the

exothermic carbonation reaction to release the stored energy. Table 1 compares chemical, physical, and engineering aspects of $CaCO_3$-CaO systems with molten salts and other TCES systems [2].

The main advantages of a CaL process over molten salts and other TCES systems are:

1) The low cost, wide availability and harmlessness of natural CaO precursors as limestone and dolomite guarantee the sustainable development of the storage solution.
2) The high energy density of the CaL system (3 – 4 GJ m-3) is one of the largest among TCES systems.
3) The high reaction turning temperature. Carbonation for generating heat is extremely fast in the range of 650 to 1000 °C depending on the CO_2 partial pressure. This would overcome the current CSP temperature limitations of 550 to 600 °C for molten salts. A higher efficiency could be achieved in CSP plants by increasing the maximum temperature reached.

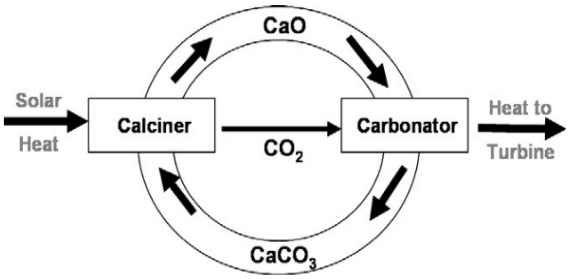

Figure 1. Calcium looping system applied to solar power thermal transport and storage [3].

Table 1. Comparison of TES technologies. The current state of the art, i.e. molten salts, and other TCES [2].

	TES system	**TCES systems**				
		Carbonates		**Hydroxides**	**Metal redox**	**Hydrides**
	Molten salts	**$CaCO_3$/CaO**	**$SrCO_2$/SrO**	**$Ca(OH)_2$/CaO**	**Co_3O_4/CoO**	**MgH_2**
Phase	**Liquid**	**Solid-gas**	**Solid-gas**	**Solid-gas**	**Solid-gas**	**Solid-gas**
Charging (˚C)	200 (minimum)	725-950	1150-1200	400-500	800-950	250-500
Discharging (˚C)	550-600 (maximum)	650-1000	900-1150	280-600 470kPa)	800-950	250-500
Theoretical energy density (GJ m^{-3})	0.4	3-4	4	1.6	1.06	2.1
Material cost	$893/tonne	$10/tonne	$580/tonne	-	250,000 €/tonne	-

In the last decade, the majority of the research related to the CaL process where most for post-combustion CO_2 capture system which involves carbonation under low CO_2 partial pressure and calcination carried under high CO_2 concentration at temperatures around 950 C. However, CaL conditions for TCES may differ since the concentration of CO_2 entering the carbonator is not imposed and it can be selected to minimize the impact of CaO deactivation. Ortiz et al. [2] summarize typical conditions for the post-combustion of CO_2 and the TCES of the CaL process as in Table 2.

A schematic of the calcium looping CSP plant is shown in Figure 2. In this concept, the heat of

carbonation is transferred to an airflow which powers a Brayton Cycle to produce electricity. The plant contains two reactor units, the solar calciner where concentrated solar energy is used for the calcination of $CaCO_3$ to produce CaO and CO_2, and the carbonator where CaO and CO_2 are recombined while releasing heat into the carrying air to transfer it to the gas turbine. Additionally, there are the storage vessels for the solids and CO_2 which would be sized to run the carbonator and turbine when solar radiation is not available, allowing the plant to generate electricity 24 h a day [3].

Table 2. Typical condition for CaL systems for the post-combustion of CO_2 and TCES [2].

CaL process application	**Typical conditions**	
	Calcination	***Carbonation***
Post-combustion CO_2 capture	950 °C high CO_2 v/v atmosphere (oxy-combustion) P=1 atm	650 °C 15% v/v CO_2 P=1 atm
Thermochemical Energy Storage	~725 °C/950 °C (He or H_2O/CO_2 atmosphere) P=1 atm	~850 °C Pure CO_2 P = 1-5 atm

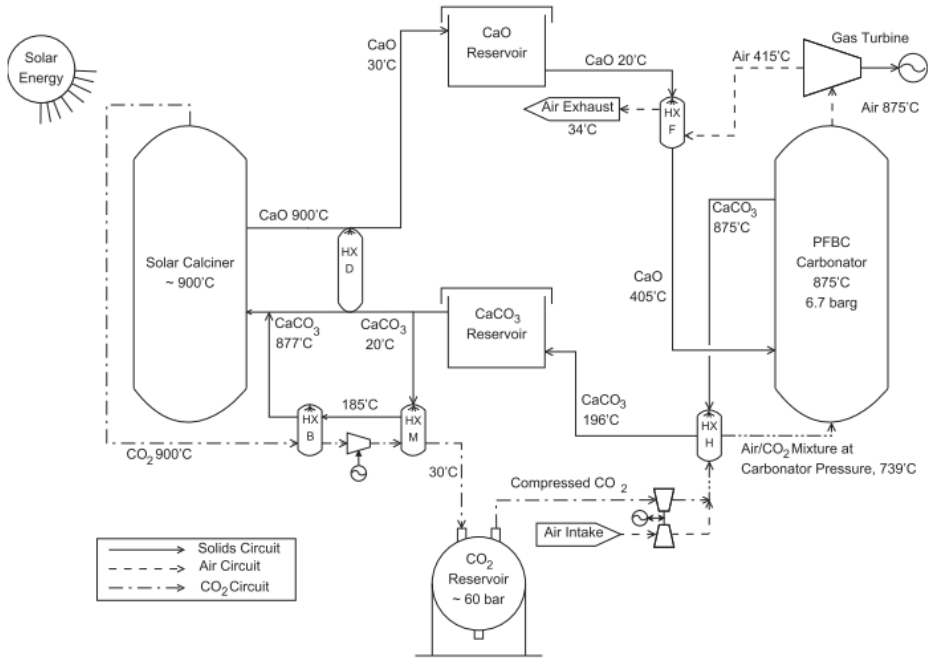

Figure 2. Flow diagram of the CaL CSP plant [3]

1.2. Objectives and Methodology

The main goal of this study is to develop a model of a reactor for the calcination of $CaCO_3$ considering that it would be later coupled with a CSP system for TCES. The steps to follow to achieve this includes:

1) *Research on the state of the art of solar reactors for the thermal decomposition of $CaCO_3$ and other chemical reactions*. The reactors are categorized based on two classifications related to the heat integration mode with the reactor chamber and the type of flow. All the experimental set-ups are described making emphasis on their size, geometry, operation conditions, and

efficiencies. A summary table with all the reviewed papers is the final product of this step.

2) *Discussion to ponder the benefits and downsides of each technology*. From the literature review, the most significant characteristics of the experimental results on solar reactors are gathered into two tables. One is based on the type of flow in the reactor and the other is based on the heat integration mode. In the first, each type of solar reactor is described based on their heat and mass transfer characteristics, their operation and particle residence time, issues as dust formation, clogging and erosion, and the parasitic energy requirements. In the second, the most relevant characteristics of directly and indirectly heated systems are summarized. Attention is paid to the heating pace of the reactor, thermal gradient along with the reaction chamber, hotspots formation, re-radiation losses, and issues as window cracking, degradation due to fouling of particles, and clogging.
3) *Selection of the reactor concept based on the previous discussion and the feasibility of coupling the solar reactor to a CSP system*. The outcome of this step is to define the design to be used as the start point of this study. It is expected that in the future one could add complexity to design by iterating on the steps described in the workflow summarized in Figure 3.
4) *Establish the geometry, materials, and operating conditions of the reactor*. For this, a literature review on conventional calciners is conducted. The input parameters and inlet conditions are gathered in this stage.
5) *Development of a model describing the reactor in terms of the reaction kinetics, hydrodynamics, and heat transfer*. The objective of this step is to develop a model that can reproduce the conversion of the sorbent inside the reactor. This model is a tool to be used for design purposes like assessing the needed height under given operating conditions or assessing the effect that inlet conditions would have on the performance of the reactor. This is why a base case is established using parameters obtained from the literature. Then, a sensitivity study is done by variating the relevant model input parameters and the inlet conditions. The model is initially designed for a constant wall temperature. A further step is given by using a heat flux distribution as input for the heat power from the wall to the bed. The used heat flux distribution is the result of a preliminary ray-tracing analysis.

The outcome of this work is to develop a model that can describe what is occurring inside the reaction chamber. In future works, this model would be coupled with the reactor's cavity model and the CSP field with the purpose of completing the workflow in Figure 3. Coupling the current model with the CSP system would allow having a final tool for the design of a prototype for testing the concept.

1.3. Structure of the Thesis

This thesis is composed of 5 chapters including this introduction. Chapter 2 presents the current state of the art of solar receivers/reactors for calcination. At the end of the chapter, a conclusion is reached regarding the selected reactor to be modeled in this work. Chapter 3 describes the mathematical model to be used. This includes the hydrodynamic model, heat transfer model, and final mass and energy balances. Chapter 4 presents the input parameters of the model and the results obtained for several

cases. This includes the case for constant wall temperature and the case of a constant heat power on the wall. Finally, Chapter 5 presents the main conclusions of the study and suggestions for future work.

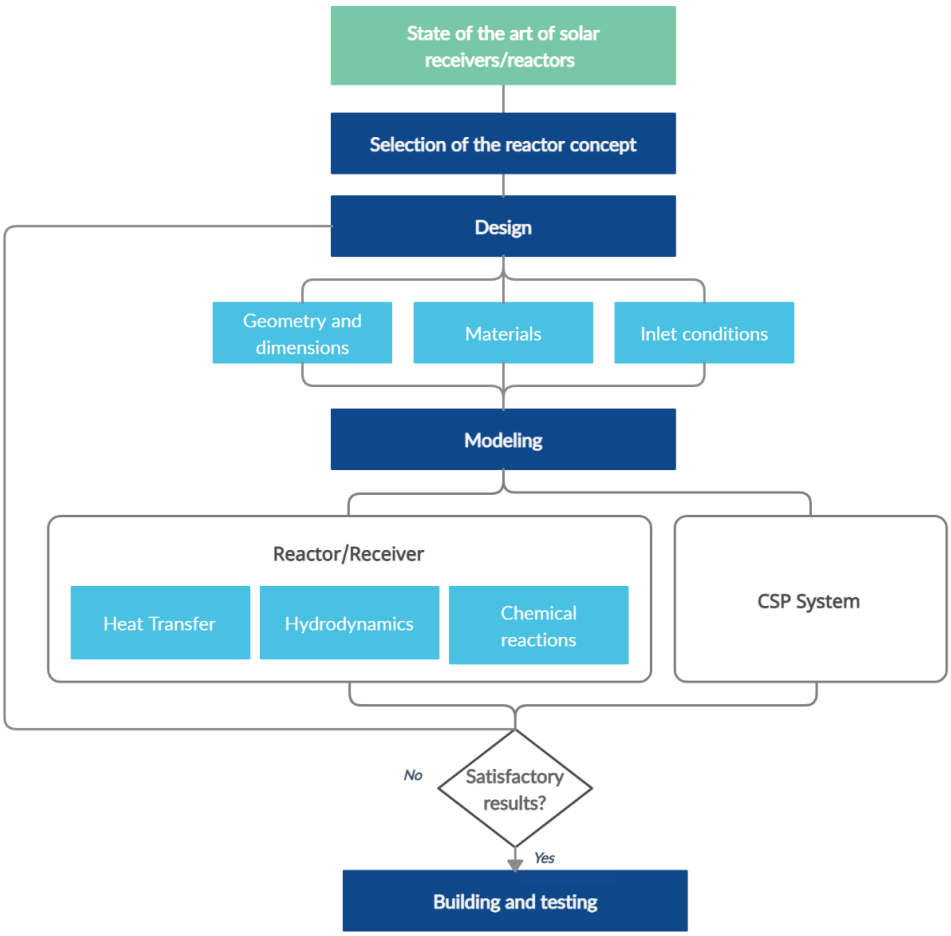

Figure 3. Workflow of the design of a solar receiver/reactor.

Chapter 2

State of the Art of Solar Receivers/Reactors

This chapter gives extensive reference related to the research on solar reactors for limestone calcination. The different solar reactors classifications used in the literature are discussed. The chapter aims to evaluate the advantages and challenges of different types of solar reactors and to select a configuration from which this investigation will proceed. Special attention is paid to the SOCRATCES [4], [5] project for being a recent project whose objectives are aligned with this investigation.

2.1. Solar Reactors Classifications

In the literature, it can be found different types of reactor classification depending on different criteria [6], [7]. Zsembinszki et al. [7] suggest three main parameters to classify solar-driven reactors, i.e. the heat integration mode into the reaction chamber, the flow pattern, and the reaction limiting step of the process. This last one is of interest when considering the calcium looping cycle as a whole. Consequently, the reaction limiting step classification will not be used in this work which centers on the calciner design only. Its description can be found in Annex A.1.

2.1.1. Classification based on the heat integration mode into the reaction chamber

This classification is based on the interaction between solar radiation and the thermochemical reactor [7]. It can be categorized into directly and indirectly irradiated reactors (Figure 4).

In indirectly irradiated reactors, the reactant does not receive direct concentrated irradiance. These reactors rely on a primary absorber where the heat resulting from the concentrated radiation is absorbed and transferred to the reactant or a secondary cavity. This arrangement is simpler but less efficient than directly irradiated reactors [6]. The heat transfer is limited by thermal losses through the absorber and the properties of the material composing it. Both aspects limit the maximum temperature of the system.

The temperature distribution along the reaction chamber is relevant when choosing the type of reactor to be used. In indirect systems, two types of configuration can be found (Figure 4): (1) a reactor composed of two cavities, one that receives the concentrated irradiance and the other that works as the reaction chamber, and (2) a reactor configuration were the reaction chamber is made of an array of tubes. In the second one, the temperature distribution might be an issue because experience has shown that different tubes across the reactor can have different temperatures.

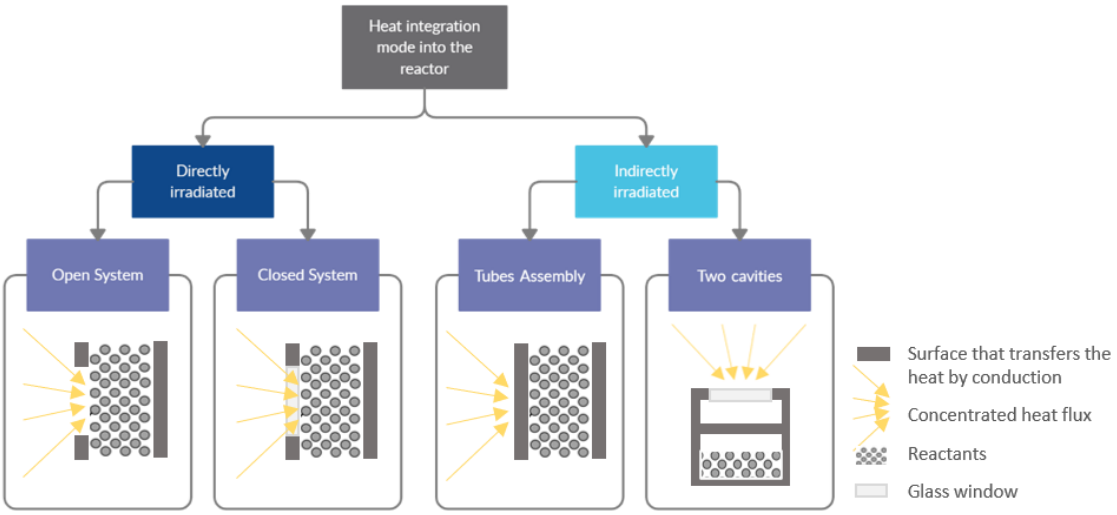

Figure 4. Solar thermochemical reactors classification based on the heat integration mode into the reaction chamber.

In directly irradiated reactors, the reactant is irradiated and heated by the solar radiation input enabling an efficient radiative heat transfer by avoiding having an intermediary surface as in the case of indirectly heated systems [3]. The reactants in this configuration serve as a protective layer that minimizes the reactor's component exposure to high radiative fluxes, reducing the amount of radiation absorbed by the reactor walls and its temperature. In the reactor, there is an aperture that might or not be sealed, i.e. open or closed systems respectively, by a refractory quartz glass window, which allows passing the concentrated solar radiation to the reaction site [2].

Zsembinszki et al. [7] state that the use of the quartz window is mandatory for direct systems for high temperatures processes (over 900 ^{o}C) to reduce heat and mass losses. However, the design of a suitable window is still a challenge. Additionally, during operation, the quartz glass must be kept clean to avoid the reduction of radiation transfer to the reaction chamber, hence reducing the system efficiency [6].

2.1.2. Classification based on the flow pattern

Different configurations of reactors have been proposed depending on the required residence time of the particles inside the reactor, and the presence of a carrier fluid and its contact with the particles. When considering the flow pattern, solar reactors can be divided into three main groups: stacked bed reactors, fluidized bed reactors, and entrained bed reactors [8]. In fluidized bed reactors, the particles move with the gas flow creating a bubble-induced phenomenon, while in the case of entrained bed reactors, specifically cyclones, the injected gas creates a vortex inside the cavity. In contrast, in stacked bed reactors no gas is injected in the process and the working principle will depend on whether the particles compose a fixed, moving, or rotating bed. Figure 3 shows the subtypes of reactors and examples of their application gathered from the literature.

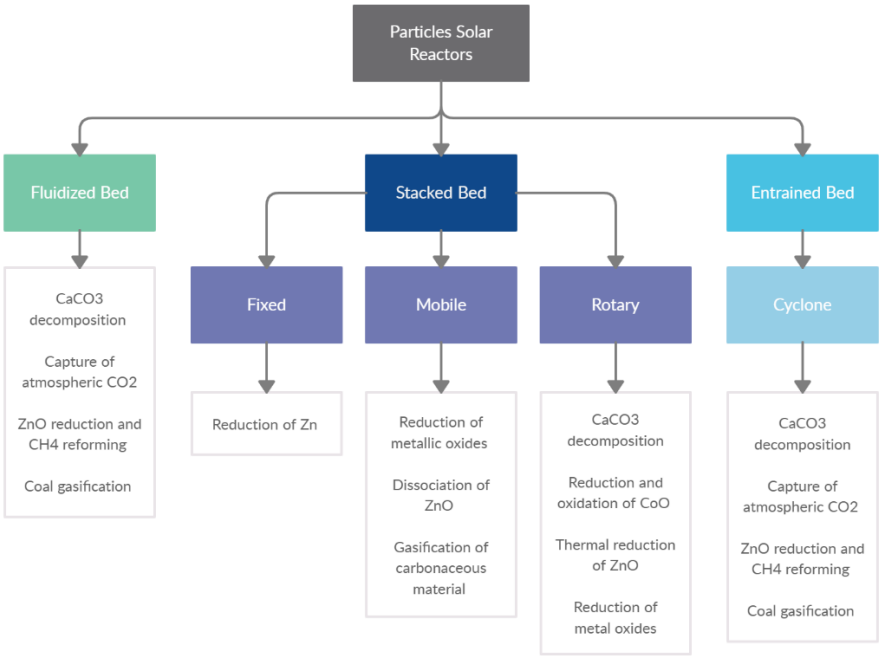

Figure 5. Solar reactor classification based on the flow pattern.

2.1.3. Solar Reactor Performance

To characterize the performance of the reactors summarized in this chapter, three types of efficiencies are defined in literature as follows:

1) The thermal efficiency (η_{th}), defined as the ratio of the rate of sensible heat taken by the particle flow and airflow (when used as transport fluid) to the solar power input:

$$\eta_{th} = \frac{\dot{Q}_{th}}{\dot{Q}_s} = \frac{\dot{m}\, C_P\, \Delta T}{\dot{Q}_s} \tag{2.1}$$

where ṁ represents the flow rate of particles and transport fluid (depending on the configuration used), C_p is the specific heat at constant pressure, ΔT is the temperature difference between the inlet and outlet, and $\dot{Q}_s$ is the incoming solar power input.

2) The chemical efficiency (η_{ch}), defined as the ratio of the power absorbed in the chemical process to the solar power input. For this calculation, the degree of calcination (X_{calc}) is also considered:

$$\eta_{ch} = \frac{\dot{Q}_{ch}}{\dot{Q}_s} = \frac{\dot{m}\, \Delta H_{calc}\, X_{calc}}{\dot{Q}_s} \tag{2.2}$$

where ΔH_{calc} is the reaction enthalpy of the calcination which is 1781 kJ kg^{-1} for $CaCO_3$.

3) The total efficiency (η_{tot}), defined as the sum of the thermal (η_{th}) and chemical efficiency (η_{ch}).

$$\eta_{tot} = \eta_{th} + \eta_{ch} \tag{2.3}$$

2.2. Literature Review of Solar Reactors

The solar calcination of $CaCO_3$ has been experimentally analyzed in previous studies. Forty-nine papers were identified in this literature review. From these, five were review papers, and nineteen were related to limestone calcination. There are some types of configurations of solar reactors that have not been tested for calcination. Therefore, other available experimental studies dealing with other processes were revised in this review, i.e. steam gasification of charcoal and sewage sludge, and water-splitting for hydrogen production by thermal decomposition of zinc oxide, copper oxide, tin oxide, and cerium oxide.

This literature review was structured as follows:

1) Fluidized bed reactors
2) Entrained bed reactors
3) Stacked bed reactors
    a. Fixed beds
    b. Mobile beds
4) Other configurations (heat pipes reactor and hot CO_2 reactor from SOCRATCES project)

Each subsection is further divided into two categories, indirectly and directly heated solar reactors. The literature review accounts for a total of 25 pages. Therefore, only fluidized bed reactors, the type of reactor selected to proceed with the development of the model (see discussion in section 2.3), will be presented in the body of this thesis. The rest of the literature review, i.e. entrained bed reactors, fixed and mobile bed reactors, and other configurations, can be found in Annex A.2-A.4.

2.2.1. Fluidized bed reactors

Gas-solid fluidized bed reactors have been proposed as a convenient solar receiver due to their large heat transfer coefficients in the order of hundreds of $W\ m^{-2}\ K^{-1}$, and thermal diffusivities, i.e. $10^{-2}\ m^2\ s^{-1}$. These properties are the result of the convective heat transfer due to the motion of the fluidized solid and the bubble-induced phenomena [9]. In fluidized bed reactors, the gas-solid contact is improved, and the residence time of the particles is increased when compared with entrained reactors. This is an advantage for chemical reactions with a slower kinetic mechanism [8].

There are two configurations of solar fluidized bed reactors based on the interaction between incident radiative flux and the fluidized bed, i.e. indirectly irradiated systems and directly irradiated closed systems.

Directly irradiated:

In directly irradiated closed fluidized bed reactors, radiation passes through a transparent window before directly heating the bed, allowing higher operating temperatures when compared with indirect systems. This system is promising for thermochemical storage applications with a high energy density that requires high operating temperatures. The main challenges rely on the need of keeping the glass

window clean and scratch-free to maintain the medium transmittance and avoid the efficiency reduction of the system, and the erosion of the internal components of the reactor [9], [10].

Flamant et al. [11] proposed a fluidized bed reactor using a transparent silica wall of 0.3 m height and a 10^{-3} m^2 cross-sectional area, allowing direct irradiance of a bed of limestone particles of 0.6 - 2 mm diameter (Figure 6). The thermal and chemical efficiencies were 20 - 40 %, and 20 % respectively [8]. The experimental results showed a uniform temperature distribution through the fluidized bed. The total heat loss of the received energy is 46.3 % from which 14.3 % account for convection and conduction losses and 32 % for radiative losses through the glass window. To avoid radiative losses the author suggests increasing the absorptivity of the material. The authors do not comment on abrasion nor dust in the walls which would decrease the transmittance and therefore reduce the energy absorbed [12].

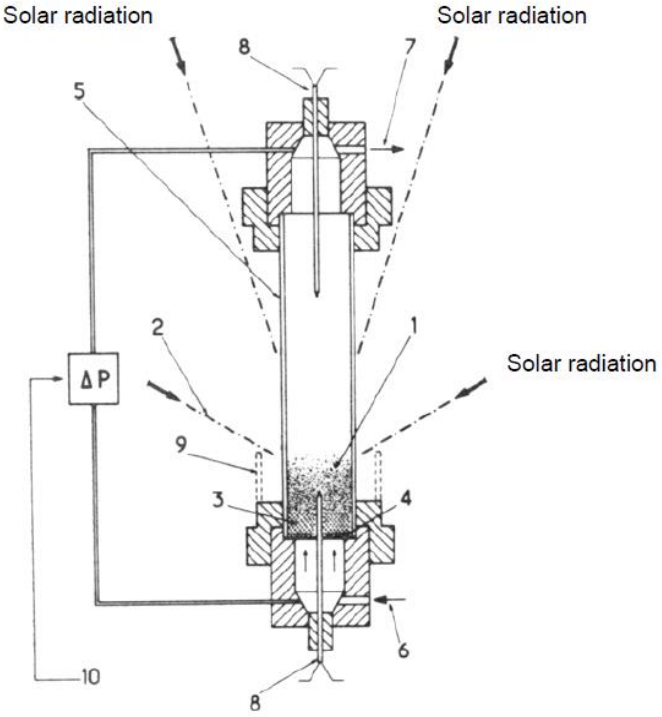

Figure 6. Schematic diagram of the solar fluidized bed reactor from Flamant et al. [11]: (1) fluid bed, (2) concentrated solar rays, (3) gas distributor consisting of glass, iron or zirconia beads, (4) grid, (5) transparent silica tube, (6) gas inlet, (7) gas outlet, (8) thermocouples, (9) reflectors, and (10) pressure loss measurement.

Nikulshina et al. [13] tested a laboratory-scaled solar reactor to consecutively perform the CaO carbonation and the $CaCO_3$ calcination reaction to capture CO_2 from the atmosphere. The solar reactor consisted of a fluidized bed where the particles were directly exposed to the solar radiation from a high flux solar simulator with a power up to 75 kW. The reactor was designed as a quartz tube of 25 mm outer diameter, 3 mm thickness, and 25 cm height, positioned at the focal plane of the solar concentrator (Figure 7). The tube contained the fluidized bed reacting particles of $CaCO_3$ or CaO. The arrangement was designed to attain uniform irradiance, temperature, and gas-solid contacting surface for efficient heat and mass transfer. Complete calcination was achieved after about 500 s, and a maximum temperature of 875 °C was obtained. With the increase of the cycles, there was a decrease in the CaO

particle size due to the attrition of the SiO_2 grains used as inert material to help the fluidization process.

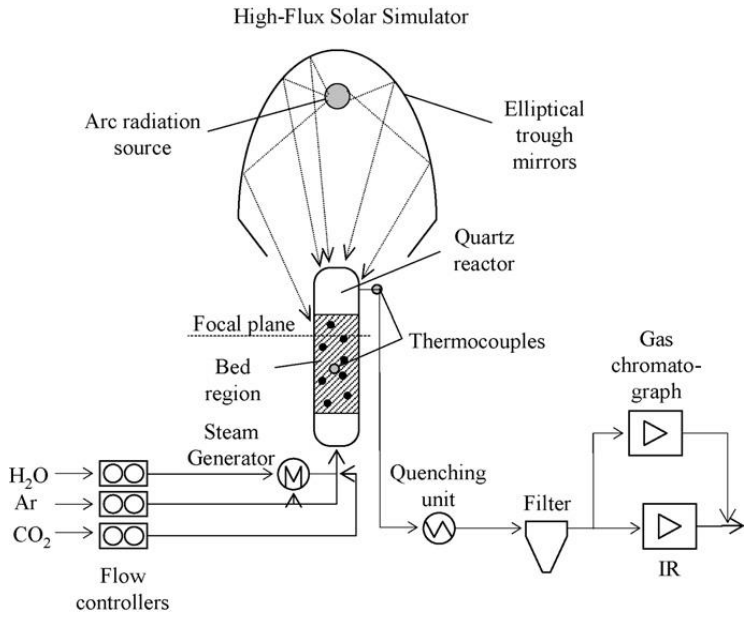

Figure 7. Experimental set-up of the fluidized bed reactor for CO_2 capture from the atmosphere from Nikulshina et al. [13].

Tregambi et al. [14] studied a directly irradiated fluidized bed reactor using an array of short arc Xe-lamps and elliptical reflectors with a total power of nearly 3 kW incident on the bed surface (Figure 8). The purpose of the research was to perform calcium looping tests to accomplish energy storage by solar-driven calcination of limestone and to perform solar aided CO_2 capture from flue gas. The results showed a decrease in the release of CO_2 after the fourth calcination cycle which suggests a stabilization of the material performance and a decrease in the sintering relevance.

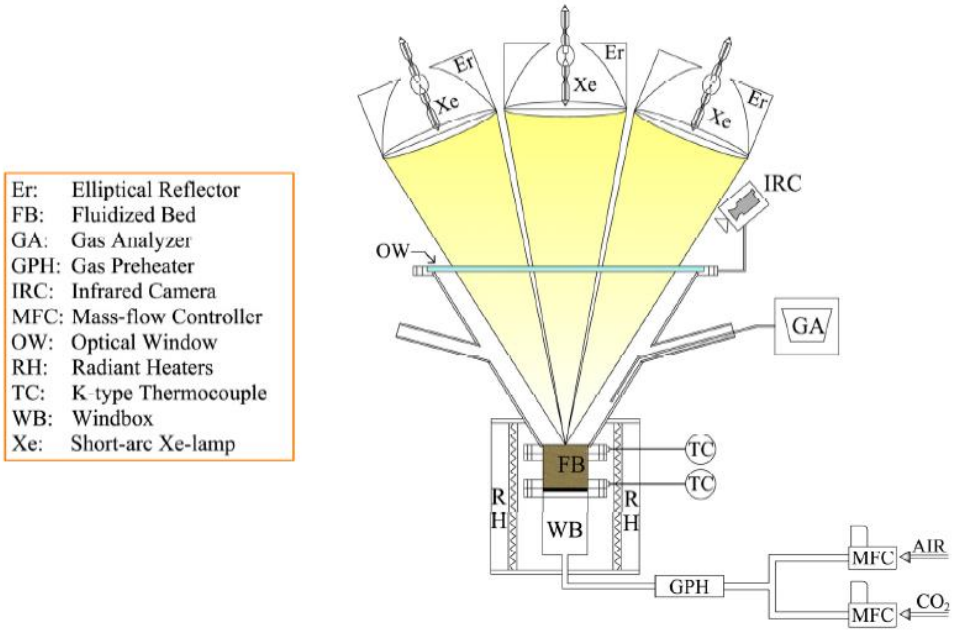

Figure 8. Experimental set-up of the fluidized bed reactor for calcium looping tests from Tregambi et al. [14].

Tregambi et al. [15] designed a batch laboratory-scale fluidized bed reactor by coupling a fountain-like solar receiver and a double pipe heat exchanger. The inlet bed particles are preheated by sensible heat of the outlet solids achieving high temperatures. Figure 9 shows a detailed scheme of the reactor consisting of the assembly of two concentric tubes. The inner tube has four holes to allow the circulation of bed solids from the inner tube space to space in between tubes. The top of the tube is closed by a transparent quartz glass of 2 mm thickness to seal the reactor and let the solar radiation enter.

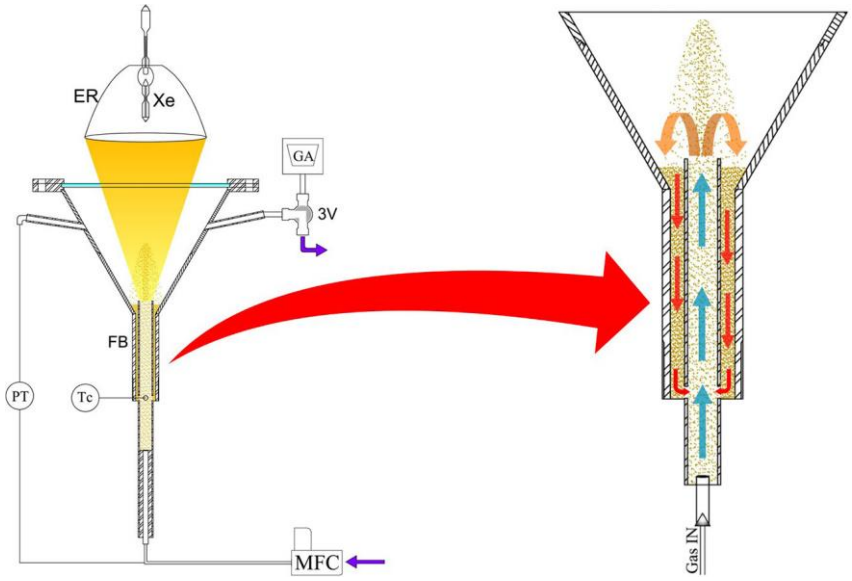

Figure 9. Experimental set-up and close-up view of the fluidized bed reactor from Tregambi et al. [15]

Indirectly irradiated:

In indirect irradiated systems, the solar radiation is directed into an arrangement of tubes or a cavity where the heat is transferred to the fluidized bed. In these systems, the solid particles are forced upward by airflow through the irradiated tubes or cavity. The airflow fluidizes the particle and increases the heat transfer from the irradiated surface to the particles [7]. This configuration is the simplest but may lead to unacceptable thermo-mechanical stresses acting on the solar irradiated surface of the reactor [9].

During the literature review, ten papers were consulted for indirectly heated fluidized bed reactors. One of them referred to an indirectly irradiated fluidized bed using a non-cylindrical cavity for calcination (Figure 10). The other publications referred to indirectly heated tubes for other processes as experiments of dense particle suspension (Figure 11) and steam gasification (Figure 12). No experiment was found for calcination using indirectly heated tubes.

Esence et al. [16] modeled and tested a laboratory-scale fluidized-bed solar reactor for calcination of dolomite. The reactor consisted of an indirectly heated reactor composed of four compartments in series. The use of compartments helps to reduce the dispersion of the residence time distribution of the particles and to increase the homogeneity of the product conversion. The particles are fluidized with preheated air injected from the bottom of the reactor through two perforated tubes and the radiation falls into the front wall of the reactor. Using a solar furnace of 1 MW at Odeillo's solar furnace, half decomposition of

dolomite ($CaMg(CO_3)_2$) is achieved with a degree of 100 % resulting in calcium carbonate, manganese oxide, and CO_2 for a stream of 9.4 kg/h. The air and CO_2 produced are sucked from the top of the reactor. A complete decomposition was not possible because the temperature was not enough to decompose the calcium carbonate when taking into account the CO_2 partial pressure in the reactor. The chemical efficiency was 6.6 % which the authors claim to be not critical because the purpose of this lab-scale prototype was to control the particle flow and the front wall solar flux distribution. The authors claim that efficiency will improve by using a cavity-type reactor concept currently being tested.

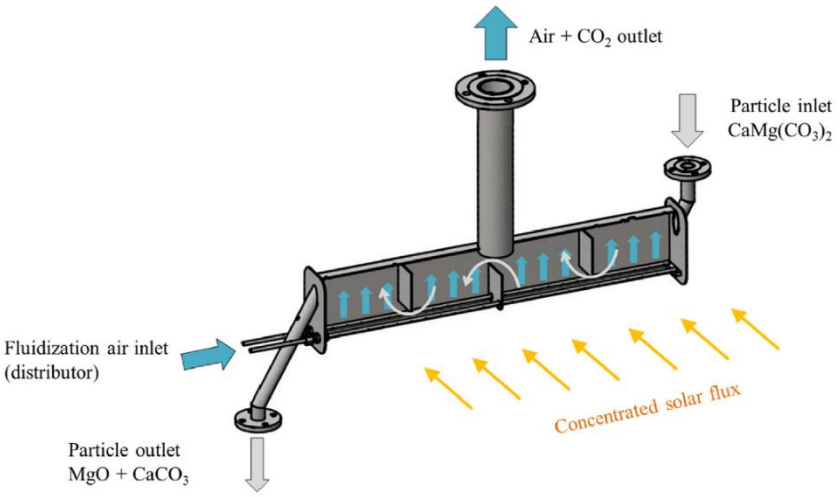

Figure 10. Isometric view of the fluidized bed solar receiver Esence et al. [16].

An example of an indirectly irradiated fluidized bed reactor using an irradiated tube configuration is the work of Benoit et. al [17] who tested a solar receiver with one single opaque tube containing solid-gas dense suspension upwards. The solar absorber metallic tube was located inside an alkaline-earth silicate cylindrical cavity that was irradiated through a rectangular opening (Figure 11.a). Gallo et al. [18] presented the design and performance analysis of a receiver based on the use of dense particle suspension. In this concept, schematized in Figure 11.b, the fluidized particles pass through absorber tubes onto which the solar flux is focused. The advantage of the upward flow of the particles relies on the controllability of the residence time.

Li et al. [19] designed and experimentally validated a fluidized bed solar reactor for the steam gasification of sewage sludge for the production of syngas with a high content of hydrogen. The gasifier consisted of a cylindrical cavity receiver where a fluidized bed receives the solar radiation (Figure 12). The inner cavity wall is made of silicon carbide, a durable material at high temperatures, and with high chemical inertness. While the outer cavity is made of a ceramic with high durability and reflectivity to maximize the absorption. A window is integrated into the outer cavity to minimize heat losses between the inner cavity and the environment. The transient simulation yields a hydrogen production in the range of 61.2 - 67.6 g per kg of sludge for a power input of 2.2 MW. The solar to fuel efficiency of 26 % was achieved.

The use of an indirectly heated configuration in a multi-tube fluidized-bed could lead to a temperature difference between the tubes of the arrangement. The variation of the temperature profile across the transversal cross-section of the system could result in a change in the calcination rate and the degree

of calcination of the particles depending on the location of the tube, being higher at the ones where the solar flux is falling upon.

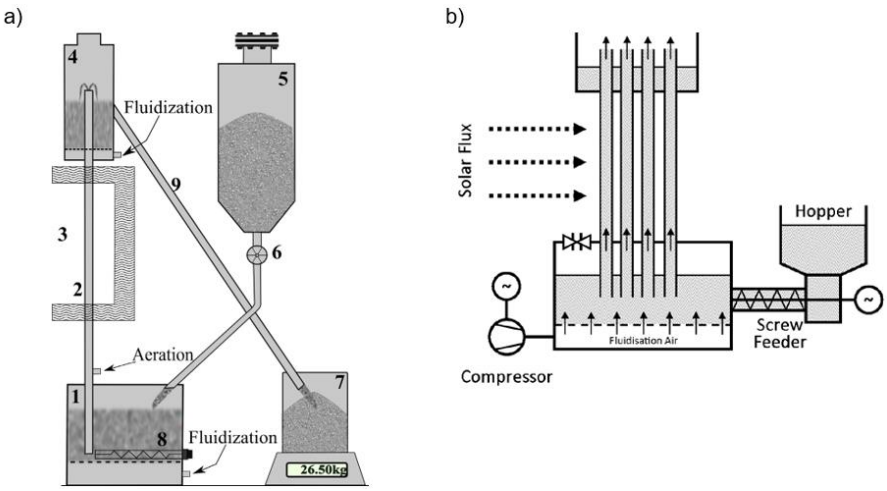

Figure 11. Experimental set-up of fluidized bed reactor. a) Single-tube solar receiver: (1) dispenser fluidized bed, (2) solar absorber metallic tube, (3) solar receiver cavity, (4) collector fluidized bed, (5) solid storage tank, (6) rotary valve feeder, (7) weighing scale, (8) electrical resistances, (9) solid evacuation tube from Benoit et. al [17]. b) Multi-tube receiver from Gallo et al. [18].

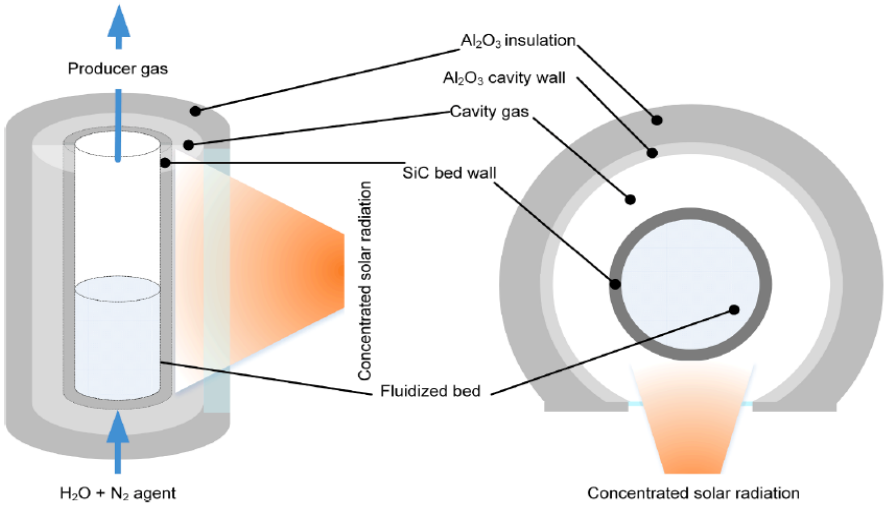

Figure 12. Scheme and close-up view of a fluidized bed solar gasifier from Li et al. [19].

In the case of a fluidized bed of one uncontained irradiated tube, a significant amount of energy would be lost through re-radiation. This is supported by the discussion presented in the deliverable of the SOCRATCES project where an irradiated tube design is proposed (Figure 13) [4]. The analysis showed that high re-radiation losses will lead to an efficiency of 4.8 %. Therefore, the authors concluded that it would be necessary to insulate the tube and provide the radiation differently. Even though this design is a falling particle reactor, the same logic could be used regarding the re-radiation losses for a fluidized bed reactor with an uncontained irradiated tube.

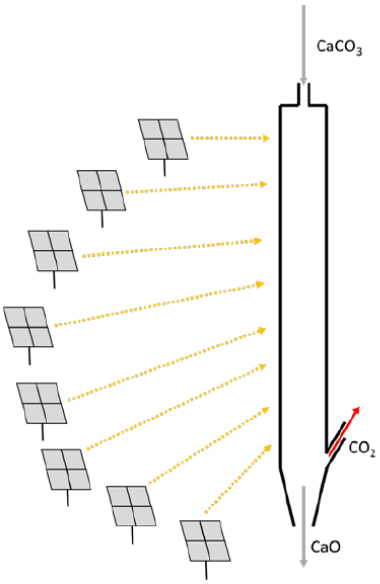

Figure 13. Irradiated tube reactor design proposed by SOCRATCES [4].

2.3. Evaluation of Existing Reactor Designs

Table 3 summarizes the available publications on experimental solar reactors for thermal decomposition of limestone that have been published until May 2020. Around fifty papers were reviewed, from which nineteen papers were related to limestone calcination. From them, eight (42 %) were directly heated reactors with a closed system, seven (37 %) were directly heated reactors with an open system and four (21 %) were indirectly heated reactors. Looking at a higher level in the classification, the most used reactor that has been tested at a laboratory scale is the rotary reactor, followed by fluidized bed reactors and lastly cyclone reactors.

Two decisions had to be taken when selecting the solar reactor concept to proceed with this work. The first is the heat integration mode into the reaction chamber and the second the type of flow pattern of the solid-gas flow. To evaluate the existing reactor concepts, Table 4 and Table 5 are the final products to be used for this analysis. Table 4 shows the criteria selected for the reactors' evaluation based on their characteristics. Similarly, Table 5 summarizes the benefits and challenges of directly and indirectly irradiated systems.

Table 3. Summary of the experimental results from the literature review of solar reactors for limestone calcination presented in section 2.2.

Reactor Type	Sub-type	Heat integration mode into the reactor	Type of system	Number of total papers reviewed	Number of papers reviewed involving $CaCO_3$ calcination	Author	Year	Power (kW)	Tmax (K)	Operation	Mass flow if cont. operation (kg/h)	Mass if batch operation (g)	Thermal Efficiency (%)	Chemical Efficiency (%)	Total Efficiency (%)	Degree of calcination (%)	Length / Diameter (mm/mm)	Particle size (µm)
Fluidized bed	**-**	Direct	Open	0	None													
			Closed	7	6	Flamant et al.	1980	1.75	1575	Batch	-	10	20 - 40	20	40 - 60	80 - 100	300/35	200 - 315
						Nikulshina et al.	2009	75	1150	Batch	-	7 [1]	-	-	-	≤ 71	250/25	-
						Tregambi et al.	2017	3.2	1200	Batch	-	120	-	-	-	88	100/100	420 - 590
						Tregambi et al.	2019	2	1448	Continuous	7.58	-	-	-	-	-	120 (cylinder) + 12 (cone)/12	250
		Indirect	-	3	None	Applied in dense particle suspension in single-tube solar receiver (Benoit et al., 2015), a multi-tube receiver (Gallo et al., 2015) and steam gasification of sewage sludge (Li et al., 2020)												
Entrained bed	**Cyclone**	Direct	Open	4	4	Steinfeld et al.	1992	3	1300	Continuous	0.60	-	34	9	43	53 - 94	300/200	1 - 5
						Imhof et al.	1997	54	975	Continuous	25.00	-	73	15	88	32 - 85	800/540	< 10
			Closed	3	1 [2]	Nikulshina et al.	2009	3.7	1223	Continuous	0.18	-	-	7 - 10	-	83	210/120	6
		Indirect	-	2	None	Applied in steam gasification of charcoal (Melchior et al., 2009)												
Stacked bed	**Rotary**	Direct	Open	4	3	Flamant et al.	1980	1.5	1775	Cont./Batch	0.28	8	10 - 30	15	25 - 45	30 / 60 [3]	90/20	200 - 315
						Meier et al.	2004	10	1423	Continuous	1.30	-	-	20	-	> 95	600/350	2000 - 3000
						Moumin et al.	2019	14	1300	Continuous	9.6 / 6.2 5	-	22 / 17	15 / 20	37 / 37	44-73 / > 95	735/240	< 176
			Closed	7	1	Moumin et al.	2019	The closed system experimental test was interrupted due to clogging issues in the suction system located at the reactor aperture										
					None	Applied for ZnO thermal decomposition (Haueter et al., 1999; Romero et al., 2012; Steinfeld et al., Schunk et al., 2009) and CuO/CuO_2 thermal decomposition (Neises et al., 2012; Arribas et al., 2015)												
		Indirect	-	3	3	Meier et al.	2006	10.6	1400	Continuous	7.00	-	22	35	57	≤ 98	225/252	2000 - 3000
						Badie et al.	1980	2	1575	Continuous	1.29	-	-	65	-	80	90/20 [4]	200 - 315
						Abanades et al.	2018	0.75	1325	Continuous	0.16	-	-	17	-	100	400/20	50 - 100
	Mobile	Direct	Open	0	None													
			Closed	2	None	Applied in ZnO thermal decomposition (Koepf et al., 2012)												
		Indirect	-	2	None	Applied in ZnO reduction with carbon (Wieckert et al, 2004; Schaffer et al., 2003)												
	Fixed	Direct	Open	0	None													
			Closed	4	None	Applied in ZnO, SnO2 thermal decomposition (Agrafiotis et al., 2015); MnO2, Mn3O4, Mn2O3, Mn3O4, CeO reduction (Alonso et al., 2015)												
		Indirect	-	3	None	Applied in steam gasification of charcoal (Puig-Arnavat et al., 2013; Piatkowski et al., 2008)												

[1] The mass is a mixture of CaO and SiO

[2] This paper corresponds to the $CaCO_3$-decomposition and CH_4-reforming, no other paper was found for the $CaCO_3$ decomposition

[3] 30 % and 60 % degree of calcination was achieved for the continuous and batch experiment respectively

[4] The reactor is an improvement of Flamant et al. 1980 with a transfer wall of 6.6 cm length and 5.25 cm diameter

[5] Two different mass flow were used for testing the reactor

Table 4. Characteristics reported in reviewed publications for fluidized bed reactors, cyclone reactors, and stacked bed reactors.

				Stacked Bed Reactors			
		Fluidized Bed Reactor	**Cyclone Reactor**	**Rotary Reactor**		**Mobile Bed Reactor[1]**	**Fixed Bed Reactor[2]**
	System reported in literature	**Closed**	**Open and Closed[3]**	**Open**	**Indirect**	**Closed and Indirect**	**Closed and Indirect**
	Reference	[14], [20]–[24]	[12], [13], [25]–[28]	[20], [27], [29]	[20], [24], [30]	[31]	[32]
Heat Transfer	Heat transfer rate	High	High	Moderate	High	High - Moderate	Low
	Longitudinal thermal gradient[4]	Low to high[5]	Low	High	Low	High	High
	Transverse thermal gradient	Low	Not reported	Not reported	Low [6]	Low	Not reported
Mass Transfer	Mass transfer rate (diffusion)	High	Not reported	High to moderate	High to moderate	Not reported	Not reported
	Mixing of solids leading to good calcination degree and uniform gas composition	Good to moderate[5]	Not reported	Moderate to low	Good	Not reported	Bad
Operation	Adjustable residence time	Yes	No	Yes	Yes	Design dependent	Yes
	Residence time in the high-temperature zone	Long to short[5]	Short	Medium to short	Short	Not reported	- [7]
	Possibility of continuous operation	Yes	Yes	Yes	Yes	Yes	No
Particle	Particle size	Small (< 1 mm)	Small (< 1 mm)	Up to 3 mm	Small (< 1 mm)	Design dependent	Any
	Dust formation due to particle movement	Yes	Yes	Yes	No	Yes	No
	Particle erosion against walls, windows, and other particles	High	Not reported	Not reported	No	Low	Low
	Clogging issues reported in literature	Not reported	No	Yes	No	No	No
Air	Use of transport air to ensure the transport of reactive particles	Yes	Yes	No	Yes	Yes[5]	No
Parasitic Energy Requirement (Energy Penalty)	Equipment for air injection	Yes	Yes	No	Yes	Yes	No
	Equipment for rotation of parts	No	No	Yes	Yes	No	No
	Equipement for vibration or moving table	No	No	No	No	Yes	No

[1] Based on the experimental results of a solar-thermochemical reactor for the reduction of ZnO powder

[2] Based on the experimental results of coal gasification for syngas production

[3] The reviewed closed reactor involves limestone calcination and methane reforming (no other paper was found for the $CaCO_3$ decomposition only)

[4] For FB the temperature gradient is measured on the central axis. For CR and RK the temperature gradient is measured on the reactor wall

[5] Dependant on design

[6] Abanades et al. (2018) reported no temp gradient between the front and rear part of the tube

[7] The high temperature zone is limited to the upper layer of the bed

Table 5. Characteristics reported in reviewed publications for directly and indirectly heated reactors.

Characteristic	Directly Heated Systems		Indirectly Heated Systems
Direct concentrated solar radiation focused on	Reactant		Intermediate radiating surface / sub-surface of the primary cavity
Heating pace	Fast		Slow
Distribution of radiation (among the cavity)	Less challenging		More challenging
Reactors wall temperature	Lower		Higher
Longitudinal thermal gradient across the reaction chamber	High		Low
Hotspots formation	Likely[1]		Unlikely
	Open	Closed	
Gas-tightness and possibility of capturing CO_2 mass	No	Yes	Yes
Risk of cracking of the window	N/A	High	N/A
Risk of degradation of the window for fouling of particles	N/A	High	N/A
Risk of clogging	Low	High	Low
Re-radiation losses through openings	Moderate	Low	Low to high

[1] The hotspot formation can be improved by introducing turbulence to the particle flow by injecting gas to enhance mixing or by using a conical cavity where the particle moves in a vortex through the reactor

From the fourteen laboratory experiments revised in Table 3, only ten reported the chemical efficiency and from these, six reported the thermal efficiency. Even though this information might not be enough to make strong conclusions, some general thoughts could be drawn on the total efficiency (defined as the ratio of the sum of the power absorbed in the chemical process and the rate of sensible heat taken by the particle flow and airflow - when used as transport fluid - to the solar power input).

It can be seen from Figure 14 that the total efficiency increases when increasing the dimensions of the receiver, i.e. length (Figure 14.a) and diameter (Figure 14.b). For a larger reactor, there is an increase in the power and the mass flow rate due to the scale-up effect. The efficiency increase is because for larger reactors there are lower specific losses.

The previous argument is further supported by Figure 15, where it can be concluded that there is a dependency of the total efficiency on the mass flow rate (Figure 15.a) and power (Figure 15.b). However, Figure 16.a shows that there is no dependence on the specific power – the ratio of power to mass flow rate. Therefore, the dependency of the total efficiency with the mass flow rate and power could be explained by the dependency on the dimensions of the reactor only. Figure 16.b shows a decrease in the total efficiency with the maximum temperature which is mainly a result of the decrease in the thermal efficiency due to higher thermal losses at higher temperatures.

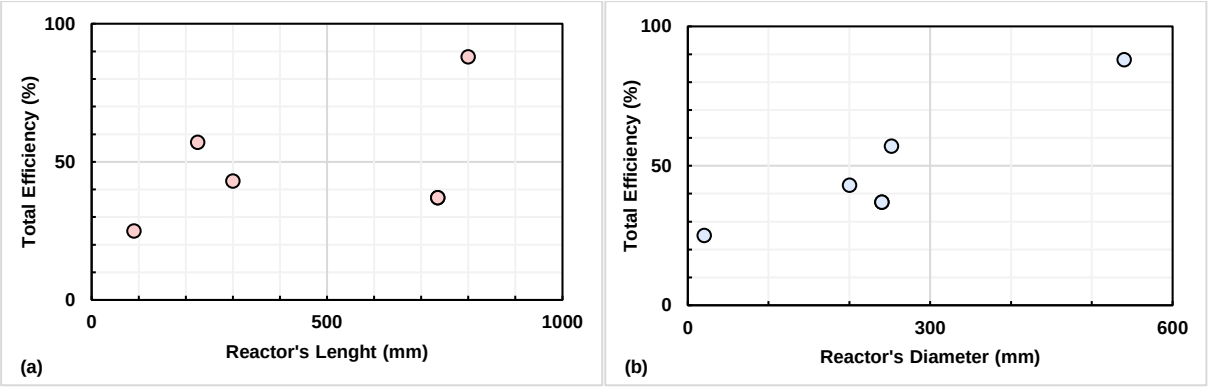

Figure 14. Total efficiency relation with the reactor's dimensions: (a) length and (b) diameter.

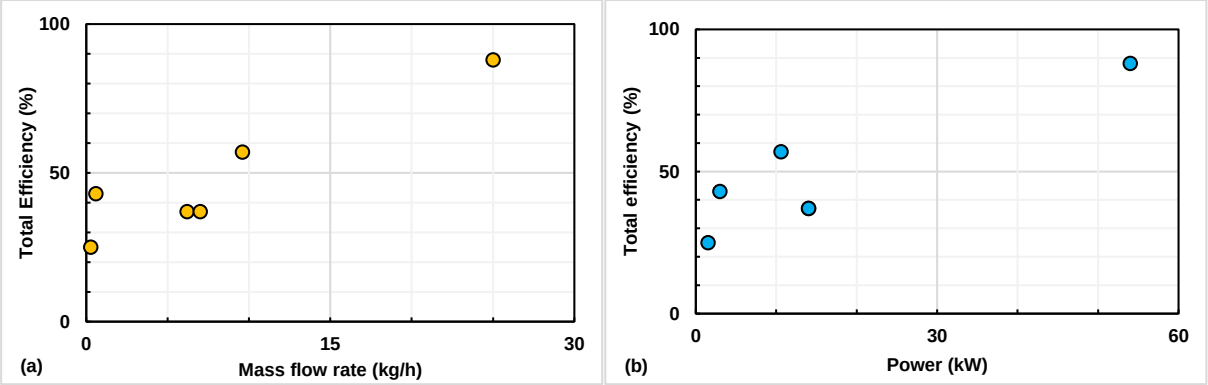

Figure 15. Total efficiency relation with mass flow rate (a) and power (b).

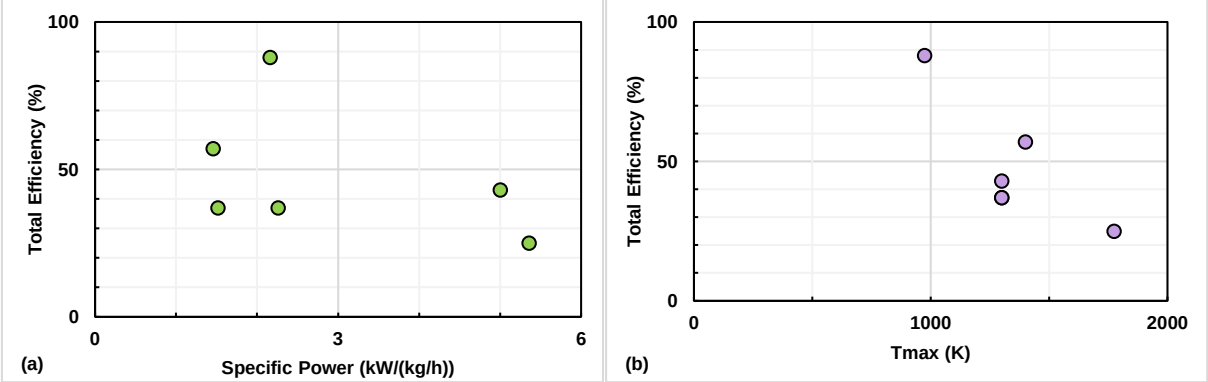

Figure 16. Total efficiency relation with specific power (a) and maximum temperature (b).

2.4. Selection of the solar reactor concept

Two decisions had to be taken when selecting the solar reactor concept to proceed with this work. The first is the heat integration mode into the reaction chamber and the second the type of flow pattern of the solid-gas flow.

After an intensive review and discussion on the conducted literature review, it was concluded that indirectly heated systems are the preferred concept. The main benefit is the lack of need for a quartz window which could bring complications — namely the risk of window degradation and crack, and the clogging of the suction system used to keep it clear. Besides, the use of an intermediate radiating surface

helps to smooth the temperature differences reducing the risk of over and under heating the reactant as it passes through different parts of the reactor. The price to pay is on the challenge of distributing the radiation through the irradiated surface, the high temperatures it must stand, and the re-radiation losses through the opening. From this analysis, the balance between benefits against challenges of the indirect heating configuration makes it the favored option.

In terms of the flow pattern, it was concluded that the Fluidized Bed (FB) reactor is the preferred option for performing well on the selected criteria shown in Table 4. The major benefits of FB are their high heat and mass transfer rate, good mixing of solids, adjustable residence time with long permanence in high-temperature zones, and the possibility of continuous operation, i.e. Circulating Fluidized Bed (CFB). From the stacked bed reactors, only rotary kilns showed to perform well under the selected criteria. However, a system with rotating parts adds complexity to the operation of the solar reactor and therefore was discarded. Similarly, mobile beds were discarded also for the need for moving parts and the fact that it is an untested design that is likely difficult to control. Fixed beds were abandoned for their low heat transfer rate and the impossibility of continuous operation. Finally, cyclone reactors were discarded for the short residence time of the particles under the high-temperature zone beside the impossibility of adjusting the residence time of the particles once the reactor is built.

Figure 17 shows a sketch of the selected concept, i.e. an absorber tube inside a cavity. The absorber tube also has the role of the riser of the CFB. As an initial step, the objective will be to model and assess the performance of one absorber tube reactor in terms of the reaction kinetics, hydrodynamics, and heat transfer. In future works, this model will be coupled with the reactor's cavity model and the CSP field. At each iteration for improving the final model, complexity will be added to build a final tool that can be used for design purposes. With this tool different configurations could be tested, e.g. several risers inside the reflective cavity. As for now, this study looks to develop a model that can simulate the conversion of the sorbent inside the absorber tube.

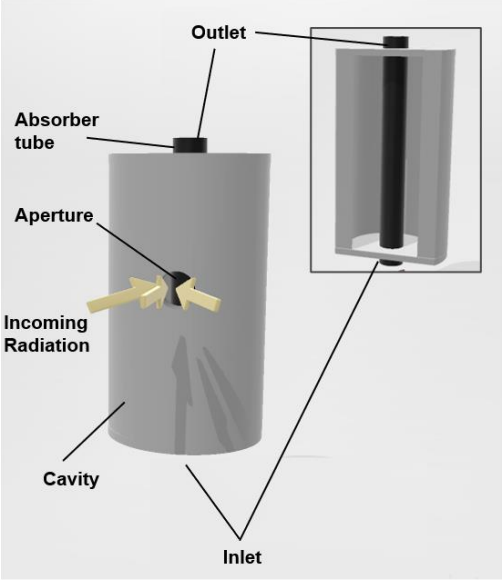

Figure 17. Isometric view of the proposed reactor with its cross-section. The presented scheme is not to scale

Chapter 3

Theoretical development of the model

In Chapter 2 it was concluded that an indirectly heated riser of a Circulating Fluidized Bed (CFB) would be the design selected for continuing this investigation. Therefore, this chapter provides the basic concepts of CFB and the mathematical and computational foundation for the solution of the calcination reaction in a circulating fluidized bed. The model is unidimensional and is constituted by a set of ordinary differential equations (ODE) resulting from mass and energy balances. The moment equations are integrated through the characteristics of the flow, based on experimental results for this type of system.

3.1. Fundamental Concepts

3.1.1. Circulating fluidized beds

Fluidized beds can be categorized as conventional, for low-velocity operations, and circulating fluidized beds (CFB), for high-velocities. The circulating fluidized bed is a high-velocity gas-solid suspension where particles are elutriated by a fluidizing gas above the terminal velocity of particles. There are different flow regimes as shown in Figure 18. The fluidized bed goes through particulate, bubbling, turbulent, fast fluidization, and pneumatic transport as the velocity increases. The transport velocity marks the limit between low-velocity fluidization and high-velocity fluidization. In the present study, the focus will be on the fast fluidization regime for the possibility of continuously operating the reactor.

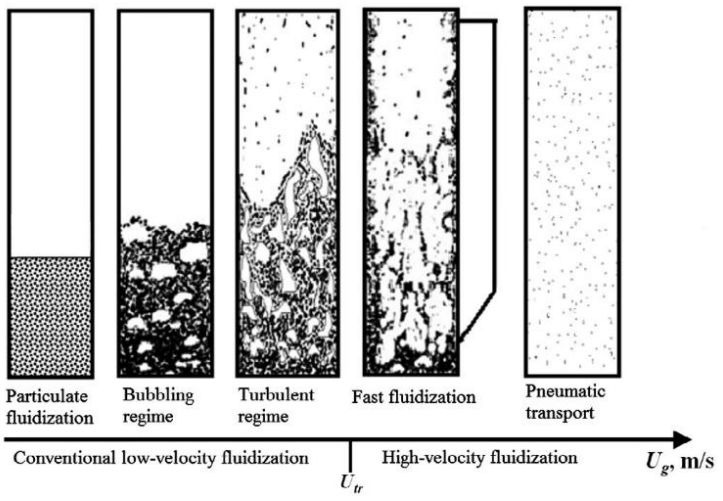

Figure 18. Flow regimes for gas-solid fluidization systems [33].

For the classification of regimes, several diagrams have been published [34], [35]. However, these flow

diagrams were presented when yet the definition of fast fluidization was not agreed upon. For this reason, the new flow regime map from Sun and Zhu [33] will be used (Figure 19). The operating parameters for the regime classification are based on the superficial gas velocity (U_0), which is the average velocity that the gas would have in the axial direction of the reactor without the presence of particles inside it, and the apparent solids velocity (U_s) defined as:

$$U_s = \frac{G_s}{\rho_p} \tag{3.1}$$

where G_s stands for the solids circulating rate (the mass flow rate divided by the section of the fluidized bed) and ρ_p is the particle density. In the diagram, the CFB region is divided vertically into two-regimes, the low-density CFB, for low solids circulating rates, and the high-density CFB, for high solids circulating rates.

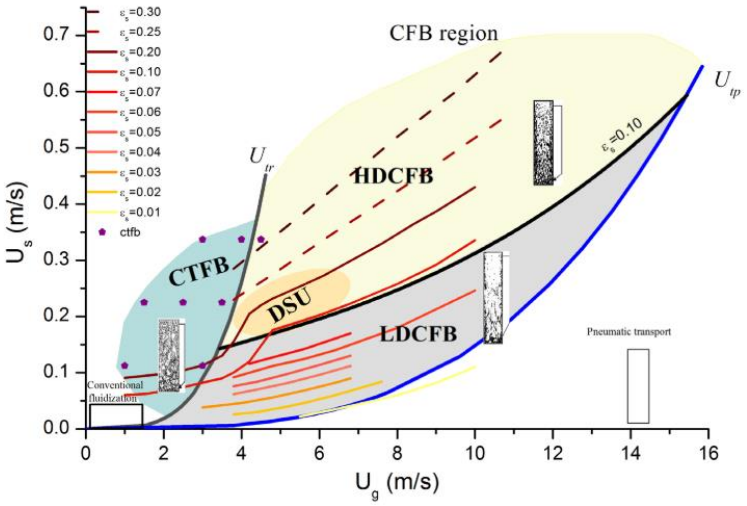

Figure 19. Diagram for the classification of flow regimes of CFB. CFB: circulating fluidized bed where U_g is the superficial gas velocity called U_0 in this study. CTFB: circulating turbulent fluidized bed. DSU: dense suspension flow. HDCFB, high-density circulating fluidized bed. LDCFB, low-density circulating fluidized bed.

3.1.2. Calcium looping fluidized bed facilities

To assess the type of regime needed in the calciner, it was necessary to review the available lab-scale CaL systems for post-combustion CO_2 capture technologies given that no CFB solar reactors were found for calcination purposes. In CO_2 capture the main focus is the carbonator where particles of CaO absorb CO_2 from the flue gas. However, it requires a combustor-calciner to carry out oxy-combustion and drive the calcination reaction. Both reactors are interconnected as shown in Figure 20.

Table 6 summarizes the operating conditions of lab- and pilot-scale CaL systems. Lab-scale are distinguished from pilot-scale plants based on their size and heating mode, i.e. low power range and generally heated by external means (electrical heating systems). Therefore, the selection of the operating conditions of the reactor of this study is based on lab-scale plants based on the similarity of being externally heated and their size. Nevertheless, both lab- and pilot-scale calciners are designed

for low solids circulation rates, i.e. less than 30 kg m^{-2} s^{-1}, and with superficial gas velocities varying from 1.5 - 6 m s^{-1}. Assuming the density of the particles like the one from $CaCO_3$, i.e. 1320 $kg.m^{-3}$, the calciners reviewed fall in the low-density CFB region from the classification of Sun and Zhu [33]. Therefore, the calciner of this model will be designed for the low-density regime.

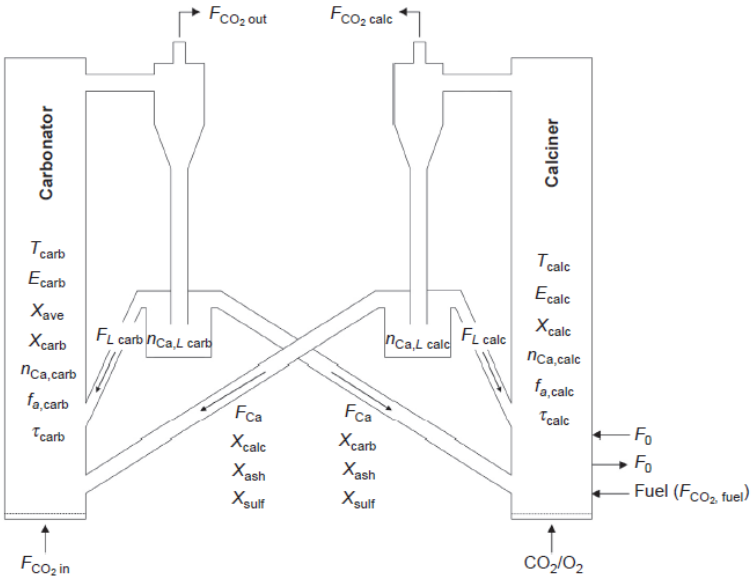

Figure 20. Schematic of the CaL system showing operating variables in the reactors [36].

Table 6. Review of the design and operating conditions of Lab- and pilot-scale CaL facilities.

		Size (kWth)	Diameter (m)	Height (m)	T (°C)	Inlet CO_2 content (%vol)	U_0 (m s^{-1})	U_s (m s^{-1})	Ref.
Lab-scale	Consejo Superior de Investigaciones Científicas	30	0.1	6	800-1000	15-16	1.5 - 3.5	0.001	[8], [37], [38]
	IFK at University of Stuttgart	10	0.071	12.4	850-900	15	4 - 6	0.006 - 0.02	[37], [39]
	Vienna University of Technology	100	0.08[a]	5	850	-	-	-	[40]
Pilot-scale	La Pereda	1700	0.75	15	820-950	12.5	3 - 5	0.001 - 0.003	[36], [41]
	IFK at University of Stuttgart	200	0.021	10	875-930	15	4 - 6	0.006 - 0.017	[39]
	Darmstadt University of Technology	1000	0.4	11.35	<1000	12-12.6	3- 4.1	-	[42]

3.1.3. Reactors models

The computational models describing CFB reactors that are available in the literature were reviewed by Trendewicz [43]. They can be categorized into four classifications:

Empirical correlations:

Empirical correlations are applied for small-scale systems over a limited range of operating conditions. They describe the axial volumetric fraction profiles of non-reactive flows [44],.[45] .

Mechanistic models:

Mechanistic models are more flexible than empirical correlations as they account for the most influential physical parameters on the flow. These models are simplified as plug flow reactors and core-annulus models describing the solid and gas volume fractions in risers [46].

1-D models:

For 1-D steady-state models, the approach varies. To describe the hydrodynamics along the axial direction, some authors assume uniform hydrodynamics. Others adopt an exponential decay function or experimentally determined functions to describe the solid volumetric fraction, while others use a series of well-mixed compartments with different solids concentrations. These models assume uniformity along the radial direction. The core-annulus model is an improved version of the approaches previously described [38], [47], [48].

Computational Fluid Dynamics models:

These models offer the most detailed description in terms of solid-gas flow. They are usually based on Eulerian-Eulerian approximation. The increasing complexity of the model results in an increased computational cost [48]–[50].

For this work, it was decided to proceed with a 1-D model that follows a core-annulus model for determining the heat transfer coefficient and uses an exponential decay function to describe the hydrodynamics of the flow. This is expected to be enough for creating a tool for design purposes. The hydrodynamic and heat transfer model are explained in sections 3.2.4 and 3.2.7 respectively.

3.2. Proposed Mathematical Model

3.2.1. Overview

In the fast fluidization regime, the carryover of solids is very large and fresh solids are continuously fed to the riser to make up for the loss of the bed solids. In a fast fluidized bed, two regions are encountered: the dense zone, which corresponds to the lower part of the riser where there is almost a constant solids volumetric fraction in the order of 0.15 - 0.22, and the lean zone, which is the zone that follows where solids are entrained and the solids volumetric fraction decreases progressively (Figure 21) [44].

In the lean zone, the flow structure is described as a core-annulus flow pattern. Then the cross-section of the lean zone is further divided into two regions: a dilute core with bed particles transported upwards

by the fluidizing gas, and a dense and smaller annulus region where clusters flow down over the reactor wall. The clusters after traveling a certain distance, dissolve, and detach themselves from the wall to be re-entrained into the core region where they mix with fresh particles at the bed temperature (Figure 21). Based on these considerations the model described in this chapter is proposed.

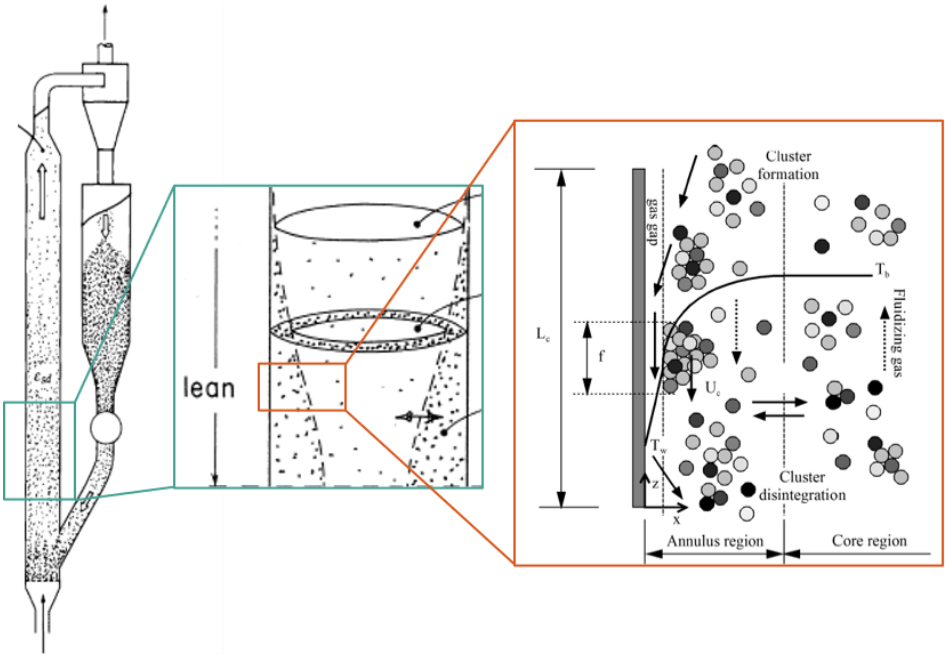

Figure 21. Distribution of solids in the riser of a CFB. The image shows the core annulus regions with the cluster formation and the gas gap over the heat transfer surface. Modified from Kunii and Levenspiel [51] and Blaszczuk [52].

3.2.2. Proposed model assumptions

For the implementation of the proposed mathematical model several assumptions where taken:

General

- A control volume of the reactor, dV, is defined as $dV = A\,dz$, where the section A is constant.
- In the balance equations the diffusivity terms are neglected (mass diffusion and heat conduction within the flow)
- The process in the reactor is a steady-state process
- The static pressure inside the reactor due to the particles (suspension) is neglected
- The gas species can be assumed as ideal gases

Flow

- Inside the reactor we have both a dense bed zone and a lean zone; for very fast fluidization the height of the dense zone can be set close to zero
- Both in the dense zone and each dV of the lean zone the thermophysical properties of the flow species are constant
- The volume fraction of the solids in the dense zone is calculated with an experimental correlation

- The volume fraction of the solids in the lean zone, as a function of z, is described by an adaptation of the Kunii and Levenspiel (K-L) model
- The velocity of gas species is the same
- The velocity of the solid species is the same
- The solid particles are considered to be spheres with a single radius

Chemical reactions

- The kinetic constant of the calcination reaction is described by an experimental correlation
- The equilibrium concentration of CO_2 is described by an experimental correlation

Heat transfer

- The lean zone will be described by a core-annulus model
- The heat transfer between the reactor wall and the fluidized bed is modeled with a total heat transfer coefficient for each dV
- The solid and the gas are in thermal equilibrium
- The energy of the flow is due only to its enthalpy (kinetic energy and gravitational potential energy variations neglected)

3.2.3. Mass conservation analysis

The mass balance for steady-state conditions of the control volume (Figure 22) is given by the following equation.

$$\frac{dm_{cv}}{dt} = m\ z\ - m\ z + dz\ + MassSource\ z\ = 0 \tag{3.2}$$

where $MassSource\ z\ =\ r_i\ z\ \ dV = r_i\ z\ \ A\ dz$

m_{cv} is the mass inside the control volume and $r_i(z)$ is the mass generation rate of the i[th] species per unit of volume and A is the cross-section area.

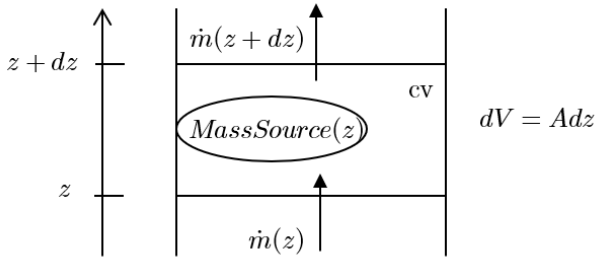

Figure 22. Scheme for the discretization of the CFB riser.

After algebraic manipulation, the mass flow rate of a specie along the reactor height is given by:

$$\frac{m\ z+dz\ -m\ z}{z+dz\ -z}=r_i\ z\ A \tag{3.3}$$

$$\frac{dm(z)}{dz}=r_i\ z\ A \tag{3.4}$$

$$r\ z\ =M_i\ \widetilde{r_i}\ z \tag{3.5}$$

where $r\ z$ is the moles' generation rate of the species per unit of volume and M_i is the molar mass of the species. The moles' generation rate can be rewritten as:

$$\widetilde{r_i}\ z\ =c_s\ z\ \frac{\partial X_i\ z}{\partial t} \tag{3.6}$$

where $c_s(z)$ is the total number of moles of the solid components per unit of volume reactor and $X_i(z)$ is the fraction of the i[th] species in the solids. It is important to note here that $\frac{\partial X_i(z)}{\partial t}$ represents a rate of reaction and not a changing of the species fraction in time, since the steady-state condition assures that, at any instant, a possible change of $X_i(z)$ is compensated by the flow. The fractions of species change only with z.

The species involved in the calcination of $CaCO_3$ are shown in equation (3.7). Calcination of $CaCO_3$ is an endothermic reaction that regenerates the CaO sorbent and produces a concentrated stream of CO_2.

$$CaCO_3(s) \Leftrightarrow CaO(s)+CO_2(g)\quad ;\ \Delta H_{cal}=178.4\ MJ\ kmol^{-1} \tag{3.7}$$

The reaction rate used in the model is proposed by Martinez et al. [53] and Fang et al. [54]. The expression is a function of the difference Δc_{CO_2} of the equilibrium concentration of CO_2 $c_{CO_2,equil}$ and its local concentration c_{CO_2}, the molar fraction of the solid specie X_i and the kinetic constant of $CaCO_3$ calcination k_{calc} in $m^3\ mol^{-1}\ s^{-1}$.

$$\frac{\partial X_i\ z}{\partial t}=\ k_{calc}\ f\ X_i\ \Delta c_{CO_2} \tag{3.8}$$

$$\text{where } \Delta c_{CO_2}=\mathrm{Max}(0, c_{CO_2,equil}-c_{CO_2}) \tag{3.9}$$

$$f\ X_{CaO}\ =\ 1-X_{CaO}\ ^{\frac{2}{3}} \tag{3.10}$$

$$f(X_{CaCO_3})=-(X_{CaCO_3})^{\frac{2}{3}} \tag{3.11}$$

The final differential equation for a given specie is

$$\frac{dm_i(z)}{dz}=M_i\ c_s\ z\ \ k_{calc}\ f\ X_i\ \ \Delta c_{CO_2} A \tag{3.12}$$

where the kinetic constant of the calcination reaction and the equilibrium concentration of CO_2 in the gas are given by empirical correlations,

$$k_{calc}(z) = 2.05 \times 10^3 \; e^{-\frac{1.12\times10^5}{R\,T_b(z)}} \tag{3.13}$$

$$c_{CO_2,eq}(z) = \frac{1.462 \times 10^{11}}{T_b(z)} e^{-\frac{1.913\times10^4}{T_b(z)}} \tag{3.14}$$

where R is the ideal constant gas in J mol-1 K-1 and T_b is the temperature of the bed. Equation (3.12) is rewritten for both solid species and their boundary conditions defined.

$$\frac{dm_{CaO}(z)}{dz} = M_{CaO}\; c_s\; z\; k_{calc}\; \left(1 - X_{CaO}\; z\;\right)^{\frac{2}{3}} \left(c_{CO_2,eq} - \; \mathrm{c}_{CO_2}\right) A \tag{3.15}$$

$$m_{CaO}\; 0\; = \bar{X}_{CaO}\; 0\; m_s\; 0 \tag{3.16}$$

$$\frac{dm_{CaCO_3}(z)}{dz} = \; -M_{CaCO_3} c_s(z)\; k_{calc}\; (X_{CaCO_3}(z))^{\frac{2}{3}}\; \left(c_{CO_2,eq} - \; \mathrm{c}_{CO_2}\right)\; A \tag{3.17}$$

$$m_{CaCO_3}\; 0\; = \left(1 - \bar{X}_{CaO}\; 0\; \right) m_s\; 0 \tag{3.18}$$

$\bar{X}_{CaO}\; 0\;$ is the mass fraction of CaO at the inlet and $m_s\; 0\;$ is the solids mass flow rate at the inlet defined as the sum of the mass flow rates at the inlet of $CaCO_3$ and CaO.

The mass flow rate of CO_2 can be obtained by mass flow rate conservation:

$$m_{CO_2}\; z\; = m_{CO_2}\; 0\; + m_s\; 0\; - m_s\; z \tag{3.19}$$

$$\text{where} \qquad \dot{m}_{CO_2}(0) = \bar{X}_{CO_2}(0)\dot{m}_g(0) \tag{3.20}$$

To solve equations (3.15) and (3.17) it is needed to find equations that describe the solids concentration, which is the total number of moles of the solid components per unit of volume reactor, the molar fraction of CaO, and the local concentration of CO_2. Equations (3.21) - (3.23) are derived using useful identities included in Annex

$$c_s\; \; z\; = c_{CaO}\; z\; + c_{CaCO_3}\; z\; = \frac{1}{U_s\; z\; A}\left(\frac{m_{CaO}\; \; z}{M_{CaO}} + \frac{m_{CaCO_3}\; \; z}{M_{CaCO_3}}\right) \tag{3.21}$$

$$X_{CaO}\; z\; = \frac{\frac{m_{CaO}\; z}{M_{CaO}}}{\frac{m_{CaO}(z)}{M_{CaO}} + \frac{m_{CaCO_3}(z)}{M_{CaCO_3}}} \tag{3.22}$$

$$c_{CO_2}(z) = \frac{m_{CO_2}(z)}{M_{CO_2} U_g(z) A\; \varepsilon_g(z)} \tag{3.23}$$

where U_s and U_g are the velocity of the solids and the gas, ε_g is the gas volumetric fraction.

The velocities of the solids and the gas can be found using the local density of the solid $\rho_s\ z$ and the local density of the gas $\rho_g\ z$. The density of a mixture of species a and b can be calculated as:

$$\rho_{a+b} = \frac{\rho_a \rho_b}{(1-\bar{X}_a)\rho_a + \bar{X}_a \rho_b} \tag{3.24}$$

$$\text{where} \quad \bar{X}_a = \frac{m_a}{m_a+m_b} = \frac{\dot{m}_a}{\dot{m}_a+\dot{m}_b} \tag{3.25}$$

In the case of computing the density of a given gas specie, one can use:

$$\rho_a = \frac{P}{R_a T_b} \tag{3.26}$$

Then, the solids and gas velocities can be found using equations (3.24), (3.25), (3.26):

$$U_s = \frac{m_s}{\rho_s \varepsilon_s A} = \frac{1}{\varepsilon_s(z) A}\left(\frac{m_{CaO}(z)}{\rho_{CaO}} + \frac{m_{CaCO_3}(z)}{\rho_{CaCO_3}}\right) \tag{3.27}$$

$$U_g = \frac{m_g}{\rho_g \varepsilon_g A\ \frac{1}{\varepsilon_g(z) A}\left(\frac{m_{CO_2}(z)}{\rho_{CO_2}(z)} + \frac{m_{N_2}(z)}{\rho_{N_2}(z)}\right)} \tag{3.28}$$

Finally, the superficial gas velocity $U_0\ z$ would be computed as it is needed for the hydrodynamics correlations. The superficial gas velocity is the velocity the gas would have if it occupied the whole section of the reactor.

$$U_0\ z\ \equiv \frac{m_g\ z}{\rho_g\ z\ A} \tag{3.29}$$

3.2.4. Hydrodynamic Model

The hydrodynamics is described by the K-L model from Kunii and Levenspiel [44]. To close the system of equations described in the previous section it is necessary to compute the solid and gas volumetric fraction ε_s and ε_g. To do so, the following equation is used:

$$\varepsilon_{s,lean}\ z\ = \varepsilon_s^* + (\varepsilon_{s,dense} - \varepsilon_s^*) e^{-a\ (z - H_{dense})} \tag{3.30}$$

where the subindex $lean$ and $dense$ are used to denote the dense and lean zone in the riser, ε_s^* is the saturation carrying capacity, a is the decay factor and H_{dense} is the height of the dense bed.

Figure 23 shows a sketch of the profile described by equation (3.30). Parameter a describes the “S” shape of $\varepsilon_s(z)$ in the initial part of the lean zone, ε_s^* is the asymptotic limit of $\varepsilon_s(z)$, corresponding to the saturated carrying capacity of the gas, and H_{dense} is a constant to change from the height z to the height

in the lean zone.

The equation (3.30) is based on data obtained for cold columns without reactions and with constant solids and gas mass flow rates along z, therefore, its use in this model is arguable. For cold columns with constant mass flow rates, the velocities changes are only due to the changes of ε_s and ε_g.To a lower volumetric fraction corresponds a higher velocity in order to keep the mass flow rate constant, and *vice-versa*. The gas velocity starts at its maximum and the solids velocity starts at its minimum. They change monotonically and by construction, they meet at the pneumatic transport conditions.

When the mass flow rate and temperature change with z, as in the case of this study, the velocity has to change accordingly. In this case, the temperature is increasing and the gas mass flow rate is also increasing due to the release of CO_2 Therefore, the K-L model must be adapted in a way that its basics physics is kept but taking into consideration these new factors. For this reason, the following subsections look to give more detail on the needed parameters.

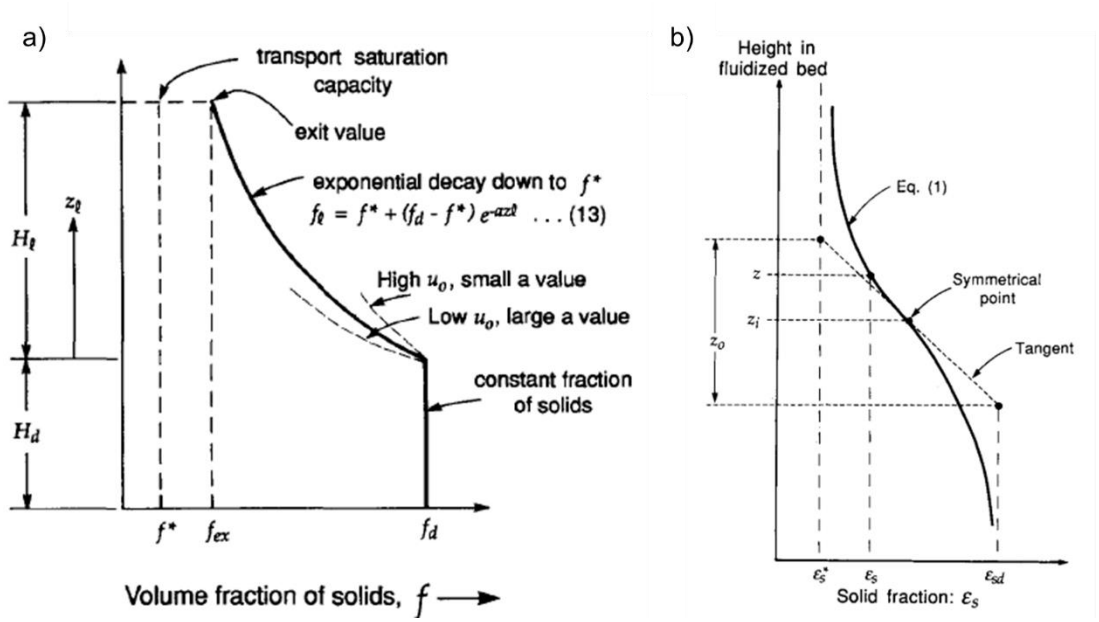

Figure 23. Sketch of the solids volumetric fraction where f and ε are equivalent. a) gives an insight into the variables needed for the K-L model [51] and b) shows the fitted distribution by Li and Kwauk [44]. The decay factor links both correlations and can be computed as $a = \frac{2}{z_0}$.

Solids volumetric fraction in the dense bed

The solids volumetric fraction in the dense zone is computed from a correlation obtained from a graph published by Kunii and Levenspiel [44]. The limits of the superficial gas velocity for the analyzed experimental data are between 1.5 to 5 m s^{-1}. Therefore, a constant value for higher velocities is defined in equation (3.31). The authors conclude that the superficial gas velocity seems not to affect appreciably the fractions of solids in the lower dense region.

$$\varepsilon_{s,dense} = \begin{cases} 0.2369\, U_0\ 0^{\ -0.274} & U_0 \in [1.5\ ;5.0]\ \ \mathrm{m.s^{-1}} \\ 0.15 & U_0 > 5.0\ \mathrm{m.s^{-1}} \end{cases} \tag{3.31}$$

Saturation carrying capacity of the gas

The increase of temperature and mass flow rate of the gas will increase the gas velocity for the saturated carrying capacity condition. For this condition, the velocity of the solids is assumed to be the same as the velocity of the gas, i.e. pneumatic transport. A higher velocity of the solids corresponds to a smaller ε_s^*. This means that the ε_s^* for the reactor studied in this work is smaller than the one expected from the K-L model.

The differences in mass flow rates and densities create a mismatch between the conditions that characterize the "S" curve of $\varepsilon_s(z)$ at the beginning of the lean zone ($a = \frac{2}{z_0}$ where z_0 is depicted in Figure 23.b), and the conditions for the saturated carrying capacity. The $\varepsilon_s(z)$ profile, as predicted by K-L model may not capture the new physics and an impossible solution, with $U_s > U_g$, may occur, even though at the asymptotic limit $U_s^* = U_g^*$ is verified.

The constant a is not a local parameter, it is related to the shape of the "S" curve of $\varepsilon_s(z)$. Using lower values of a avoids $U_s > U_g$. However, the shape of the curve is defined in a short initial part of the lean zone. Forcing a low a seems not appropriate since the problem of the model arises from a low ε_s^*. Artificially increasing ε_s^* is the same as assuming that pneumatic transport will not occur. However, it is known from the literature that for these running conditions the pneumatic transport is a probable reality, even before the asymptotic limit. A better solution may be assuming a pneumatic transport as soon as $\varepsilon_s(z)$, as predicted by the K-L model, leads to $U_s = U_g$. During the pneumatic transport, the velocities will change while chemical reactions or temperature change occur, until $\varepsilon_s\ z\ = \varepsilon_s^*$. It is also important to have in mind that initial simulations and results reported in the literature show that the chemical reactions occur mainly in the first part of the reactor before this condition is verified.

The asymptotic value ε_s^* can be found for the asymptotic conditions, defined when solids and gas have the same velocity, and when complete calcination have been achieved. For a cold fluidized bed, this would be enough but for this case, something has to be assumed regarding the temperature of the bed. Thermal equilibrium with the wall could be a suitable choice. However, this will bring some doubts once the fixed wall temperature approach is abandoned to promote integration with the concentrating solar system. The suggested approach is to find if a wide range of expectable ε_s^* values have a small influence on the simulations results and, if it is so, choose a suitable ε_s^* to be used in the simulations.

To find the expected range of ε_s^*, the temperature of the bed, in equilibrium with the wall, was tested within the interval $T^* \in [650\ ;\ 1000]$ ℃ using the following equations. Firstly, the assumption of pneumatic transport for the saturated carrying capacity corresponds to

$$U_s^* = U_g^* \simeq U_0^* \tag{3.32}$$

where the superscript * corresponds to the saturated carrying capacity conditions. The solids volume fraction can be found as:

$$\varepsilon_s^* = \frac{m_s^*}{\rho_s^* U_g^* A} \simeq \frac{m_s^*}{\rho_s^* U_0^* A} \tag{3.33}$$

where the solids mass flow rate m_s^*, the density of the solid ρ_s^* and the superficial gas velocity U_0^* under saturated carrying capacity condition will be found as follows. The mass flow rate of solids corresponds to the mass flow rate of CaO, which is the initial value plus the converted $CaCO_3$.

$$m_s^* = m_{CaO}\ 0\ + n_{CaCO_3}\ 0\ M_{CaO} = m_{CaO}\ 0\ + \frac{M_{CaO}}{M_{CaCO_3}} m_{CaCO_3}\ 0 \tag{3.34}$$

The density of the solids is the density of CaO:

$$\rho_s^* = \rho_{CaO} \tag{3.35}$$

The velocity U_0^* can be found applying equation (3.29) to this case and taking into consideration that the mass flow rate of gas is the initial one plus the mass flow rate of CO_2 released in the complete calcination process:

$$U_0^* = \frac{m_g^*}{\rho_g^* A} = \frac{m_g(0) + n_{CaCO_3}\ 0\ M_{CO_2}}{\rho_g^* A} = \frac{m_g(0) + \frac{M_{CO_2}}{M_{CaCO_3}} m_{CaCO_3}(0)}{\rho_g^* A} \tag{3.36}$$

The gas density is found using equations (3.24), (3.25), and (3.26):

$$\rho_g^* = \frac{\rho_{CO_2}^* \rho_{N_2}^*}{(1 - \overline{X}_{CO_2}^*)\rho_{CO_2}^* + \overline{X}_{CO_2}^* \rho_{N_2}^*} \tag{3.37}$$

$$\text{where}\quad \overline{X}_{CO_2}^* = \frac{m_{CO_2}^*}{m_g^*} = \frac{m_{CO_2}(0) + \frac{M_{CO_2}}{M_{CaCO_3}} m_{CaCO_3}(0)}{m_g(0) + \frac{M_{CO_2}}{M_{CaCO_3}} m_{CaCO_3}(0)} \tag{3.38}$$

$$\rho_{N_2}^* = \frac{P}{R_{N_2} T^*} \tag{3.39}$$

$$\rho_{CO_2}^* = \frac{P}{R_{CO_2} T^*} \tag{3.40}$$

Decay factor

The parameter a is presented in the literature as depending on a constant gas superficial velocity, which

is not the case in this study. However, its value doesn't change too much in the lean zone, therefore, an estimative will be made with a sensitivity study. For the estimative one could consider the value of U_0 at the midpoint of the lean zone. However, to find it an initial simulation has to be done. Another possible approach is to use the range of a that can be found in the experimental literature. Kunii and Levenspiel [44] present experimental results from Lu and Wang (1985) for running conditions similar to the ones in this study, although with constant mass flow rates. Based on those results, a lies in the interval $a \in \left[\frac{4}{U_0};\frac{12}{U_0}\right]\ \mathrm{m}^{-1}$. The final selection for the reference case will be discussed in the next chapter.

Pneumatic transport condition

In the proposed adapted K-L model, after $U_s = U_g$ is achieved for the first time one has pneumatic transport. Then, ε_s is found from equations:

$$\frac{1}{\varepsilon_s(z)A}\left(\frac{m_{CaO}(z)}{\rho_{CaO}}+\frac{m_{CaCO_3}(z)}{\rho_{CaCO_3}}\right)=\frac{1}{1-\varepsilon_s(z)\ A}\left(\frac{m_{CO_2}(z)}{\rho_{CO_2}(z)}+\frac{m_{N_2}(z)}{\rho_{N_2}(z)}\right) \tag{3.41}$$

$$\varepsilon_s\ z\ =\frac{\left(\frac{m_{CaO}\ z}{\rho_{CaO}}+\frac{m_{CaCO_3}\ z}{\rho_{CaCO_3}}\right)}{\left(\frac{m_{CaO}\ z}{\rho_{CaO}}+\frac{m_{CaCO_3}\ z}{\rho_{CaCO_3}}\right)+\left(\frac{m_{CO_2}\ z}{\rho_{CO_2}\ z}+\frac{m_{N_2}\ z}{\rho_{N_2}\ z}\right)} \tag{3.42}$$

3.2.5. Molar calcination efficiency and residence time of solids

One of the objectives of the model is to determine the calciner efficiency to be able to measure the performance of the reactor. The molar calcination efficiency η_{calc} can be understood as the fraction of $CaCO_3$ calcined in the reactor and it is calculated as:

$$\eta_{calc}\equiv\frac{X_{CaCO_3}\ 0\ -X_{CaCO_3}\ H_t}{X_{CaCO_3}\ 0} \tag{3.43}$$

where H_t is the total height of the reactor. The efficiency of the reactor is correlated with the solids residence time. It is expected that the longer the residence time is the higher the efficiency would be. Therefore, the residence time of solids can be computed as:

$$\frac{dt(z)}{dz}=\frac{1}{U_s(z)} \tag{3.44}$$

3.2.6. Energy conservation analysis

The energy balance of the control volume depicted in Figure 24 is given by the following equation.

$$\frac{dE_{cv}}{dt}=mh\ z\ -mh\ z+dz\ +PowerSource\ z\ +Heat\ transfer\ z \tag{3.45}$$

where the $PowerSource\ z\ =-H_{calcination}\ z\ $ is the heat power consumed in the calcination process in

the control volume, $Heat\ transfer(z)$ is the heat power transferred from the wall to the control volume, and h is the enthalpy.

$$H_{calcination}\ z\ = H_{calc}\ z\ dz = r_{CaO}\ z\ \frac{\Delta H_{calc}}{M_{CaO}} Adz \tag{3.46}$$

where $\frac{\Delta H_{calc}}{M_{CaO}}$ is the energy necessary for the calcination process per kg of produced CaO and $r_{CaO}(z)$ is, as defined for the mass balance (3.5), the mass generation rate of CaO per unit of reactor volume. So, $H_{calc}\ z\ $ is the calcination heat power per dz.

Solving equation (3.45) for a steady-state process:

$$mh\ z+dz\ - mh\ z\ = H_{transf}\ z\ \ dz - H_{calc}\ z\ Adz \tag{3.47}$$

$$\frac{h(z+dz)-h(z)}{z+dz\ -z} = H_{transf}\ z\ - H_{calc}\ z \tag{3.48}$$

$$m\frac{dh(z)}{dz} = \ H_{transf}\ z\ - H_{calc}\ z \tag{3.49}$$

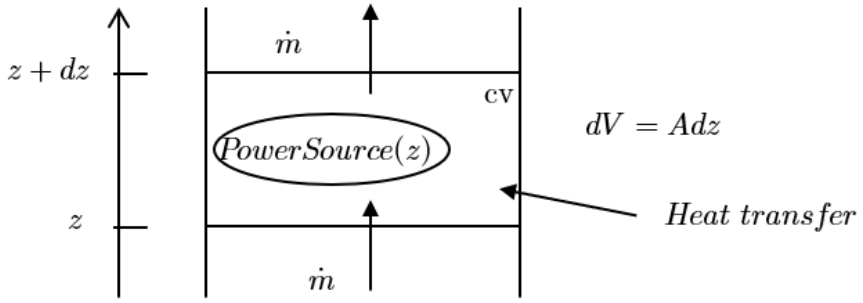

Figure 24. Scheme for the discretization of the CFB riser for the energy conservation analysis.

Both for a solid and an ideal gas, enthalpy is a function of temperature only. Considering a mixture $C_P(z)$

$$mdh = mC_P dT \tag{3.50}$$

The temperature of the bed can be solved as:

$$\frac{dT_b(z)}{dz} = \frac{1}{mC_P(z)}\left(H_{transf}\ z\ - H_{calc}\ z\ \right) \tag{3.51}$$

$$\text{where } mC_P\ z\ = m_{CaCO_3}\ z\ C_{P_{CaCO_3}}\ z\ + m_{CaO}\ z\ C_{P_{CaO}}\ z\ + \\ +m_{N_2}\ z\ C_{P_{N_2}}(z) + m_{CO_2}\ z\ C_{P_{CO_2}}\ (z) \tag{3.52}$$

The calcination heat is found using (3.46), (3.8)-(3.12):

$$H_{calc}\ z\ =\ \Delta H_{calc} c_s\ z\ k_{calc}\ \left(1 - X_{CaO}\ z\ \right)^{\frac{2}{3}} \Delta c_{CO_2} A \tag{3.53}$$

3.2.7. Heat Transfer Model

The heat transfer between the wall and the bed can be written as a function of the heat transfer coefficient from the wall to the bed $h_{w-b}\ z$, which depends on the temperature difference of the wall with the bed for a given control volume, $\Delta T_{cv} = T_{w,cv} - T_{b,cv}$:

$$Heat\ transfer\ z\ = h_{w-b}\ z\ \sum_{cv} A_{transf,cv}\ \Delta T_{cv} = h_{w-b}\ z\ \sum_{cv} \pi\ D\ dz\ \Delta T_{cv} \tag{3.54}$$

where D is the diameter of the reactor. Then,

$$H_{transf}\ z\ = \frac{Heat\ transfer(z)}{dz} = h_{w-b}\ z\ \ \pi\ D\ (T_w - T_b(z)) \tag{3.55}$$

From experimental campaigns in CFB risers, it is known that the walls of the riser are intermittently washed by clusters as explained in section 3.2.1 (Figure 21). Thus at a given time, one part of the wall is covered by clusters and the rest is in contact with a dilute gas-solid stream [55]. Different heat transfer mechanisms are involved: (1) convection/conduction from cluster to wall through a thin gas film (R_1 in Figure 25), (2) radiation from clusters (R_2 in Figure 25), (3) convection, and (4) radiation from the disperse phase (R_5 and R_6 in Figure 25). Figure 25 shows the electrical network analogy for the heat transfer mechanisms involved, R_3 and R_4 are omitted in this model because the temperature of the cluster T_c can be calculated from an empirical correlation.

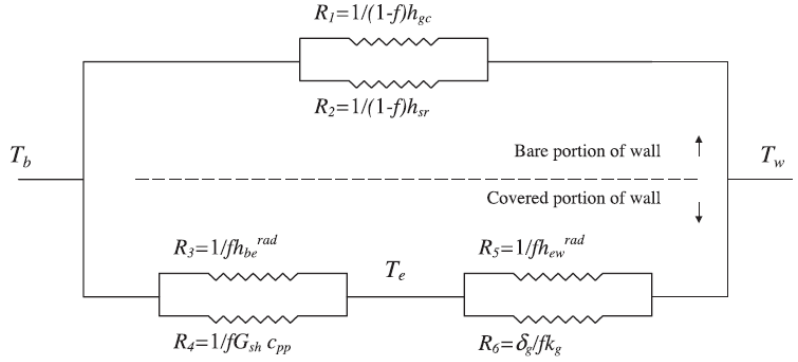

Figure 25. Heat transfer model electrical analogy form. Modified from Chen et. al. [56].

For practical reasons, an overall HTC is computed by summing up the individual heat transfer mechanism while taking into account the fraction of the wall that is in contact with the cluster δ_c while the rest is in contact with the dilute gas-solid stream. The overall HTC between the surface and the fluidized bed is:

$$h_{w-b}\ z\ \ = \delta_c(z)\ (h_c(z) + h_{c,rad}(z)) + (1 - \delta_c(z))(h_{d,con}(z) + h_{d,rad}(z)) \tag{3.56}$$

where the subindices $c,\ d,\ con$, and rad are to denote the cluster phase, dispersed phase, convection,

and radiation respectively. The time-averaged fraction of the wall area covered by the clusters may be estimated as:

$$\delta_c(z) \;=\; 0.5\left(\frac{1-\varepsilon_{cw}(z)-0.00001}{1-\varepsilon_c(z)}\right)^{0.5} \tag{3.57}$$

$$\text{where} \quad \varepsilon_{cw}(z) \;=\; \varepsilon_g^{3.811} \tag{3.58}$$

where ε_c is the gas volumetric fraction within the clusters, and ε_{cw} is the gas volumetric fraction near the wall. The local volume fraction of solids increases continuously from the center toward the wall. The gas fraction near the wall is empirically expressed as in equation (3.57) [57].

Heat transfer coefficient from the dispersed phase

The wall is in contact with the upflowing disperse phase in the space between two clusters. The heat transfer coefficient from a dilute uniform suspension of a gas-solid mixture is used as an approximation as in Basu [58]:

$$h_d(z) \;=\; \frac{k_g\; C_{P_s}(z)}{d_p\; C_{P_g}(z)}\left(\frac{\rho_{dis}(z)}{\rho_s(z)}\right)^{0.3}\left(\frac{U_t^2}{g\; d_p}\right)^{0.21} Pr(z) \tag{3.59}$$

$$\text{where} \quad C_{P,s}(z) = \frac{m_{CaCO_3}(z)\; C_{P,CaCO_3}(z) + m_{CaO}(z)\; C_{P,CaO}(z)}{m_{CaCO_3}(z) + \; m_{CaO}(z)} \tag{3.60}$$

$$C_{pg}(z) = \frac{m_{CO_2}\; z \;\; C_{P,CO_2}(z) + m_{N_2}\; C_{P,N_2}(z)}{m_{CO_2}(z) + \; m_{N_2}} \tag{3.61}$$

where d_p is the particle diameter, k is the thermal conductivity, C_{P} is the specific heat, U_t is the terminal velocity of particles, and g is the gravitational acceleration constant. The density of the dispersed phase ρ_{dis} and the Prandtl number Pr are calculated as follows:

$$\rho_{dis}\; z \;=\; 1-Y \;\; \rho_g\; z \;+Y\; \rho_s\; z \tag{3.62}$$

$$Pr \;\; z \;=\; C_{P,g}\; z \;\; \frac{\mu_g\; z}{k_g \;\; z} \tag{3.63}$$

where Y is the solid volumetric fraction of the disperse phase in the vicinity of the wall. Basu [58] found that a value of $Y = \; 0.001\,\%$ correlated well with experimental data, nevertheless, the author found that the HTC is insensitive to Y.

The heat transfer coefficient of the radiation from the dispersed phase to the wall $h_{dis,rad}$ is computed based on the effective emissivity of a particle cloud considering scattering. Then the bed emissivity e_{dis} is calculated as in Brewster [59]:

$$h_{dis,rad}\ z\ = \frac{\sigma\ (T_b^4\ z\ - T_w^4)}{(\frac{1}{e_{dis}} + \frac{1}{e_w} - 1)(T_b\ z\ - T_w\ z\ )} \tag{3.64}$$

$$e_{dis} = \left[\frac{e_s}{0.5\ \ 1 -\ e_s}\left(2 + \frac{e_s}{0.5\ \ 1 - e_s}\right)\right]^{0.5} - \frac{e_s}{0.5\ 1 - e_s} \tag{3.65}$$

where e_w and e_s are the emissivity of the wall and the particle surface respectively. A coefficient of 0.5 was selected to compute e_{dis}, i.e. for isotropic scattering on the surface of the particles.

Heat transfer from the cluster

The clusters are assumed to travel a certain distance, move away from the wall, disintegrate, and reform periodically in the riser [55]. While the cluster is in contact with the wall, it initially has the temperature of the bed. After that, a transient heat transfer between the wall and the cluster occurs. Initially, the first layer of clusters at the wall is involved and their temperature approaches the temperature of the wall due to conduction. Particles of subsequent layers will also participate in this process if enough time is given [58].

The heat transfer from the cluster involves both the contact resistance on the wall and the conduction resistance of the cluster. The contact resistance corresponds to the thermal resistance offered by a gas film of a thickness that is a fraction of the particle diameter [58]. Then, the heat transfer coefficient from the cluster to the wall is:

$$h_c\ z\ = \frac{1}{\left(\frac{\pi\ t_c}{4k_c\ z\ \ \rho_c\ z\ \ C_{P_c}\ z}\right)^{0.5} + \frac{d_p}{10\ K_{gf}\ z}} \tag{3.66}$$

where t_c is the average residence time of clusters on the wall, and K_{gf} is the thermal conductivity of gas in W m^{-1} K^{-1} evaluated at the mean gas-film temperature $T_{filmavg}$:

$$T_{filmavg}\ z\ \ = \frac{T_b\ z\ \ +\ T_w}{2} \tag{3.67}$$

$$\begin{aligned} K_{gf}\ z\ \ = \ & \left(1.5207 \times 10^{-11}\ T_{filmavg}^3\ z\ - 4.8574 \times 10^{-8}\ T_{filmavg}^2\ z\right. \\ & \left. + 1.0184 \times 10^{-4}\ T_{filmavg}\ z\ - 0.00039333\right)\ 10^{-3} \end{aligned} \tag{3.68}$$

The remaining variables needed for the computation of equation (3.65) are found as follows:

$$k_c\ z\ = k_g\left(1 + \frac{\left(1 - \varepsilon_{g,c}\ z\ \right)\left(1 - \frac{k_g}{k_s}\right)}{\frac{k_g}{k_s} + 0.28\ \varepsilon_c^{0.63\left(\frac{k_g}{k_s}\right)^{0.18}}}\right) + 0.1\ \rho_g\ z\ \ C_{P_g}\ z\ \ d_p\ U_{mf}\ z \tag{3.69}$$

$$\varepsilon_{g,c}\ z\ = 1 - 1.23\left(1 - \varepsilon_{\mathrm{g}}\ z\ \right)^{0.54} \tag{3.70}$$

$$C_{P_c}\ z\ = \left(1 - \varepsilon_c\ z\ \right)C_{P_s}\ z\ + \varepsilon_c\ C_{P_g}\ z \tag{3.71}$$

$$\rho_c\ z\ = \left(1 - \varepsilon_c\ z\ \right)\rho_s\ z\ + \varepsilon_c\ z\ \rho_g\ z \tag{3.72}$$

The minimum fluidization velocity U_{mf}, is the superficial gas velocity at which the bed turns just fluidized and is computed with the correlation of Grace [60]:

$$U_{mf}(z) = \frac{\mu(z)}{d_p\ \rho_g(z)}\left[\left(27.2^2 + 0.0408\frac{\rho_g(z)\ \left(\rho_s(z) - \rho_g(z)\right)g d_p^3}{\mu_g^2(z)}\right)^{0.5} - 27.2\right] \tag{3.73}$$

The heat transfer coefficient of the radiation from the clusters to the wall $h_{c,rad}$ is computed based on the emissivity of clusters considering multiple reflections of particles e_c and the temperature of the cluster T_c, as in Grace [60] and Basu [61] respectively:

$$h_{c,rad}\ z\ = \frac{\sigma\ (T_c^4\ z\ - T_w^4)}{(\frac{1}{e_c} + \frac{1}{e_w} - 1)(T_c\ z\ - T_w)} \tag{3.74}$$

$$e_c = 0.5\ \ 1 + e_s \tag{3.75}$$

$$T_c\ z\ \ = \ T_w\ + 1.29\left(\frac{\rho_{susp}\ z}{\rho_s\ z}\right)^{0.13}(T_b\ z\ \ - \ T_w) \tag{3.76}$$

$$\rho_{susp}\ z\ = \varepsilon_s\ z\ \ \rho_s\ z\ + \varepsilon_g\ z\ \ \rho_g\ z \tag{3.77}$$

where ρ_{susp} is the average suspension density.

3.3. Numerical solution of the mathematical model

The problem presented in this chapter is an initial value problem with stiff ODEs. A problem is stiff if the solution being sought varies slowly, but there are nearby solutions that vary rapidly, so the numerical method must take small steps to obtain satisfactory results [62]. Several numerical methods have been proposed for solving stiff systems, being the Backward Differentiation Formulas method by Gear [63] the most popular stiff solver used in MATLAB. Therefore, ode15s will be the solver used for the solution of the ODE system. The boundary conditions of the problem are defined in the following chapter of this work.

The proposed mathematical model is constituted by four ODE, i.e. equations (3.14), (3.16), (3.43), and (3.50), and around 30 equations for the calculation of needed variables. Table 7 summarizes the equations to be modeled. To use the inbuilt MATLAB ode15s solver the following steps were required:

1) Construction of the ODE function which has input arguments and returns the value of the derivatives of the ODEs. Inside this function, the equations described in this chapter are coded and computed for each step. The ODEs are coupled in a system of equations.
2) Call the ODE solver by passing the needed variables and parameter, i.e. the ODE function that returns the value of the derivative, the range for which the problem is to be solved which is the height of the reactor, and the initial conditions for each ODE.
3) Lastly, store the values of interest by extracting them from the solution in form of a matrix and plot.

Table 7. Summary of the proposed model equations.

Mass conservation

$$\frac{dm_{CaO}(z)}{dz} = M_{CaO}\, c_s\ z\ k_{calc}\ (1 - X_{CaO}\ z\ )^{\frac{2}{3}}\ (c_{CO_2,eq} - \ c_{CO_2})A$$

$$\frac{dm_{CaCO_3}\ z}{dz} = \ -M_{CaCO_3} c_s(z)\ k_{calc}\ (X_{CaCO_3}(z))^{\frac{2}{3}}\ (c_{CO_2,eq} - \ c_{CO_2})\ A$$

$$m_{CO_2}\ z\ = m_{CO_2}\ 0\ + m_s\ 0\ - m_s\ z$$

$$c_s\ \ z\ = \frac{1}{U_s\ z\ A}\left(\frac{m_{CaO}\ \ z}{M_{CaO}} + \frac{m_{CaCO_3}\ \ z}{M_{CaCO_3}}\right)$$

$$X_{CaO}\ z\ = \frac{\frac{m_{CaO}\ z}{M_{CaO}}}{\frac{m_{CaO}\ z}{M_{CaO}} + \frac{m_{CaCO_3}\ z}{M_{CaCO_3}}}$$

$$k_{calc} = 2.05 \times 10^3\ e^{-\frac{1.12\times10^5}{R\ T_b}}$$

$$c_{CO_2}(z) = \frac{m_{CO_2}(z)}{M_{CO_2} U_g(z) A\ \varepsilon_g(z)}$$

$$c_{CO_2,eq} = \frac{1.462 \times 10^{11}}{T_b} e^{-\frac{1.913\times10^4}{T_b}}$$

$$U_s = \frac{m_s}{\rho_s \varepsilon_s A} = \frac{1}{\varepsilon_s\ z\ A}\left(\frac{m_{CaO}\ z}{\rho_{CaO}} + \frac{m_{CaCO_3}\ z}{\rho_{CaCO_3}}\right)$$

$$U_g = \frac{m_g}{\rho_g \varepsilon_g A\ \frac{1}{\varepsilon_g\ z\ A}\left(\frac{m_{CO_2}\ z}{\rho_{CO_2}\ z} + \frac{m_{N_2}\ z}{\rho_{N_2}\ z}\right)}$$

$$\eta_{calc} \equiv \frac{X_{CaCO_3}\ 0\ - X_{CaCO_3}\ H_t}{X_{CaCO_3}\ 0}$$

$$\frac{dt(z)}{dz} = \frac{1}{U_s(z)}$$

Hydrodynamics

$$\varepsilon_{s,lean}\ z\ = \varepsilon_s^* + (\varepsilon_{s,dense} - \varepsilon_s^*) e^{-a\ (z - H_{dense})}$$

$$U_0\ z\ \equiv \frac{m_g\ z}{\rho_g\ z\ A}$$

$$\varepsilon_{s,dense} = \begin{cases} 0.2369\ U_0\ 0\ ^{-0.274} & U_0 \in [1.5\ ;5.0]\ \ \mathrm{m.s^{-1}} \\ 0.15 & U_0 > 5.0\ \mathrm{m.s^{-1}} \end{cases}$$

$$\varepsilon_s\ z\ = \frac{\left(\frac{m_{CaO}\ z}{\rho_{CaO}} + \frac{m_{CaCO_3}\ z}{\rho_{CaCO_3}}\right)}{\left(\frac{m_{CaO}\ z}{\rho_{CaO}} + \frac{m_{CaCO_3}\ z}{\rho_{CaCO_3}}\right) + \left(\frac{m_{CO_2}\ z}{\rho_{CO_2}\ z} + \frac{m_{N_2}\ z}{\rho_{N_2}\ z}\right)}$$

Energy Conservation

$$\frac{dT\ z}{dz} = \frac{1}{mC_P\ z}\left(H_{transf}\ z\ - H_{calc}\ z\ \right)$$

$$mC_P\ z\ = m_{CaCO_3}\ z\ C_{P_{CaCO_3}}\ z\ + m_{CaO}\ z\ C_{P_{CaO}}\ z\ + + m_{N_2}\ z\ C_{P_{N_2}}\ z\ + m_{CO_2}\ z\ C_{P_{CO_2}}\ (z)$$

$$H_{calc}\ z\ = \ \Delta H_{calc} c_s\ z\ k_{calc}\ (1 - X_{CaO}\ z\ )^{\frac{2}{3}}(c_{CO_2,eq} - \ c_{CO_2})A$$

$$H_{transf}\ z\ = h_{w-b}\ z\ \pi\ D\ (T_w - T_b(z))$$

Heat Transfer Model

$$h_{w-b}\ z\ \ = \delta_c\ z\ \left(h_c\ z\ + h_{c,rad}\ z\ \right) + (1 - \delta_c\ z\ )\left(h_{d,con}\ z\ + h_{d,rad}\ z\ \right)$$

$$\delta_c\ z\ =\ 0.5\left(\frac{1 - \varepsilon_{cw}\ z\ - 0.00001}{1 - \varepsilon_c\ z}\right)^{0.5}$$

$$\varepsilon_{cw}\ z\ =\ \varepsilon_g^{3.811}$$

$$h_d\ z\ = \frac{k_g\ C_{P_s}\ z}{d_p\ C_{P_g}\ z}\left(\frac{\rho_{dis}\ z}{\rho_s\ z}\right)^{0.3}\left(\frac{U_t^2}{g\ d_p}\right)^{0.21} \mathrm{Pr}\ z$$

where $C_{P,s}\ z$

$$= \frac{m_{CaCO_3}\ z\ C_{P,CaCO_3}\ z\ + m_{CaO}\ z\ C_{P,CaO}\ z}{m_{CaCO_3}\ z\ +\ m_{CaO}\ z}$$

$$C_{pg}\ z\ = \frac{m_{CO_2}\ z\ \ C_{P,CO_2}\ z\ + m_{N_2}\ C_{P,N_2}\ z}{m_{CO_2}\ z\ +\ m_{N_2}}$$

$$\rho_{dis}\ z\ =\ 1 - Y\ \ \rho_g\ z\ + Y\ \rho_s\ z$$

$$Pr\ \ z\ =\ C_{P,g}\ z\ \ \frac{\mu_g\ z}{k_g\ \ z}$$

$$h_{dis,rad}\ z\ = \frac{\sigma\ \ T_b^4\ z\ - T_w^4}{\left(\frac{1}{e_{dis}} + \frac{1}{e_w} - 1\right)\left(T_b\ z\ - T_w\ z\ \right)}$$

$$e_{dis} = \left[\frac{e_s}{0.5\ \ 1 - \ e_s}\left(2 + \frac{e_s}{0.5\ \ 1 - e_s}\right)\right]^{0.5} - \frac{e_s}{0.5\ 1 - e_s}$$

$$h_c\ z\ = \frac{1}{\left(\frac{\pi\ t_c}{4k_c\ z\ \ \rho_c\ z\ \ C_{P_c}\ z}\right)^{0.5} + \frac{d_p}{10\ K_{gf}\ z}}$$

$$T_{filmavg}\ z\ \ = \frac{T_b\ z\ \ +\ T_w}{2}$$

$$K_{gf}\ z\ \ =\ 1.5207 \times 10^{-11}\ T_{filmavg}^3\ z\ -$$

$$-4.8574 \times 10^{-8}\ T_{filmavg}^2\ z\ + 1.0184 \times 10^{-4}\ T_{filmavg}\ z\ -$$

$$-0.00039333$$

$$k_c\ z\ = k_g\left(1 + \frac{\left(1 - \varepsilon_{g,c}\ z\ \right)\left(1 - \frac{k_g}{k_s}\right)}{\frac{k_g}{k_s} + 0.28\ \varepsilon_c^{0.63\left(\frac{k_g}{k_s}\right)^{0.18}}} + 0.1\ \rho_g\ z\ \ C_{P_g}\ z\ \ d_p\ U_{mf}\ z\right)$$

$$\varepsilon_{g,c}\ z\ = 1 - 1.23\left(1 - \varepsilon_{\mathrm{g}}\ z\ \right)^{0.54}$$

$$C_{P_c}\ z\ = \left(1 - \varepsilon_c\ z\ \right)C_{P_s}\ z\ + \varepsilon_c\ C_{P_g}\ z$$

$$\rho_c\ z\ = \left(1 - \varepsilon_c\ z\ \right)\rho_s\ z\ + \varepsilon_c\ z\ \rho_g\ z$$

$$U_{mf}(z) = \frac{\mu(z)}{d_p\ \rho_g(z)} \times$$

$$\times\left[\left(27.2^2 + 0.0408\frac{\rho_g(z)\ \left(\rho_s(z) - \rho_g(z)\right) g d_p^3}{\mu_g^2(z)}\right)^{0.5} - 27.2\right]$$

$$h_{c,rad}\ z\ = \frac{\sigma\ \ T_c^4\ z\ - T_w^4}{\left(\frac{1}{e_c} + \frac{1}{e_w} - 1\right)\ T_c\ z\ - T_w}$$

$$e_c = 0.5\ \ 1 + e_s$$

$$T_c\ z\ \ =\ T_w\ + 1.29\left(\frac{\rho_{susp}\ z}{\rho_s\ z}\right)^{0.13}\ \ T_b\ z\ \ -\ T_w$$

$$\rho_{susp}\ z\ = \varepsilon_s\ z\ \ \rho_s\ z\ + \varepsilon_g\ z\ \ \rho_g\ z$$

Chapter 4

Results and Discussion

This chapter presents the discussion of the results obtained from implementing the proposed model in two sections. Section 4.1 presents the results obtained when applying the model assuming a constant wall temperature. As this model was prepared to be coupled in the future with the cavity model and CSP system, a further step is given by imposing a non-uniform heat flux distribution on the wall. These results are presented in section 4.2.

4.1. Model implementation with constant wall temperature

This section starts by presenting the parameters and conditions used in the model by imposing a constant wall temperature. Then, the mass and energy balances were verified by disregarding the reaction and/or heat transfer. Finally, the results for the baseline case and the sensitivity study are presented.

4.1.1. Parameters and conditions of the model

The input parameters and boundary conditions of the model are described in this section for the reference case. Table 8 describes the parameters related to the reactor and the solid-gas flow.

Table 8. Model input of the reactor and solid-gas flow parameters.

	Parameter	Value	Units
Reactor	D	0.1	m
	H	10	m
	e_w	0.8	-
	P	120000	Pa
	T_w	900	°C
Solid	d_p	300	μm
	ρ_{CaCO_3}	1320	kg.m^{-3}
	ρ_{CaO}	870	kg.m^{-3}
	M_{CaCO_3}	0.1	kg.mol^{-1}
	M_{CaO}	0.056	kg.mol^{-1}
	e_s	0.9	-
Gas	M_{CO_2}	0.044	kg.mol^{-1}
	M_{N_2}	0.1	kg.mol^{-1}
	R_{N_2}	296.8	J kg^{-1} K^{-1}
	R_{CO_2}	188.9	J kg^{-1} K^{-1}

Reactor geometry, material properties, and P-T conditions:

The reactor diameter and height were selected based on the literature review of current CaL lab-scale available systems (section 3.1.2). The diameter for lab-scales ranges from 0.07 - 0.1 m for plants with thermal powers between 10 - 30 kW. Reactors in larger plants as La Pereda and TU Darmstadt were not taken into consideration for being pilot-scale plants with capacities of 1 MWth and 1.7 MWth respectively. Similarly, the reactor length for lab-scale calciners is in the range of 6 - 12 m. A value of 10 m height was selected as a reference for design purposes. The final height will be recommended based on the simulation results.

The riser wall is assumed to be of stainless steel with a constant surface temperature of 900 °C. AISI 310S stainless steel was used as reference material to select the emissivity to be inputted in the model, i.e. 0.8 [64]. This type of steel was used for the absorber tube receiver on the experimental setup for an on-sun test on a unit at the 1 MW solar furnace of CNRS (Odeillo Font-Romeu) [65].

The operation of the reactor occurs at atmospheric pressures. The pressure chose for the reference case was 1.2 $\times 10^{-5}$ Pa. From experimental data, it was checked that static pressure inside the reactor due to the particles can be neglected [39]. A constant wall temperature of 900 °C is chosen. This value corresponds to the limit after which sintering of the particles may occur. It is expected that the temperature of the bed reaches the temperature of the wall.

Solids and gas properties and parameters:

The values of the molar masses and mass-specific gas constants for all species were obtained from [66]. The densities of the solids were obtained from laboratory measurement using a sample of sorbent with a particle diameter in the range of 250 - 350 μm. The $CaCO_3$ density measurement was done using a fresh sample. For the measurement of CaO density, a sample resulting from the calcination reaction (after one cycle) was used. The particle diameter selected for the reference case is 200 μm. A sensitivity study will be done over the particle range ($d_p \in [200\ ;\ 400]$) to assess its effect on the process efficiency.

The emissivity of limestone was selected to describe the emissivity of the solids in the model. A value of 0.9 was chosen [66]. Table 9 presents the equations used for the calculation of the heat capacity of the involved species as a function of the temperature.

Table 9. Specific heat of species [67].

Validity range of temperature (K)	Specific heat (kJ kmol-1 K-1)
300<T<2000	$C_{p,\mathrm{CO_2}} = \frac{1}{M_{co2}}\ (43.2915\ +\ 1.1472\times10^{-2}\ T_b\ -\ 818519.4\ T_b^{-2})$ $C_{p,N_2}\ =\ 1027\ +\ 0.02162\ \ \mathrm{T_b}\ +\ 1.486\times10^{-4}\ \ T_b^2\ -\ 4.484\times10^{-8}\ T_b^3$
300<T≤1000	$C_{p,CaCO_3} = -147.0097\ +\ 5.14113\ T_b - 7.33\times10^{-3}\ T_b^2\ +\ 3.83712\times10^{-6}\ T_b^3 - 2.482\times10^{-10}\ T_b^4$ $C_{p,CaO} = 251.1235\ + 2.69093\ T_b - 4.2066\times10^{-3}\ T_b^2 + 3.0414\times10^{-6}\ T_b^3 - 8.181\times10^{-10}\ T_b^4$
1000<T<1200	$C_{p,CaCO_3}\ =\ 1199.445\ -\ 0.1161\ T_b^1\ +\ 1.69741\times10^{-4}\ T_b^2$ $C_{p,CaO}\ =\ 838.5397\ + 0.15071\ \mathrm{T_b}\ -\ 3.7921\times10^{-5}\ T_b^2 + 8.08248\times10^{-9}\ T_b^3 - 6.313\times10^{-13}\ T_b^4$

The gas dynamic viscosity is computed as the simple mass average given that the individual dynamic viscosity of N_2 and CO_2 are almost the same for the temperature range expected in the reactor. It is determined as:

$$\mu_g = [0.0162 + 3.2\times10^{-5}T(\mathrm{°C})]\times10^{-3} \qquad [Pa.s] \tag{4.1}$$

Inlet boundary conditions:

Table 10 presents the boundary conditions of the model. The solids and gas mass flow rates were selected after reviewing the available information on calciners for the CaL process and their cold model studies. The solids circulation rate and the superficial gas velocity ranged from 0.6 - 5 kg m^{-2} s^{-1} and 2 - 5 m s^{-1} respectively [41], [48], [68]. This translates into solids and gas flow rates in the order of 0.02 kg s^{-1}. This value was selected as the reference value. It must be noted that the operating conditions of reactors are given in literature based on constant solids circulation rates and superficial gas velocities. In this model, the superficial gas velocity is calculated and not introduced as an input. In the equations, the superficial gas velocity would be used for the calculation of the decay factor and nothing more. A sensitivity study for m_g and m_s will be presented in the sections to come. The variation range is $m_g\ 0\ \in [0.005\ ;\ 0.025]$ and $m_s\ 0\ \in [0.005\ ;\ 0.025]$.

Table 10. Inlet boundary conditions of the model

Boundary Condition	Value	Units
$m_s(0)$	0.02	m
$m_g(0)$	0.02	m
$x_{CaO}(0)$	0.05	kg.mol^{-1}
$x_{CO2}(0)$	0.2	kg.mol^{-1}
$T_b(0)$	650	°C

The inlet mass fractions of CaO and CO_2, $x_{CaO}\ 0$ and $x_{CO2}(0)$ respectively, were also selected according to experimental data. In the beginning, fresh $CaCO_3$ without any content of CaO is expected

to be used. After the first cycle, the introduced mass flow of solids will correspond to the one recovered from the carbonator which will have a higher content of CaO due to the deactivation of the sorbent. Texeira et al. [69] concluded that the fraction of unreacted CaO is highly dependant on the type of sorbent used. It was found that for CaO precursors as dolomite, the fraction of unreacted CaO was much lower (i.e. 5 - 8 %) when compared with wastes of marble powder (i.e. 20 - 30 %). Therefore, a reference value for the inlet mass fraction of CaO of 5 % is selected. A sensitivity study will be conducted for a range of values of $x_{CaO}\ 0\ \in [0;0.35]$. Similarly, the initial mass fraction of CO_2 selected for the reference case is 0.2. From the literature, it is known that the local concentration of CO_2 highly affects the reaction rate. Therefore, a sensitivity study will be performed for the inlet mass fractions of CO_2 for typical values found in the literature ($x_{CO_2}\ 0\ \in [0\ ;0.4]$) [70].

The temperature of the bed at the inlet is assumed to be 650 °C as this is the temperature of the products at the outlet of the carbonator in CaL processes. However, for thermochemical energy storage in CSP systems, this temperature might drop depending on the time and conditions for storing the products. Therefore, the need for preheating of the sorbent and the fluidizing gas will be also assessed in the sensitivity study ($T_b\ 0\ = [25\ ;\ 650]$).

Hydrodynamics:

As discussed in previous sections, to model the hydrodynamics three parameters must be selected (Table 11), i.e. the height of the dense zone, the decay factor, and the solids fraction at saturated carrying capacity condition.

Table 11. Input parameters of the hydrodynamic model.

Parameter	Value	Units
a	$\frac{4}{U_0\ H_d}$	m
H_d	0.25	m
ε_s^*	2×10^{-4}	-

The height of the dense bed was selected as 0.25 m for the reference case. This value was chosen after reviewing available experimental data from low-density CFB which corresponds to the reactor described in this work. After reviewing the work of Bidwe [39], Charitos et al. [37], Xu et al. [71], and Collado et al. [72], it is expected to have a very small bed of some tens of centimeters or even inexistent. Nevertheless, this parameter will likely affect greatly the calcination efficiency of the reactor, therefore, this input will be evaluated in a sensitivity study by variating its value over the range of $H_d \in [0\ ;\ 0.5]$.

The decay factor is presented in the literature as depending on a constant superficial gas velocity. The reference value was selected based on the experimental results presented by Kunii and Levenspiel [44] where the superficial gas velocity will be calculated at the beginning of the lean zone. Later, a sensitivity study will be performed in the range of the values proposed by the authors ($a \in \left[\frac{4}{U_0\ H_d}\ ;\ \frac{12}{U_0(H_d)}\right]$).

The solids fraction at saturated carrying capacity condition were found in this study assuming that the

particles are fully calcined and that they reach pneumatic transport conditions (i.e. the gas and solids have the same velocity). For high-temperature reactions, as in this case, additional assumptions had to be added regarding the temperature of the bed. The suggested approach presented on pages 31 - 32 allowed finding the expected range of ε_s^* for a temperature interval of 650 - 1000 °C. The obtained range was $\varepsilon_s^* \in [1.8 \times 10^{-4};\ 2.5 \times 10^{-4}\ ]$. It was also verified with this model that the results of the simulation are very insensitive to ε_s^*. The molar calcination efficiency obtained was $\eta \in [0.6802; 0.6810]$ for the interval limits. Therefore, a reference value of 2×10^{-4} will be used.

4.1.2. Tests to verify the proper implementation of mass and energy balances

Test without reaction and heat transfer:

The consistency of the complete mathematical model was tested first disregarding the occurrence of reaction and temperature change. Figure 26.a and b show that the mass flow rate of the components remained equal to the feed conditions throughout the reactor's height, which means that the proposed mass balance equations seem to be consistent. Similarly, Figure 26.c shows a constant temperature of the bed as expected from testing the model without heat transfer between the wall and the bed.

In this test, a constant density of the gas phase and constant mass flow rate is assumed for the whole height of the reactor. For this reason, Figure 26.e shows a constant superficial gas velocity which is usually the assumption used in CaL reactors modeling presented in the literature [38]. This is not the case with the model presented in this work. However, by assuming constant gas density and mass flow rates, it was confirmed that the gas and solids velocities profiles present the expected behavior. In Figure 26.e the gas velocity starts at its maximum and the solids velocity starts at its minimum. They change monotonically due to the changes of ε_s and ε_g until they converge at pneumatic transport conditions.

Test with heat transfer and no reaction

A second test was performed with no reaction to assess the consistency of the energy balance and HTC correlations. Figure 27.a shows the total heat transfer coefficient between the bed and the wall along the axial direction of the reactor. The total HTC varies from 270 to 370 W m^{-2} K^{-1} which is in the range of values suggested in the literature for circulating fluidized beds [65], [58], [73].

In the dense bed, the fraction of cluster is set to zero and the HTC is computed as the contribution of the dense bed as a homogeneous dispersed phase. In the lean zone, the total HTC is computed as the sum of convective and radiative mechanisms from the disperse phase and clusters by taking into account the fraction of clusters at the wall. The cluster convection to the wall is in the order of 0.035 W m^{-2} K^{-1} and is negligible when compared to the other HT mechanisms. This agrees with the results from the example case presented in Basu [58]. Oppositely, the cluster radiation is more significant. The cluster radiation reaches its maximum at the beginning of the lean zone and decreases with the axial direction of the reactor. This is a result of smaller fractions of the wall covered by clusters as one moves up in the axial direction of the reactor. The major contribution is from the radiation and convection of the

disperse phase.

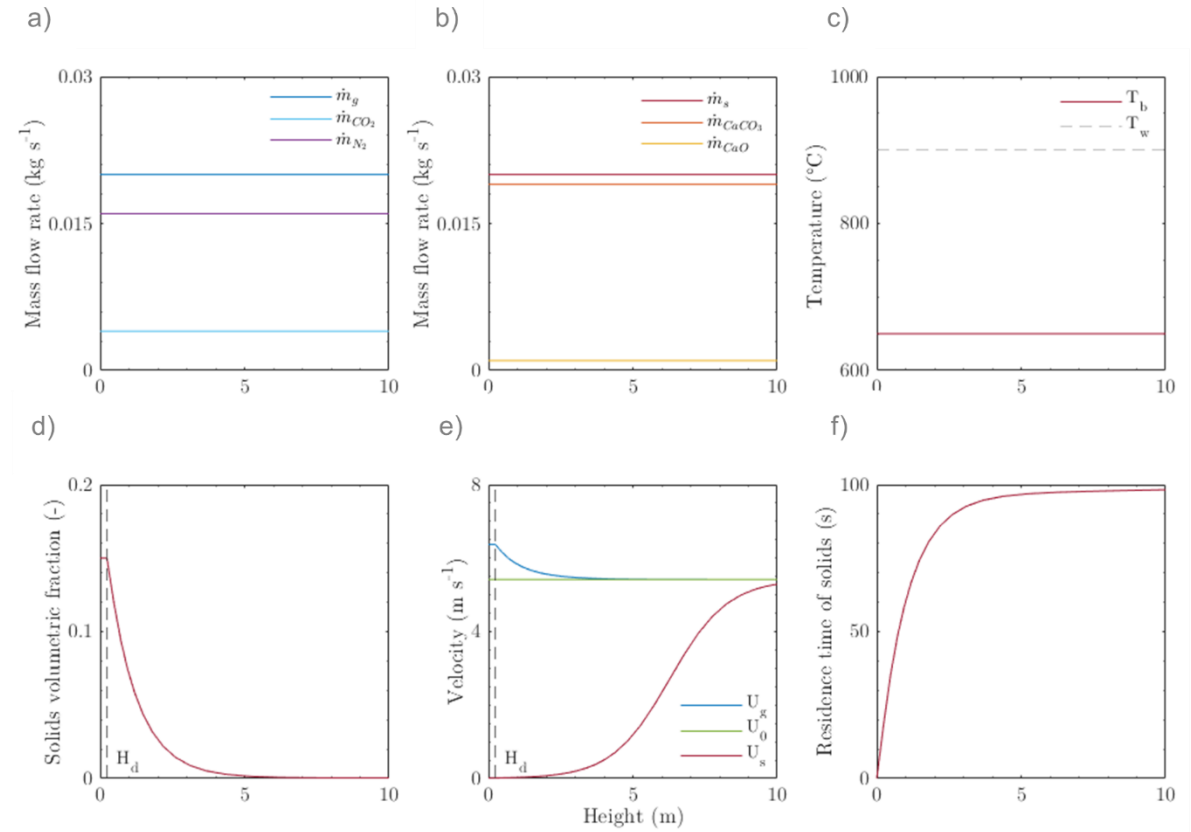

Figure 26. Distribution along the axial direction of the calciner of a) gas mass flow rate, b) solids mass flow rate, c) wall and bed temperature, d) solids volumetric fraction (the dotted line denotes the height of the dense bed (H_d)), e) superficial gas velocity (U_0), solids velocity (U_s) and gas velocity (U_g), f) residence time of the solids. For these results, the calcination reaction and heat transfer between the wall and the bed were disregarded.

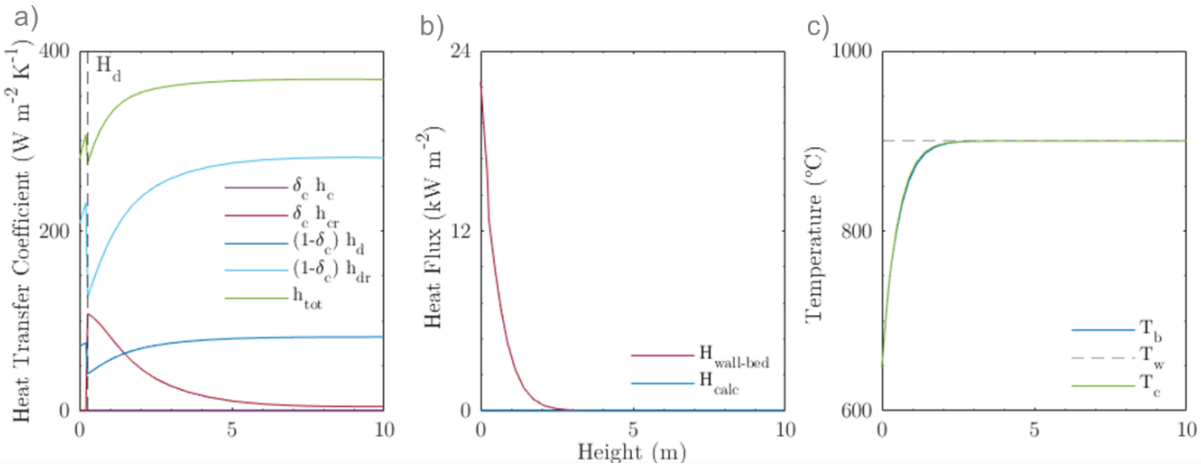

Figure 27. Distribution along the axial direction of the calciner of a) total heat transfer coefficient, b) wall to bed heat flux, and c) temperature profiles of the bed, wall, and clusters. The total HTC is computed as the sum of the convective and radiative contributions from the disperse phase and clusters taking into account the fraction of the wall covered by the clusters (δ_c). For these results, the calcination reaction was disregarded.

Figure 27.b and c show the heat flux from the wall to the bed and the temperature profile of the bed, wall, and clusters. The power required for calcination is as expected from this test and the power from

the wall reaches zero around 3 m height. This is in agreement with the temperature profile of the bed, which rises as the solid and gas phases heat up until reaching equilibrium with the temperature of the wall around that height. Thus, it can be said that the energy balance was properly implemented. It must be remarked that the calculation of gas-to-particle heat transfer was neglected in this model because it was proved after some tests that the gas and solid particles reach a temperature equilibrium at a short distance from the distributor. This is also confirmed in the publications of Rusheljuk [55] and Basu [58].

With an increase in temperature, it is expected that the hydrodynamics in the riser differs from cold model test conditions. Usually, authors use the hydrodynamic model proposed by Kunii and Levenspiel [44] for high-temperature reactive systems by assuming constant densities, constant superficial gas velocity, and constant mass flow rates (Cormos et al. [38], Lasheras et al. [74], Sattari et al. [75]). Under these assumptions, for a lower volumetric fraction, a higher velocity is achieved to keep the mass flow rate constant, and vice-versa.

For a high-temperature system, Figure 28 shows otherwise. A rise in temperature results in an increase of the superficial gas velocity because of the change of the gas density (green line in Figure 28.b). This will be aggravated by the increase of the gas mass flow rate due to the release of CO_2. Furthermore, Figure 28.b shows that the K-L model as it is may not capture the physics of the new problem and an impossible solution, with $U_s > U_g$ can occur, even though the solid and gas velocities converge at the asymptotic limit $U_s^* = U_g^*$. This result justify the need of adapting the K-L model in a way that considers the rise of temperature and variable mass flow rate as presented in section 3.2.4.

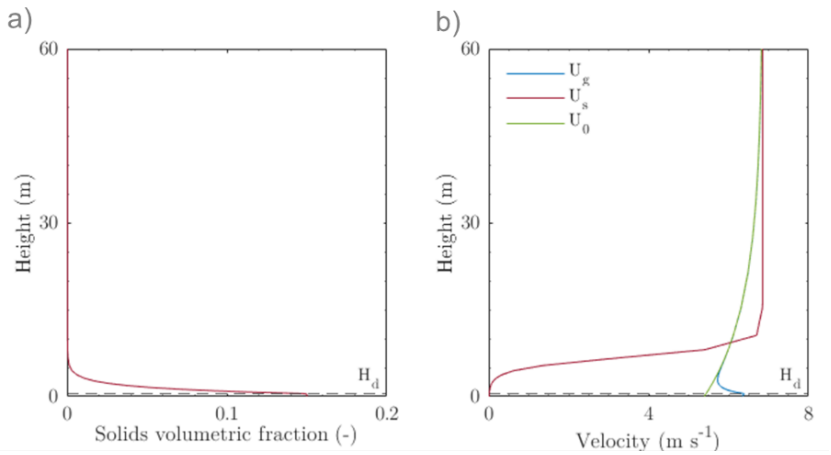

Figure 28. Distribution along the axial direction of the calciner of a) the solids volumetric fraction and b) the superficial gas velocity (U_0), solids velocity (U_s) and gas velocity (U_g). The height of the reactor was exaggerated for this simulation to verify the convergence of the solid and gas velocity at the asymptotic limit $U_s^* = U_g^*$.

Test with reaction and heat transfer considering constant density and molar masses

This case evaluates the molar calcination efficiency obtained when a constant density and constant mass flow rates are assumed. This assumption is employed by several authors for describing the hydrodynamics in the CFB reactor [38], [74], and [75]. The final results show that the molar calcination efficiency obtained at 6 m and 10 m is 0.70 and 0.77 respectively (Figure 29). These results will be

compared in the following section with the ones obtained when using the proposed model of this study, i.e. when densities vary according to temperature and the CO_2 generation from the calcination reaction is accounted for.

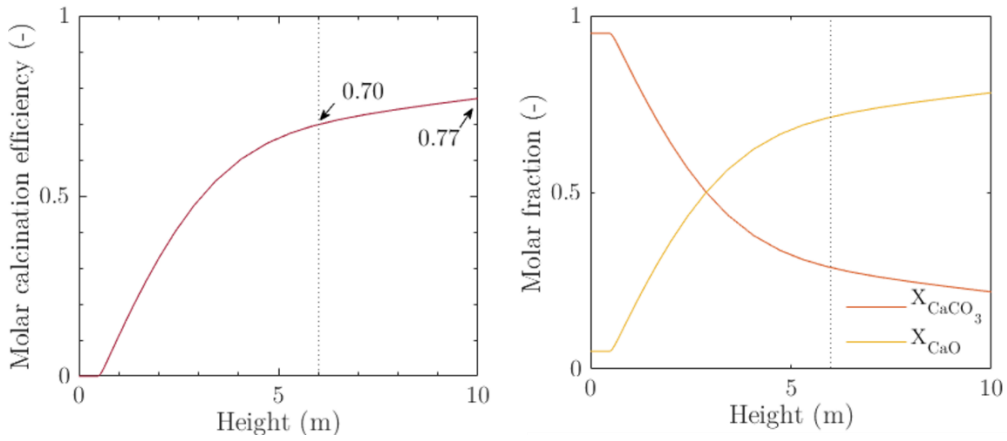

Figure 29. Distribution along the axial direction of the calciner of a) Molar calcination efficiency, and b) molar fraction of solid species. A final efficiency of 0.77 is achieved at the end of the reactor height. For this result, a constant temperature wall of 900 °C is assumed with constant densities and constant gas mass flow rate.

4.1.3. Test with reaction and heat transfer for constant wall temperature

The simulation results for a constant wall temperature with the reactive medium is presented in this section. The kinetic expressions used are from Martinez et al. [76] and Fang et al. [54] as presented in section 3.2.3. Figure 30 (a-c) shows the results related to heat transfer inside the reactor. The total heat transfer coefficient varies from 270 - 350 W m^{-2} K^{-1} and it is in the range of the reported values found in the literature. Figure 30.b shows that the heat flux from the wall to the bed steadily decreases until the reaction starts around 0.4 m. This height does not correspond to the height of the dense bed but to the point where the CO_2 equilibrium concentration surpasses the local CO_2 concentration as noticed in Figure 31.c. The dense bed is assumed to behave as a disperse phase without clusters. Therefore, the temperature of the clusters starts diverging in the lean zone where a value in between the wall temperature and the temperature of the bed until equilibrium is reached.

Figure 30 (d-f) shows the simulation results directly linked to the hydrodynamic model. The volumetric solids fraction at the dense bed is constant and equal to 0.15. This value is in the range reported in the literature for fast fluidized beds, i.e. 0.15 to 0.22 [44]. Figure 30.e shows that the superficial gas velocity changes as a result of the increase in temperature and CO_2 mass generation. Similarly, the velocities profiles of gas and solids change as expected until they reach the pneumatic transport condition and converge at the superficial gas velocity value. From the residence time of the solids profile, it can be seen that the curve flattens after approximately 5 m height which supports the selection of a shorter height for the reactor. This is also endorsed by Figure 31 (a-d) where the driving forces of the reaction are shown. The profile of the reaction rate flattens around 7 meters, however, no significant contribution can be seen after 6 m height.

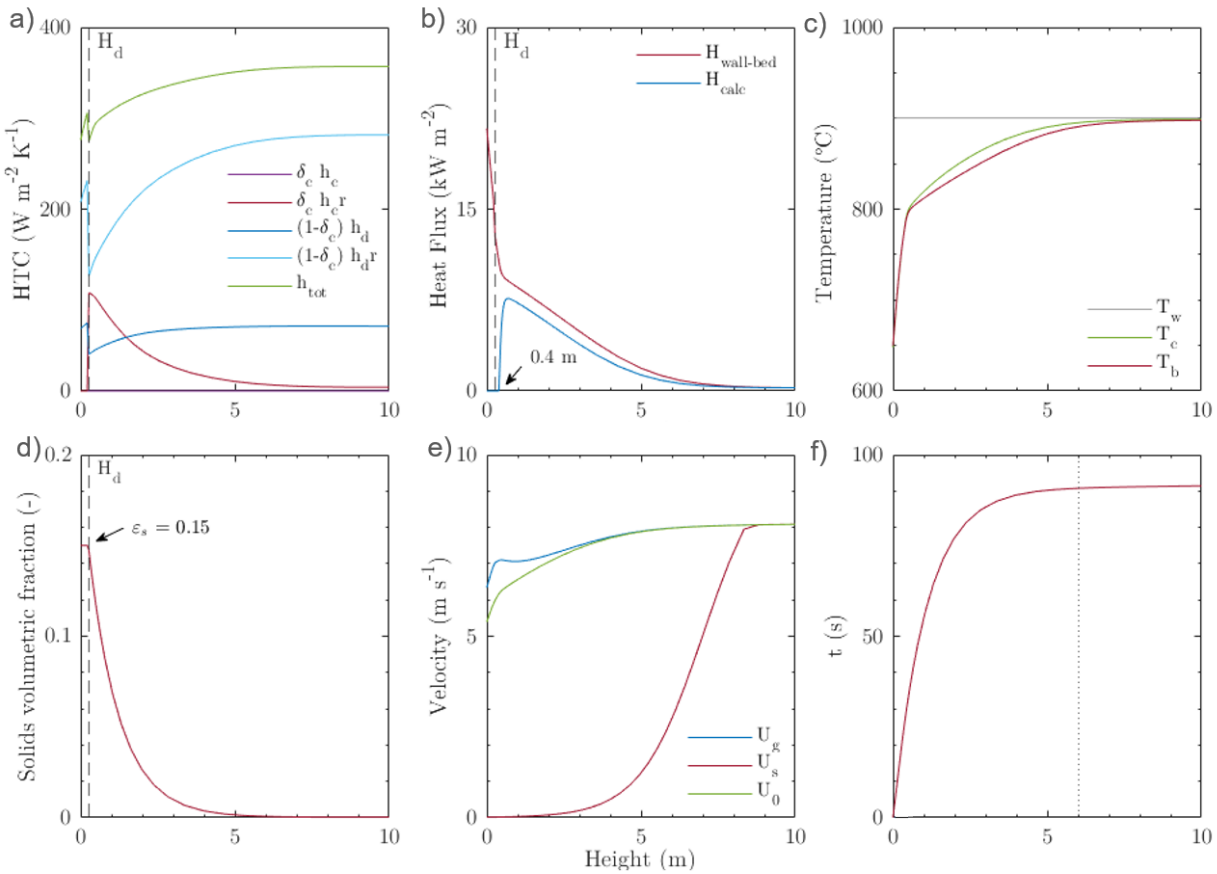

Figure 30. Distribution along the axial direction of the calciner of a) total heat transfer coefficient, b) wall to bed heat flux, and c) temperature profiles of the bed, wall, and clusters, d) the solids volumetric fraction, e) superficial gas velocity (U_0), solids velocity (U_s) and gas velocity (U_g), and f) residence time of the solids. The height of the dense bed (H_d) is shown with a vertical line. For these results, a constant temperature wall of 900 °C is assumed.

The results obtained in Figure 31.c show that the bed temperature and the mass fraction of CO_2 at the inlet are the major factors affecting the conversion (Figure 32) and therefore the molar calcination efficiency (Figure 33.). From the profiles, it is evident that the molar fraction of the species remains constant until 0.4 m, i.e. the height at which the reaction starts. The molar fraction at 6 m and 10 m height for CaO is 0.68 and 0.72 respectively, and for CO_2 is 0.21 and 0.22. Similarly, the molar calcination efficiency at 6 m and 10 m heigh is 0.65 and 0.69. This justifies the selection of a reactor height of around 6 m for the operating conditions under study. However, in the next section, a sensitivity study will be performed over the model parameters to check their effect on the final conversion. Furthermore, these results prove that for this case assuming constant densities and constant mass flow rates, as done by several authors in literature, leads to an overestimation of 5 % points and 8 % points for 6 m and 10 m height respectively (compare Figure 29 and Figure 33). The model presented in this work provides a more conservative result than when applying these simplifications.

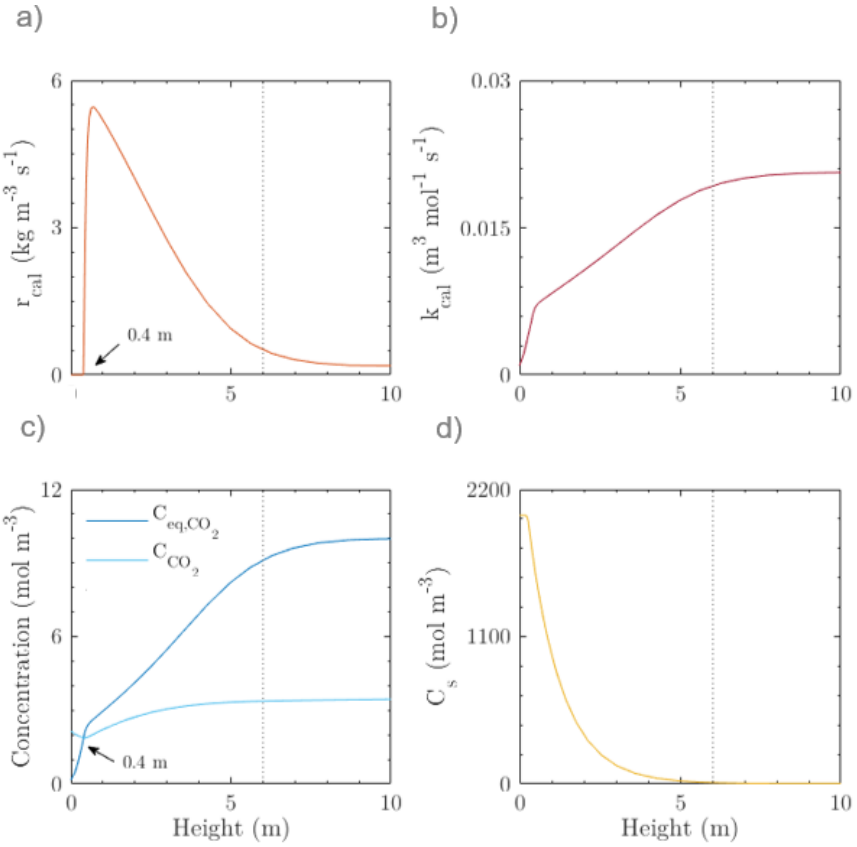

Figure 31. Distribution along the axial direction of the calciner of a) reaction rate, b) kinetic constant of the calcination reaction, c) CO_2 concentration in equilibrium and in the reactor, and d) concentration of solids. For these results, a constant temperature wall of 900 °C is assumed.

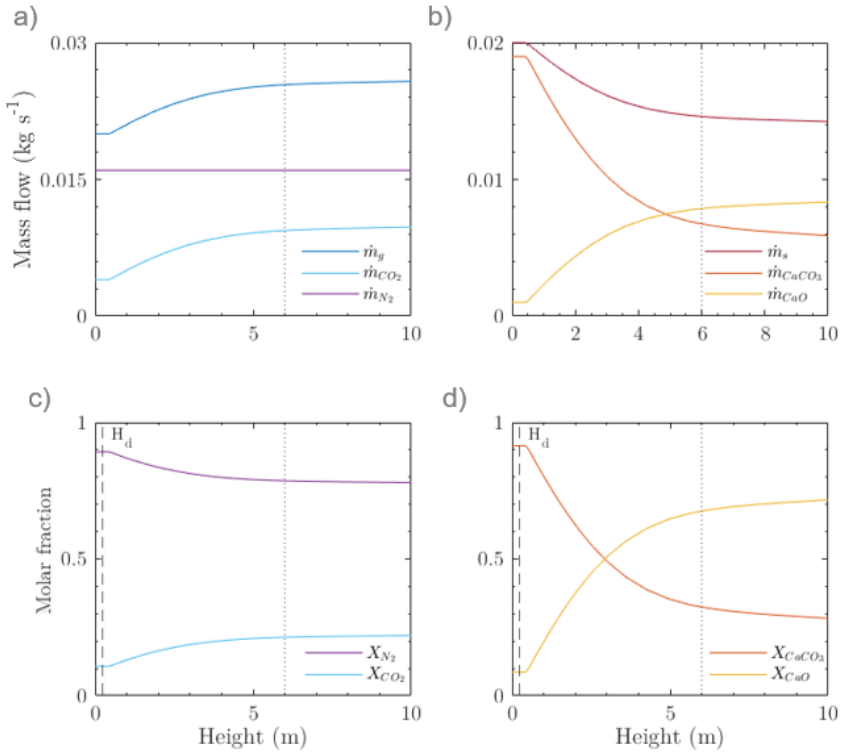

Figure 32. Distribution along the axial direction of the calciner of a) mass flow rates of gas and b) solid phases species, and the molar fractions of the c) gas and d) solid-phase species. For these results, a constant temperature wall of 900 °C is assumed.

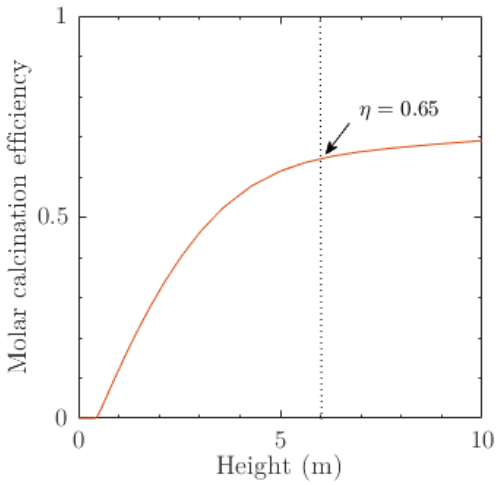

Figure 33. Molar calcination efficiency. A final efficiency of 0.69 is achieved at the end of the reactor height. For this result, a constant temperature wall of 900 °C is assumed.

4.1.4. Sensitivity study

Calculating the efficiency of the process depends on various parameters. To investigate their role in the calcination process, a sensitivity analysis was performed. These parameters are divided into two categories including the model parameters and inlet conditions. Table 12 shows the reference values and variation range for each of them. The justification of the proposed ranges has been discussed in more detail in section 4.1.1.

Table 12. Variation interval of the parameters studied in the sensitivity study for a constant temperature wall.

Parameter	Reference value	Variation interval	Justification
a [m^{-1}]	$\frac{6}{U_0(H_d)}$	$\left[\frac{4}{U_0\ H_d}\ ;\ \frac{12}{U_0(H_d)}\right]$	Based on experimental results presented in Kunii and Levenspiel [44]
H_d [m]	0.25	[0 ; 1]	Based on experimental result [39], [37], [71], [72]
d_p [μm]	300	[200 ; 400]	Diameter range of the samples used for density measurement of $CaCO_3$ and CaO
m_g 0 [$kg\ s^{-1}$]	0.2	[0.005 ; 0.025]	Based on the design conditions of calciners at lab-scale [41], [48], [68]
m_s 0 [$kg\ s^{-1}$]	0.2	[0.005 ; 0.025]	
T_b 0 [$°C$]	650	[25 ; 650]	Based on the temperature range that could be achieved when storing the products obtained in the carbonator
x_{CO_2} 0 [–]	0.2	[0 ;0.4]	Based on experimental conditions tested for calcination [70]
x_{CaO} 0 [–]	0.05	[0 ;0.35]	Based on the range of unreacted CaO after the carbonation step [69], [77]

For the sensitivity study, three variables were selected to represent the three main processes under study, i.e. reaction kinetics, hydrodynamics, and heat transfer. These variables are the molar calcination efficiency, the solids residence time, and the temperature of the bed. Figure 34 shows the sensitivity

study results for the hydrodynamic parameters, i.e. the decay factor, the dense bed height, and the particle diameter.

The decay factor was varied from 0.65 to 1.3. From the results, the molar calcination efficiency increases as the decay factor decrease. The lower the decay factor is the longer the residence time of the particles is, hence the increased efficiency. The efficiency improves 47 % points when comparing results using the limit values of the variation interval. The decay factor affects greatly the velocity of solids in a significant height of the reactor (Figure 35). Therefore, it is necessary to confirm experimentally this parameter in a set up with high temperatures and variable mass flow rates. Lastly, the temperature of the bed is also affected to a lower extent in the lean zone. Figure 36 shows that the temperature also contributes to obtaining a broad range of values for the calcination rate.

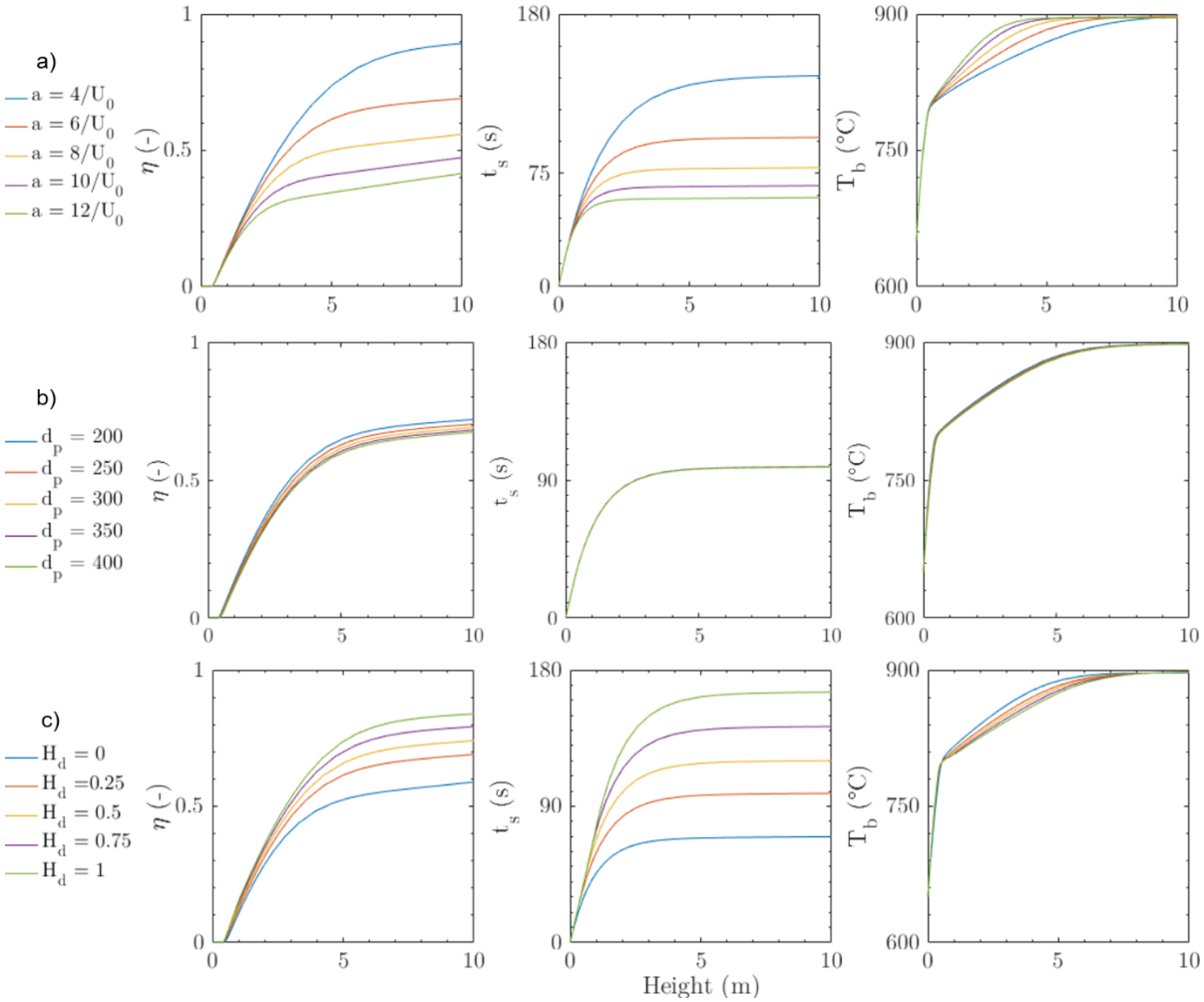

Figure 34. Sensitivity study for a) decay factor, b) dense bed height, and c) particle diameter. From left o right, the molar calcination efficiency, the residence time of solids, and the temperature of the bed are presented.

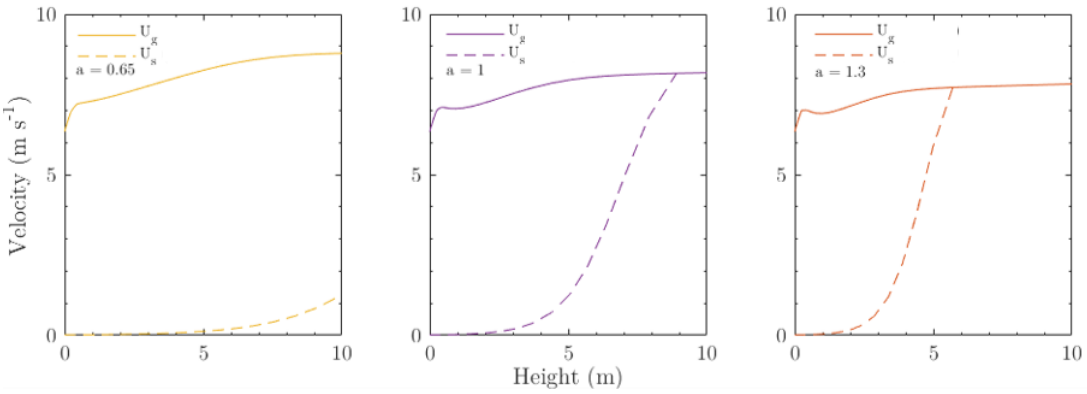

Figure 35. Variation of the gas and solids velocity for the sensitivity study of the decay factor. The variation interval is from 0.65 to 1.3 based on the correlations from Kunii and Levenspiel [44].

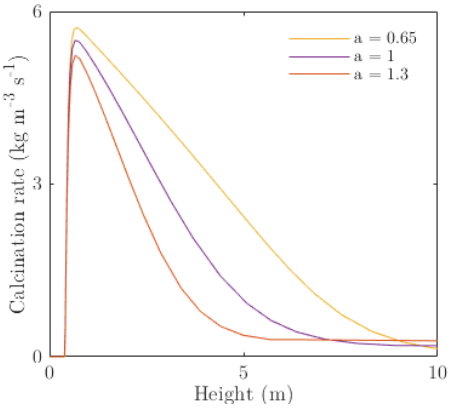

Figure 36. Variation of the calcination rate for the sensitivity study of the decay factor. The variation interval is from 0.65 to 1.3 based on the correlations from Kunii and Levenspiel [44].

The height of the dense bed was varied from 0 to 1 m. Within this range, the efficiency improved 25 % points. The increase of this parameter mainly displaces up the profiles of the solids volumetric fractions and the solids velocities leading to an increase of the residence time and the molar calcination efficiency for higher values of H_d. The effect of this parameter on the temperature of the bed is not that significant in the studied interval. The final parameter to be evaluated from this category is the particle diameter. This parameter is used for the computation of heat transfer coefficients only. Results show that its effect is negligible on the temperature profile and the molar calcination efficiency.

The second category of parameters to be evaluated is related to the inlet conditions of the reactor. The effect of varying each parameter is shown in Figure 37 and Figure 38. The temperature of the bed at the inlet showed to have major effects on the molar calcination efficiency achieved (Figure 37.a). For low temperatures, the efficiency was the lowest of all the tests. The calcination reaction starts around 1.4 m. In this interval, the bed is heated up to 800 °C (Figure 39). After 800 °C the concentration of CO_2 in equilibrium surpasses the value of the local CO_2 concentration that is the driving force to start the reaction. The results show that there is no significant change when the temperature at the inlet is increased from ambient temperature to 170 °C. After this interval, as the inlet temperature rises the process efficiency improves. An inlet temperature of 650 °C was selected as the favorable limit as this

is the temperature the bed would have if it would have come directly from the carbonator. The improved efficiency is 27 % points. These results suggest the need of using a preheater for the gas and solids before being feed into the calciner and the use of a well-insulated storage system to decrease losses from daytime to night-time.

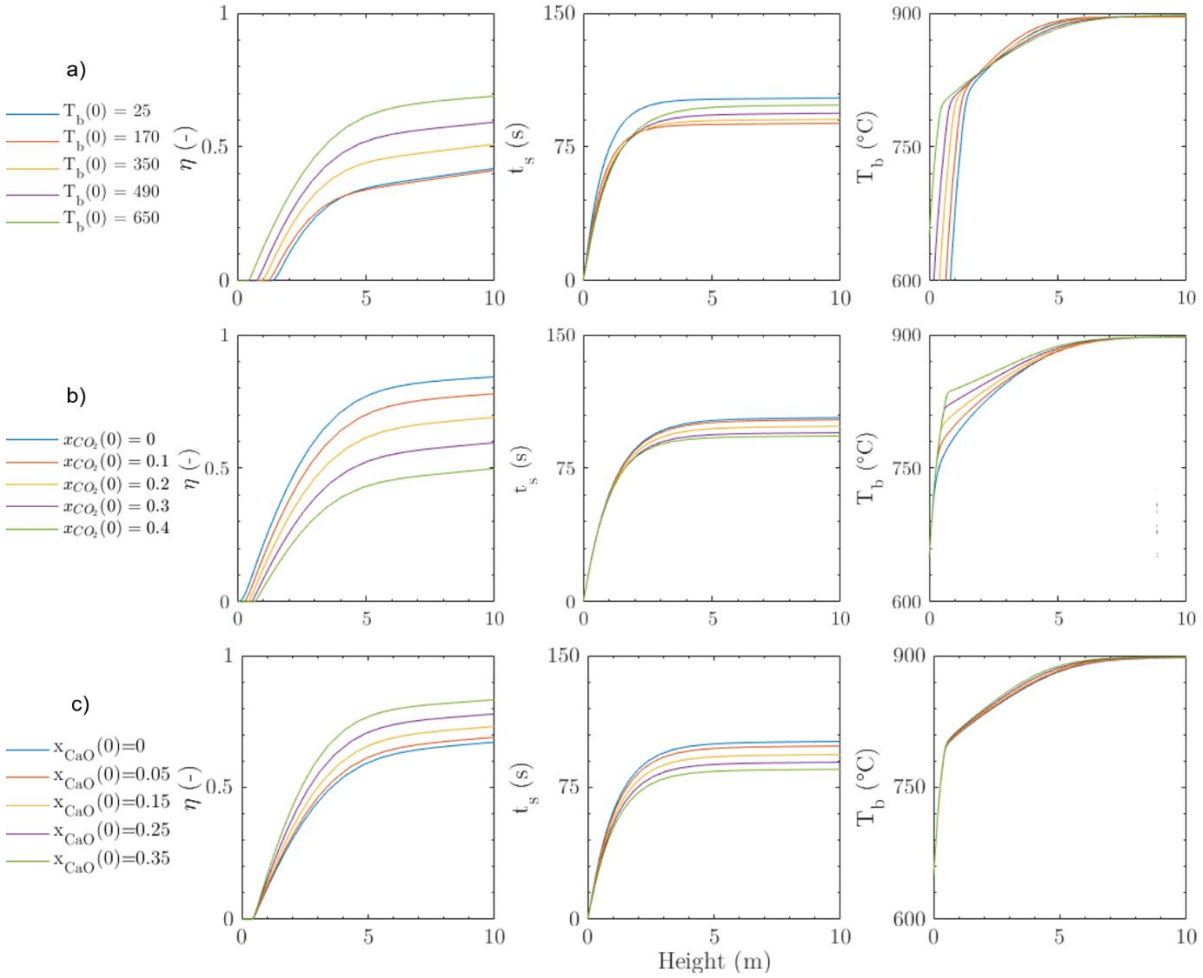

Figure 37. Sensitivity study for the following inlet conditions: a) bed temperature, and the mass fraction of b) CO_2 and c) CaO. From left to right, the molar calcination efficiency, the residence time of solids, and the temperature of the bed are presented.

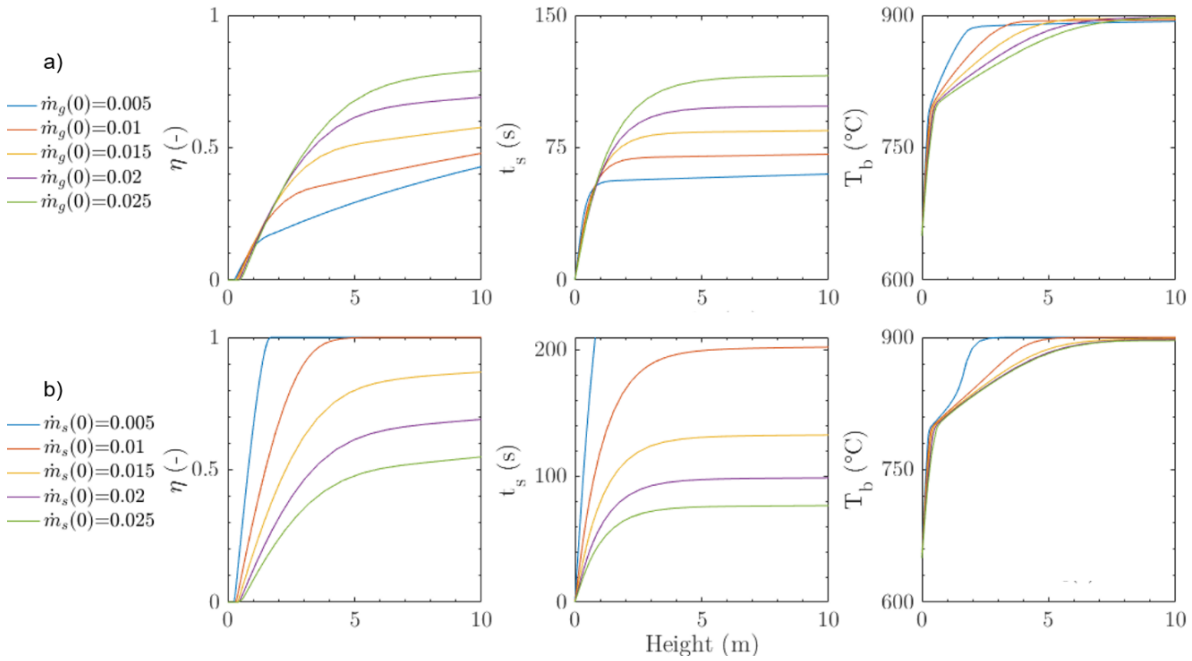

Figure 38. Sensitivity study for the following inlet conditions: a) gas mass flow rate and b) solids flow rate at the inlet. From left to right, the molar calcination efficiency, the residence time of solids, and the temperature of the bed are presented.

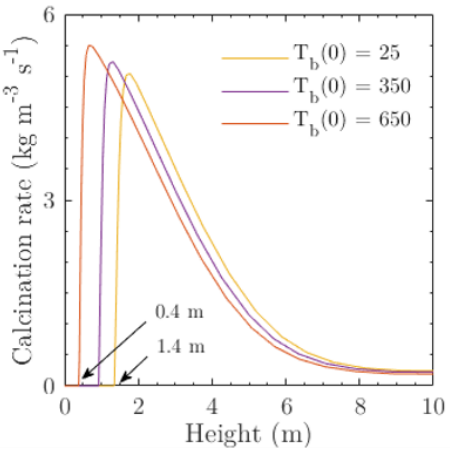

Figure 39. Variation of the calcination rate for the sensitivity study of the inlet temperature of the bed. The variation interval is from ambient temperature to 650 °C.

The change of the initial mass fraction of CO_2 affects the reaction rate and the temperature profile in the lean zone (Figure 37.b). For the lowest limit, i.e. 0 % of CO_2, the reaction starts at the very beginning of the reactor. For the highest limit, the reaction starts around 0.7 m (Figure 40) after the gas reaches 840 °C. At higher inlet CO_2 mass fractions, the initial local concentration of CO_2 is too high when compared to the one in equilibrium, therefore, the gas must be heated to a higher temperature for the reaction to start. The CO_2 mass fraction at the inlet is an important factor to be considered when designing the reactor for given conditions. These conditions should be established considering the carbonator.

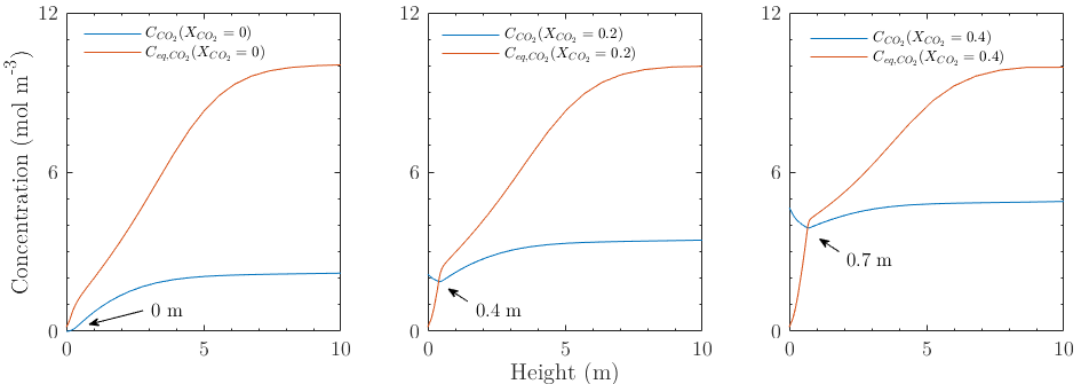

Figure 40. Variation of the local concentration of CO_2 and its equilibrium concentration for the sensitivity study of the initial mass fraction of CO_2 in the fluidizing gas. The variation interval is from 0 % to 40 %.

The final parameter evaluated in Figure 37 was the inlet mass fraction of CaO. The amount of unreacted CaO in the carbonator varies from sorbent to sorbent and a wide range of deactivation can be found in the literature. When the inlet mass fraction of CaO is varied from 0 to 0.15, the results show no significant change in the calcination efficiency. However, this range would be valid in the case of using high-quality sorbents or by decomposing dolomite which deactivation reaches up to 5 - 8 % [78]. When varying the CaO mass fraction up to 0.4, the results are more significant and a variation on the calcination efficiency of 16 % point is obtained when comparing the limiting cases. In the particular case of $X_{CaO}(0)$, the efficiencies obtained could be misleading when assessing the effect of the parameter. The molar calcination efficiency is defined as the ratio of the calcined sorbent to the inlet molar fraction of $CaCO_3$. The higher the content of CaO due to deactivation, the lower the content of $CaCO_3$ entering the calciner and the fewer sorbent available for calcination. This results in an improvement of the efficiency but only because less material is available to be calcined. Therefore, it could be beneficial to select enhanced sorbents to minimize their deactivation. CaO precursors as dolomite look to be promising for their low deactivation after several cycles.

Figure 38 shows the effect of varying mass flow rates at the inlet of the reactor. The gas mass flow rate affects the residence time of the gas and solid phases, and the particle distribution in the reactor. Therefore, there is an effect on the molar calcination efficiency. The improved efficiency is 36 % points and is achieved when the gas mass flow rate is increased up to 0.025 kg s^{-1}. The case of $m_g\ 0\ = 0.005$ shows a different pattern from the rest. This is a result of the ratio of gas and solids mass flow rate, which in this case is $\frac{m_g}{m_s} = \frac{0.005}{0.02} = 0.25$. At this condition, the achieved gas velocity is around 1.5 m s^{-1} which corresponds to conventional fluidized bed reactors where no entrainment is achieved. Therefore, this model is not valid to simulate this inlet condition but gives a hint about the fraction m_g/m_s needed for achieving fast fluidization. For higher gas mass flow rates at the inlet than this case, the residence time profiles are consistently flat after 5 - 6 m height, which supports the selection of a reactor height in this range for the operating conditions analyzed in this study. Similarly, when varying the solid mass flow rate at the inlet, a great effect on the achieved molar efficiency is seen (Figure 38.b). In the case of m_s equal to 0.005 and 0.01 kg s^{-1} complete calcination is achieved in the first half of the reactor. To have an idea, for a solids mass flow rate of 0.01 the fraction of $m_g(0)/m_s(0)$ is 2. To have more insights

about the effect of the fraction of mass flow rates, Figure 41 shows the effect on the calcination efficiency measured at the end of the reactor when changing the mass flow rate of solids at the inlet under different $m_g(0)/m_s(0)$ ratios. Even though the efficiency is measured at 10 m height, all the cases that achieve complete calcination in Figure 41 do it at shorter heights, i.e. 2 - 6 m depending on the ratio and mass flow rate selected. It can be concluded from this result that a ratio of at least 1.5 would be necessary to achieve complete calcination in a fast fluidization regime. In the reference cases of this study, a ratio of 1 was being used. To increase the efficiency conserving the same ratio, it would be needed to decrease the mass flow rate of the gas and solid. Caution should be paid to the achieved gas velocity. For example, for low velocities, the limit between conventional fluidization and low-density CFB is around 1.8 m s^{-1}. Therefore, one should verify that the selected ratio allows achieving velocities that correspond to the low-density CFB regime. The regime diagram from Sun and Zhu [33] could be used to verify this. The profiles of Figure 38 are delimited by gas velocities of 1.8 - 7 m s^{-1}. In other words, the plotted cases respect that the gas velocity achieved falls in this range. The profiles tend to move to the right with a decrease of the ratio $m_g(0)/m_s(0)$ achieving lower molar calcination efficiencies.

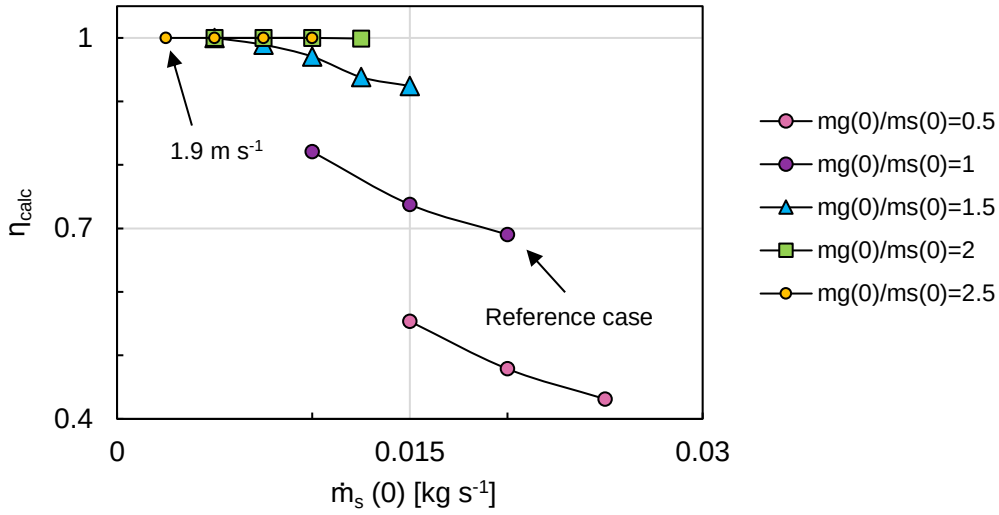

Figure 41. Effect of the molar calcination efficiency at the end of the reactor as a function of the mass flow rate of solids at the inlet when varying the ration of $m_g(0)/m_s(0)$. All the cases that achieve complete calcination do it at shorter heights, i.e. 2-6 m.

To summarize the discussion of the results from the sensitivity study, Table 13 was built. It must be remarked that these parameters were not varied by a given percentage as in regular sensitivity studies but the limits were chosen based on experience and experimental data from the literature. The parameters that lead to a difference in improved efficiency greater than 25 % are highlighted in orange. To provide context to the reader, the most favorable limits are highlighted in green. Based on these results the parameters that affect the most the efficiency of the process are the decay factor, the initial temperature of the bed, the inlet mass flow rates, and the initial concentration of CO_2. As explained before, it is necessary to validate the decay factor for reactors with reactive systems and high temperatures. This could be done by measuring the pressure drop along with the height of the reactor which will allow obtaining the solids volumetric fractions profile, therefore, allowing the validation of the

hydrodynamics under these conditions. The results related to the initial temperature of the bed have proved that the preheating of the sorbent and fluidizing gas will be important to achieve high calcination efficiencies. The upper limit for preheating is around 650 °C at ambient pressures. An optimum ratio of the gas and solid mass flow rate should be used to obtain higher calcination efficiencies. The results suggest that the m_g/m_s ratio is around 1.5-2. Ultimately, it is necessary to decide on the height of the reactor based on the CO_2 inlet mass fraction to be used. The results show that for high CO_2 mass fractions at the inlet, a significant height of the reactor is used for increasing the temperature until a favorable CO_2 equilibrium concentration is reached. Finally, from the results of this section, it is concluded that a shorter reactor can be built for the given operating conditions. A height of 5 to 6 meters is recommended.

Table 13. Molar calcination efficiencies obtained in the sensitivity study. The most favorable limit is highlighted in green and those efficiency differences with greater values than 25 % are highlighted in orange.

			Efficiency difference $\Delta\boldsymbol{\eta} = \lvert\boldsymbol{\eta}_{lowest} - \boldsymbol{\eta}_{highest}\rvert$	
Parameter	**Lowest boundary**	**Highest boundary**	**At 6 m (% points)**	**At 10 m (% points)**
$a\ [\mathrm{m}^{-1}]$	$\frac{4}{U_0\ H_d}$	$\frac{12}{U_0(H_d)}$	44	47
$H_d\ [m]$	0	1	23	25
$d_p\ [\mu m]$	200	400	3	3
$m_g\ 0\ \ [kg\ s^{-1}]$	0.015	0.025	38	36
$m_s\ 0\ \ [kg\ s^{-1}]$	0.015	0.025	49	46
$T_b\ 0\ [°C]$	25	650	27	27
$x_{CO_2}\ 0\ \ [-]$	0	0.4	34	34
$x_{CaO}\ 0\ \ [-]$	0	0.35[1]	16	16

[1] The highest calcination efficiency is found when the inlet mass fraction of CaO is the highest. However, the improved efficiency is a result of less $CaCO_3$ available for calcination.

4.2. Model Implementation with Non-uniform Heat Flux

Assuming a constant temperature at the wall is not realistic but it is an ideal scenario to study the physics behind the process. In this section, the next step to transition to the coupling of the reactor to a CSP system is given by imposing a non-uniform heat flux on the wall of the absorber tube.

4.2.1. Input parameters and considerations

The input parameters for the implementation of the model for this case are the same as the ones presented in section 4.1.1 for the reference case, with the difference of imposing a non-uniform flux on the wall instead of a constant wall temperature. The selected flux is inputted as the heat power from the wall to the bed $H_{transf}(z)$ in equation (3.55). Like this, the ODE solver computes the temperature of

the bed with the original structure of the code. However, a modification is added for computing the temperature of the wall. A function with an iterative procedure was created with the heat transfer coefficient equations. These equations depend on the temperature of the bed, which is given as input, and the temperature of the wall, which is to be found. Therefore, the temperature profile of the wall is computed at each step by using an initial guess and iterating until the computed heat power from the wall to the bed $H_{transf,comp}(z)$ converges to the input value $H_{transf}(z)$.

4.2.2. Selection of the imposed non-uniform heat flux

The concentration distributions on the receiver tube will strongly depend on the aiming point and control strategy of the solar field. In other words, a different flux distribution would result from a single aiming point strategy than from a multiple aiming point strategy. As an example, Figure 42 presents the concentration distributions obtained with different aiming strategies for a non-dimensional receiver length. For a single aim-point strategy, one encounters a high-density flux peak. In Figure 42.a it can be noted that an increase of the receiver radius results in a reduction of the solar flux concentration, an enlarged tail in the distribution, and a shift of the peaks towards lower receiver locations. To flatten the flux distribution is necessary to use multiple aim-point strategies, where the mirrors aim different focal points along the centerline of the receiver. In Figure 42.b it is shown that when a group of mirrors is aimed at a new focal point, its flux contribution maintains its original shape but is displaced vertically. Therefore, Figure 42 shows that the shape of the solar flux density distribution can be reshaped to meet certain requirements.

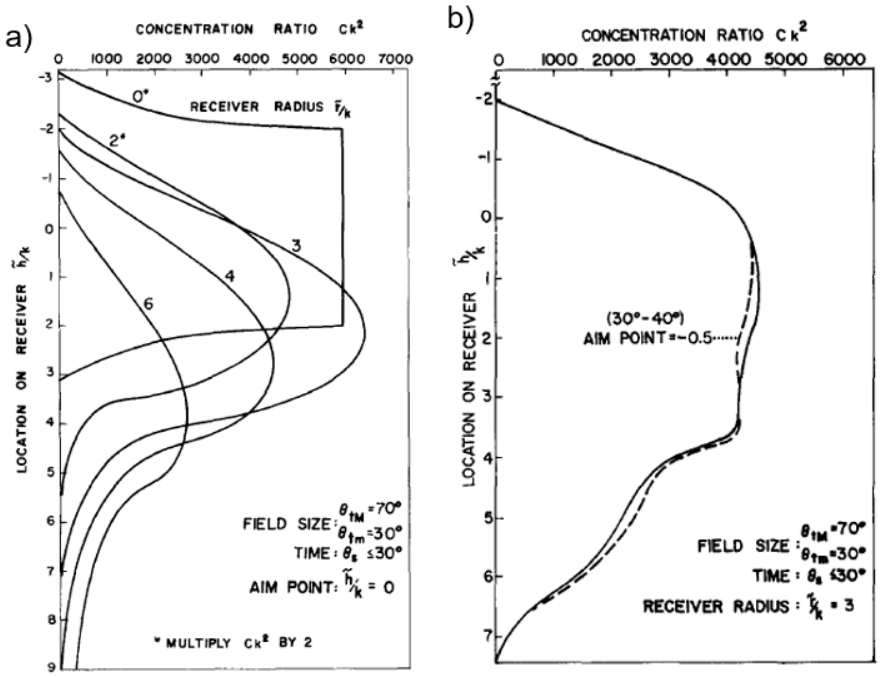

Figure 42. Concentration ratio distribution for a) single aim-point strategy and b) Multiple aim-point strategies. The receiver length is normalized to a base length equal to the perfect Sun disc radius at a distance equivalent to the tower height. k stands for dispersion factor and it variates from 2 to 4 being 1 representing ideal condition [79].

For this study case, a non-uniform flux in the vertical plane of the tube would be assumed as a starting point. Figure 43 shows the incident flux distribution to be imposed in the model. A flux distribution similar to Figure 42.b was created by using the summation of two Gaussian distributions:

$$f(z;\ \sigma, c) = e^{-\frac{(z-c)^2}{2\,\sigma^2}} \tag{4.2}$$

where σ and c are the standard deviation and the mean respectively. The gaussian parameters were variated while checking that the temperature of the wall does not exceed the 900 °C to avoid sintering of the sorbent. It can be noted that the flux distribution is not zero at the inlet of the absorber tube. The reason for this is that from the simulations it is known that a significant height of the reactor would be needed to heat the bed to a point where the equilibrium concentration of CO_2, which depends on temperature, surpasses the local concentration of CO_2. Only when the previous is accomplished, the reactions proceed. Therefore, if a centered distribution would be used, the required height of the tube would significantly increase. Nevertheless, a non-zero flux at the bottom of the receiver could have some construction implications that could be handled for example with a secondary reflector.

The distribution in Figure 43 is built to be able to compare results with the previous case presented in section 4.1. This distribution is just an example of a non-uniform flux with a zone with higher intensity. It must be reminded that the exact distribution on the absorber tube will depend on the control strategy of the solar field and require further work.

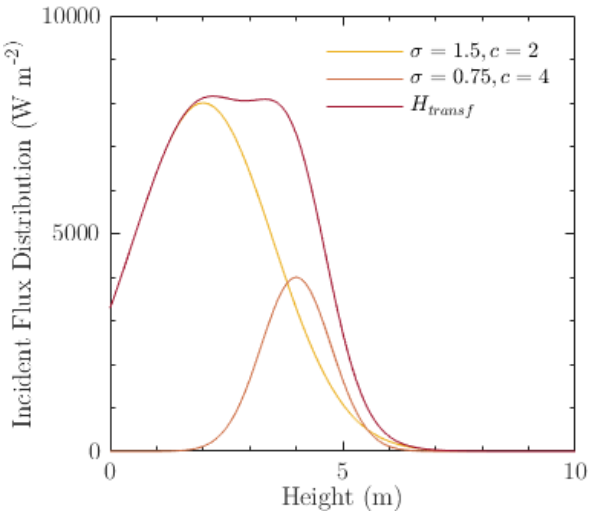

Figure 43. Irradiance distribution to be imposed as the heat power from the wall to the bed. The distribution in red is the sum of the distributions in yellow and in orange.

4.2.3. Test with reaction and heat transfer for non-uniform heat flux

The simulation results from implementing the proposed model by imposing a non-uniform heat flux are presented in this section. Figure 44 (a-c) shows the results related to heat transfer from the tube to the reactor. The total heat transfer coefficient varies from 200 - 400 W m^{-2} K^{-1}. These values are in the range of the reported values found in the literature. Nevertheless, the range is much wider than in the case of

the constant wall temperature. Figure 44.a shows the calcination heat flux. The reaction starts at 1.3 m which can be also verified in Figure 45, Figure 46, and Figure 47. As in the case with constant wall temperature, this height corresponds to the point where the CO_2 equilibrium concentration surpasses the local CO_2 concentration. After several tests varying the distribution of the heat flux used, the value of the efficiency fluctuated from 0.5 to 0.69. However, the temperature of the bed always reached 900°C around 5 m height as shown in Figure 44.b. This temperature marks the limit where sintering of the sorbent occurs, therefore, it should be avoided. Future work is necessary to optimize the solar field by using an aiming strategy that allows to homogenize the flux distribution spatially and to avoid the bed temperature to reach sintering temperatures.

The achieved conversion is similar to the one shown for the case of constant wall temperature. Figure 46 shows that the molar fraction and mass flow rates profile flattens after 6 m height. Similar behavior is shown in Figure 47 where it can be seen that the molar calcination efficiency at 6 m and 10 m height is 0.66 and 0.7, therefore, not showing greater improvement by increasing the reactor height. However, this is a result of the imposed flux distribution which approaches zero around that height. After this, the calcination proceeds without flux at the expense of the internal energy of the bed. Improvements on using a more representative solar flux might variate the needed height, and as described above this assessment is the subject of future work.

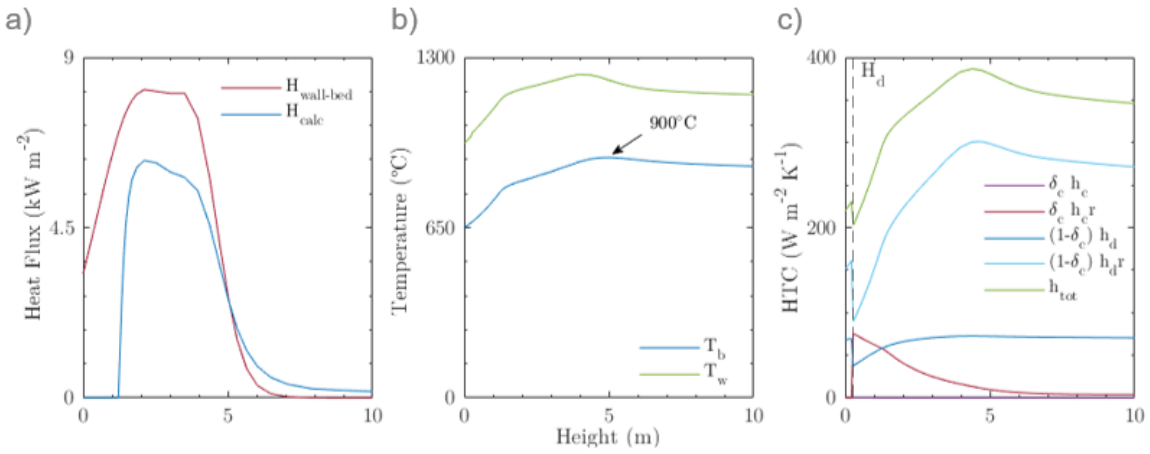

Figure 44. Distribution along the axial direction of the calciner of a) wall-to-bed heat flux, b) temperature profiles of the bed and wall, c) heat transfer coefficients. The height of the dense bed (H_d) is shown with a vertical line. These results correspond to the case where a heat flux corresponding with the irradiance of a solar field over the absorber tube is used as input in the model.

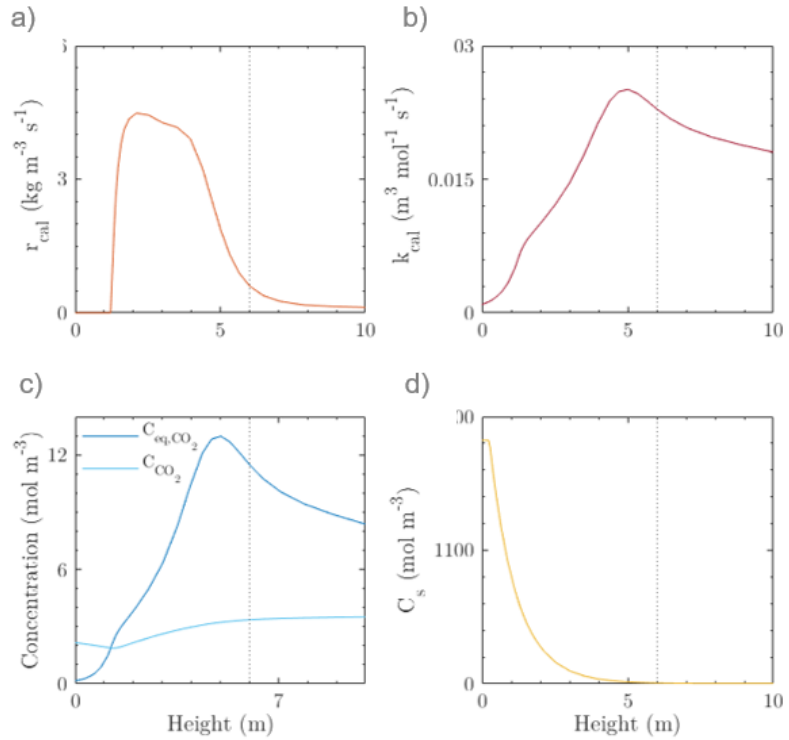

Figure 45. Distribution along the axial direction of the calciner of a) reaction rate, b) kinetic constant of the calcination reaction, c) CO_2 concentration in equilibrium and in the reactor, and d) concentration of solids. These results correspond to the case where a heat flux corresponding with the irradiance of a solar field over the absorber tube is used as input in the model.

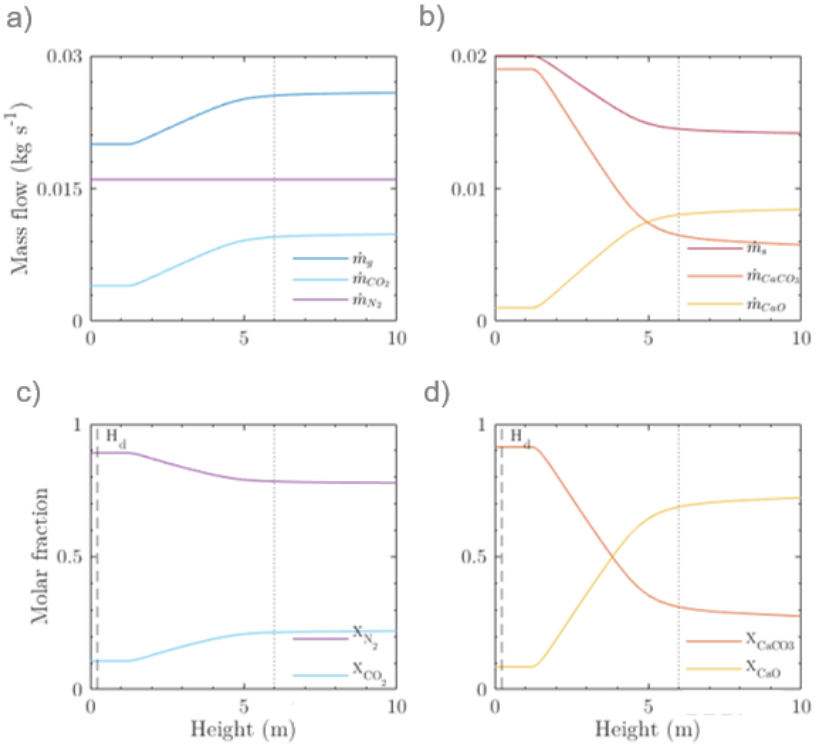

Figure 46. Distribution along the axial direction of the calciner of a) mass flow rates of gas and b) solid phases species, and the molar fractions of the c) gas and d) solid-phase species. These results correspond to the case where a heat flux corresponding with the irradiance of a solar field over the absorber tube is used as input in the model.

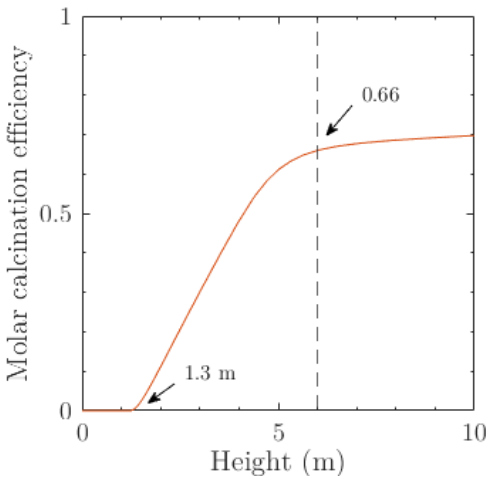

Figure 47. Molar calcination efficiency. A final efficiency of 0.7 is achieved at the end of the reactor height. The reaction starts at 1.3 m. These results correspond to the case where a heat flux corresponding with the irradiance of a solar field over the absorber tube is used as input in the model.

4.2.4. Sensitivity study

A sensitivity study for the case of non-uniform heat flux on the wall was done to evaluate the effect of the most significant parameters evaluated in the case of constant wall temperature. These parameters and their variation interval are described and highlighted in orange in Table 12. The decay factor, the gas and solids mas flow rates, the inlet bed temperature, and the inlet mass fraction of CO_2 are the parameters to be studied in this section.

The decay factor effect on the molar calcination efficiency resulted to be less significant than in the constant wall temperature case (Figure 48.a). For a non-uniform flux distribution, only a difference of 9 % points is achieved when compared to the 47 % points obtained in the constant wall temperature one. This difference is due to the flux distribution used that results in a variable bed temperature which decreases after reaching 5 m heigh. This height corresponds to the one after which the heat flux decreases dramatically, a small increase in the calcination efficiency is achieved only at the expense of the internal energy of the bed. The fact that no significant heat flux is available after 5 m is one of the reasons why the obtained profiles in the sensitivity study do not vary in the same proportion as in the case of the constant wall temperature case where the temperature of the bed reaches equilibrium in the second half of the reactor.

For the inlet mass flow rate of gas, the case of $m_g\ 0\ = 0.005$ also achieves gas velocities around 1.5 m s^{-1} which corresponds to the conventional regime of fluidization and marks the limit between this regime and fast fluidization (Figure 48.b). This model is not able to model these conditions. For the inlet mass flow rate of gas, the effect in the calcination efficiency is only 4 % points. Oppositely, for the mass flow rate of solids the effect is significant, i.e. 47 % points which is almost the same results achieved in the case of constant wall temperature (compare Figure 48.b with Figure 38.b). Even though the efficiencies achieved are similar to the previous case, the temperature profile of the bed differs as expected from applying a non-uniform flux distribution at the wall.

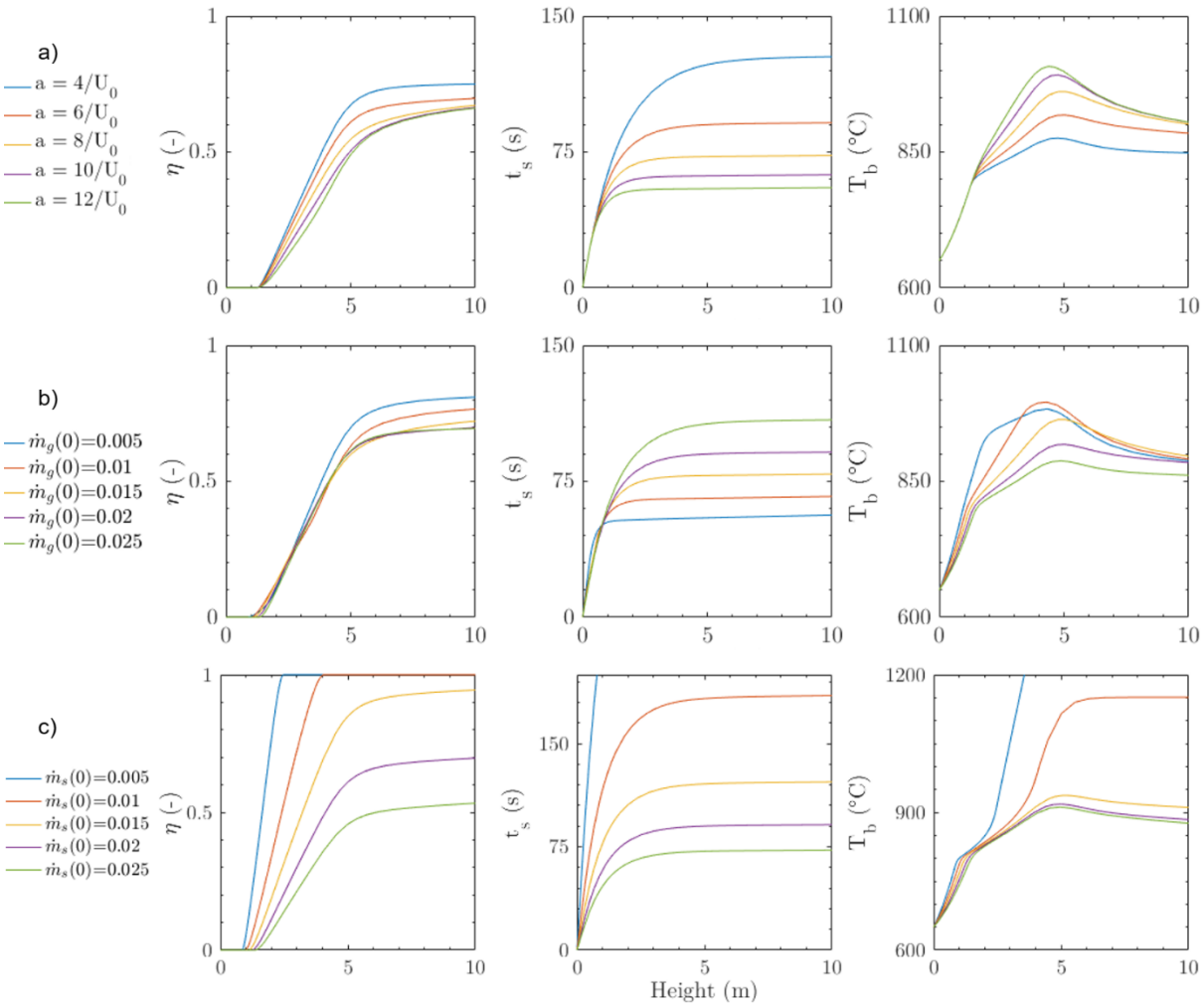

Figure 48. Sensitivity study for the following parameters: a) decay factor, b) gas mass flow rate, and b) solids flow rate at the inlet. From left to right, the molar calcination efficiency, the residence time of solids, and the temperature of the bed are presented.

Figure 49 shows the effect on the calcination efficiency measured at the end of the reactor when changing the mass flow rate of solids at the inlet under different $m_g(0)/m_s(0)$ ratios. Similarly to the case of constant wall temperature, the plotted ratios were verified so they do not fall in the conventional fluidization regime without entrainment. Also, all the cases that achieve complete calcination in Figure 41 do it at shorter heights, i.e. 2 - 6.7 m depending on the ratio and mass flow rate selected (Table 14). The results of the analysis of the ratio $m_g(0)/m_s\ 0$ when imposing a non-uniform flux distribution differ from the ones presented in the previous case (compare Figure 49 with Figure 41) because the temperature bed profile is different as a result of the flux distribution selected which raises the temperature of the bed above 900 °C and then decreases. This distribution was selected taking into account that the reference case conditions at the inlet were $m_g\ 0\ = 0.02$ and $m_s\ 0\ = 0.02$ for which a maximum bed temperature of 900 °C is achieved. When the ratio or the mass flow rates are changed in the analysis, the temperature of the bed and the wall rises as the mass flow rate of solids is lower. The temperature surpasses the limits imposed by sintering and the temperature that the wall material can stand (Table 14). Even though complete calcination is achieved, is necessary that the ratio and mass

flow rates is selected not only taking into account the velocity of the gas (to be in the low-density CFB regime) but more important the limiting temperatures.

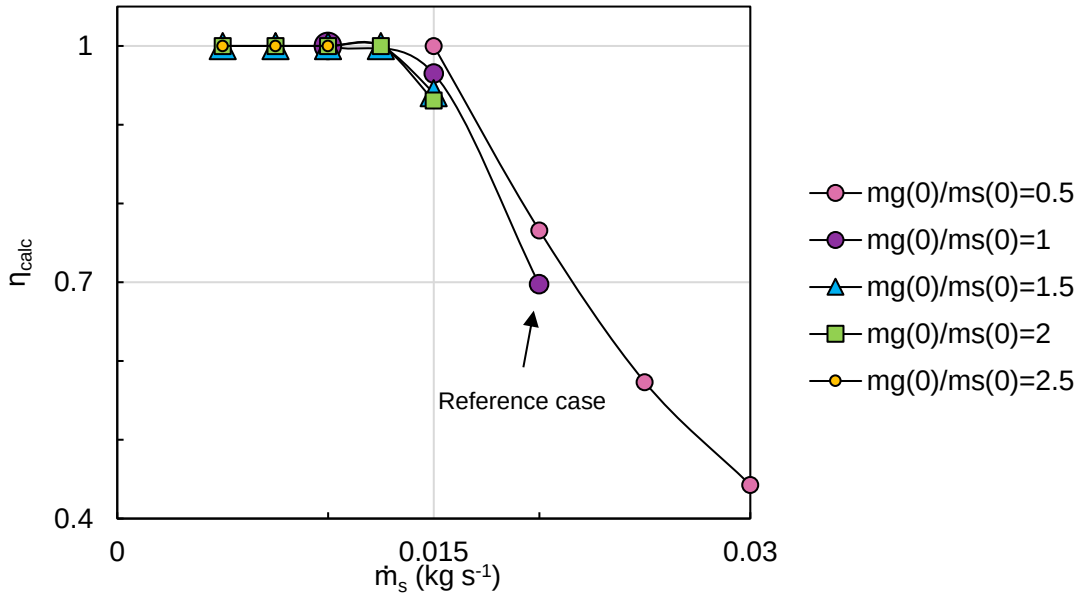

Figure 49. Effect of the molar calcination efficiency at the end of the reactor as a function of the mass flow rate of solids at the inlet when varying the ration of $m_g(0)/m_s(0)$. All the cases that achieve complete calcination do it at shorter heights, i.e. 2-6 m.

Table 14. Molar calcination efficiency $\boldsymbol{\eta_{calc}}$, height where complete calcination is achieved $\boldsymbol{z_{calc}}$, maximum bed temperature achieved $\boldsymbol{T_{b_{max}}}$ as a function of the mass flow rate of solids at the inlet when varying the ration of $\dot{m}_g(0)/\dot{m}_s(0)$.

	$\dot{m}_s$	$\boldsymbol{\eta_{calc}}$	$\boldsymbol{z_{calc}}$	$\boldsymbol{T_{b_{max}}}$
$\frac{\boldsymbol{mg(0)}}{\boldsymbol{ms(0)}} = \boldsymbol{1}$	0.01	1.0	2.7	1393.2
	0.015	1.0	4.0	985.8
	0.02	0.7	5.4	1018.8
$\frac{\boldsymbol{mg(0)}}{\boldsymbol{ms(0)}} = \boldsymbol{1.5}$	0.005	1.0	2.0	2321.1
	0.01	1.0	4.0	1248.6
	0.015	0.9	6.1	918.1
$\frac{\boldsymbol{mg(0)}}{\boldsymbol{ms(0)}} = \boldsymbol{2}$	0.005	1.0	3.0	1620.1
	0.01	1.0	5.4	1150.7
	0.015	1.0	6.7	958.4

The temperature of the bed results stresses the importance of preheating the gas-solid flow (Figure 50.a). For the flux distribution used, it was not possible to calcine the $CaCO_3$ sorbent with an initial temperature of the bed at ambient temperatures. The flux distribution used for the analysis is not enough to provide the power needed to heat the bed until a suitable temperature after which calcination can proceed. The effect of the temperature of the bed variated by 68 % points the molar calcination efficiency, being the highest efficiency achieved of 0.48 at 650 °C. In this case, this result is much more significant than in the case of the constant wall temperature where the difference achieved was 27 %.

Finally, the variation of the mass fraction of CO_2 results in an insignificant change in the profiles of efficiency effect, but it shows that for higher CO_2 inlet concentrations a higher height is needed for the calcination reaction to proceed (Figure 50.b). This would be aggravated if the aiming strategy would be different and the flux distribution would be centered in the middle of the reactor height, therefore, it is necessary to optimize the aiming strategy accordingly to reduce the needed height for the reactor.

Table 15 summarizes the differences in the molar calcination efficiency obtained in this sensitivity study. The parameters that lead to a difference in improved efficiency greater than 25 % are highlighted in orange. The significance of the change of the majority of the parameters was not of the same magnitude as for the case of the constant wall temperature. The reason for this is that the peak of the flux is constrained to the first half of the reactor. From the constant wall temperature case, it is known that the variation of the results is more significant in the second half of the reactor where the temperature of the bed approaches the temperature of the wall for a significant reactor length. Therefore, it was expected that in this sensitivity analysis the changes would be not as abrupt as in the previous case for the second half of the reactor.

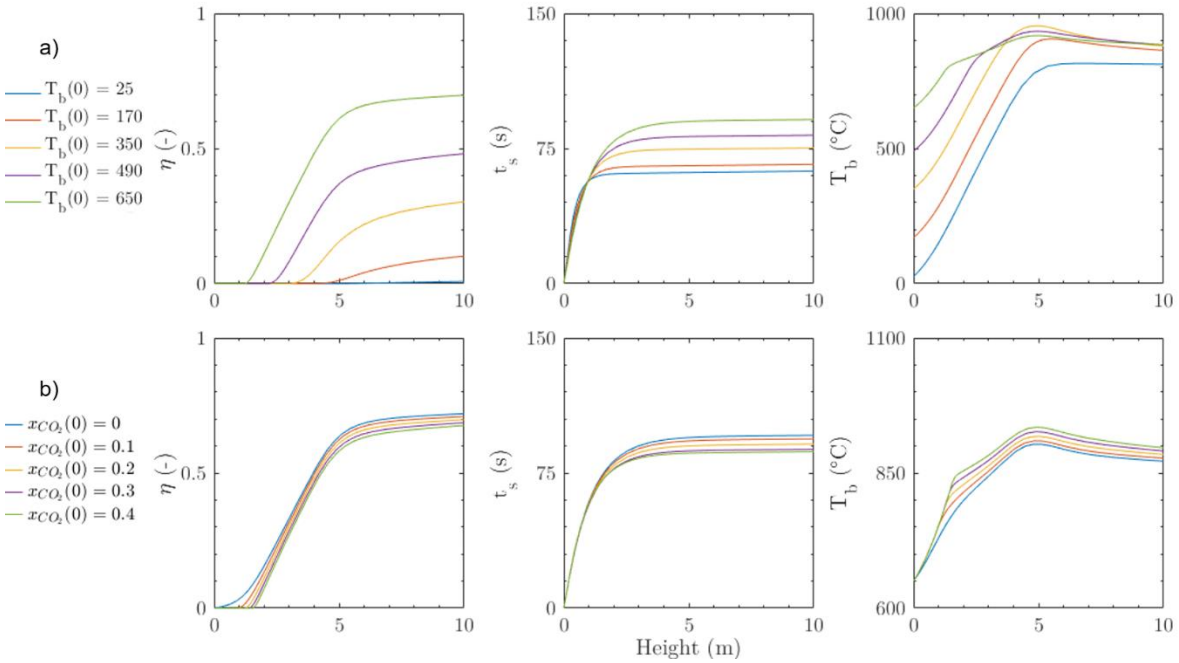

Figure 50. Sensitivity study for the following inlet conditions: a) the temperature of the bed at the inlet and b) the mass fraction of CO_2 at the inlet. From left to right, the molar calcination efficiency, the residence time of solids, and the temperature of the bed are presented.

Table 15. Molar calcination efficiencies obtained in the sensitivity study for the non-uniform flux at the reactor wall. The most favorable limit is highlighted in green and those efficiency differences with greater values than 25 % are highlighted in orange.

			Efficiency difference $\Delta\eta = \lvert\eta_{lowest} - \eta_{highest}\rvert$	
Parameter	**Lowest boundary**	**Highest boundary**	**At 6 m (% points)**	**At 10 m (% points)**
$a\ [\mathrm{m}^{-1}]$	$\frac{4}{U_0\ H_d}$	$\frac{12}{U_0(H_d)}$	13	8
$m_g\ 0\ \ [kg\ s^{-1}]$	0.015	0.025	5	4
$m_s\ \ 0\ \ [kg\ s^{-1}]$	0.015	0.025	42	47
$T_b\ 0\ [°C]$	25	650	65	68
$x_{CO_2}\ 0\ \ [-]$	0	0.4	5	3

[1] The highest calcination efficiency is found when the inlet mass fraction of CaO is the highest. However, the improved efficiency is a result of less $CaCO_3$ available for calcination.

Chapter 5

Conclusions

The main goal of this study was to develop a simplified model for the thermal decomposition of $CaCO_3$ in a solar reactor for Thermochemical Energy Storage (TCES) in Concentrating Solar Power (CSP) systems. From the exhaustive review of the state of the art of solar reactors, it was concluded that CFB was the preferred option. Their high heat and mass transfer rate, good mixing of solids, adjustable residence time, and the possibility of continuous operation, where the main factors to select this reactor. Additionally, the use of the riser of the CFB as the absorber tube allows to indirectly heat the reaction chamber while enclosing the tube in a window-less reflective cavity to reduce losses. Using the tube as an intermediate radiating surface is beneficial for smoothing the temperature differences of the bed, and reducing the risk of over and under heating the reactant as it passes through different parts of the reactor. Therefore, the selected reactor consisted of an absorber tube enclosed within a reflective cylindrical cavity, where the absorber tube is also the riser of a Circulating Fluidized Bed (CFB) where the calcination reaction proceeds.

The proposed model uses the calcination reaction kinetics proposed by Martinez et al. [53], the core-annulus heat transfer model, and a modified version of the K-L model of Kunii and Levenspiel [44]. The original K-L model is based on cold models, therefore, it was modified to account for the mass generation from the chemical reaction and the high temperature of the bed. The results showed that the gas velocity varied accordingly with the temperature increase of the bed and the variable mass flow rate of the gas. Furthermore, with the proposed model it was verified that assuming a constant density and constant mass flow rate, leads to an efficiency up to 8 % points over the one obtained with the proposed model. Therefore, it is necessary to consider the change of density of the gases with the increase of the temperature in the column, and the variation of the gas mass flow rate due to the chemical reaction.

The proposed model was implemented for two cases: (1) imposing a constant temperature of the reactor wall and (2) imposing a non-uniform flux distribution on the wall. In both cases, the bed temperature and the difference of the equilibrium concentration of CO_2 and its local concentration, proved to be the main driving forces of the reaction. A fraction of the height of the reactor was needed in both cases for heating the gas stream up to a point where the equilibrium concentration of CO_2 surpasses its local concentration. The needed height was 0.4 m and 1.3 m for cases 1 and 2 respectively. For a constant wall temperature, the needed height is much lower than in the case of the imposed flux. However, from experience, it is known that is highly unlikely to have a constant temperature on the receiver wall. Then, the control strategy of the solar field should be optimized to obtain a non-zero flux distribution on the base of the tube that allows decreasing the height of the reactor. This would result in some construction

implications during the building of the receiver, e.g. adding a second concentrator at the reactor base.

Regarding heat transfer, the constant wall temperature in case 1 allows a steady increase of the HTC and the temperature of the bed. In case 2 a variable wall temperature is achieved and the HTC reaches a maximum of 400 W m^{-2} K^{-1} at 4.5 m height where the bed temperature reaches momentarily 900 °C. This should be avoided to prevent the sintering of the sorbent by optimizing the control of the solar field.

It was concluded from the solids residence time profile and the molar calcination efficiency of case 1 that the required height of the reactor under the reference operating conditions was around 6 meters height as no significant improvement in the efficiency was achieved at higher heights. To depict this, the efficiency at 6 meters height was 0.65 while the efficiency at 10 m height was 0.69.

A sensitivity study was performed to analyze the influence of the inlet conditions and some model parameters for both cases. It was found that the decay factor affects greatly the solids velocity resulting in a great difference in the molar calcination efficiency found for the tested boundary cases. The variation of the height of the bed in an interval from 0 to 1 m did not show to be significant when compared to other parameters. Similarly, the effect of the particle size for the studied interval showed to be negligible.

As for the sensitivity study of the inlet parameters, the inlet temperature of the bed, and the initial concentration of CO_2 were the ones with stronger effects on the molar calcination efficiency. An increase in the inlet concentration of CO_2 results in a higher temperature of the bed needed for the calcination reaction to proceed. Therefore, when the final design of the calcium looping with the storage system is designed, it is necessary to consider the concentration of CO_2 resulting from the carbonation process.

As the purpose of this work is the use of CaL for TCES, it was necessary to study the effect of the inlet temperature of the bed to assess the need for preheating of the sorbents and the fluidizing gas. It was concluded that for the possible temperature range to be achieved while the products of the carbonator are stored, it is necessary to preheat the gas-solid flow to improve the efficiency. Similarly, a well-insulated storage system should be designed to decrease thermal losses from daytime to night-time.

The results showed that an increased fraction of CaO at the inlet, increased the molar calcination efficiency. This result might be misleading because in this case, the efficiency is increasing because there is a lower content of $CaCO_3$ entering the calciner and fewer sorbent available for calcination. Therefore, it would be beneficial to use enhanced sorbents as dolomite to minimize the deactivation of the sorbent and the mass fraction of CaO at the inlet.

The fraction of gas and solids mass flow rates at the inlet showed to be an important factor to consider to achieve complete calcination in the reactor. It was concluded that a ratio of at least 1.5 would be necessary to achieve complete calcination in a fast fluidization regime in the case of constant wall temperature. In the reference cases of this study, a ratio of 1 was being used. To increase the efficiency conserving the same ratio, it would be needed to decrease the mass flow rate of the gas and solid. However, a higher mass of solids could be calcined if the ratio is increased to 1.5 taking into consideration that the resulting gas velocity corresponds to the limits for low-density CFB. An additional

conclusion was found when assessing gas and solids mass flow rates ratio for case 2. The mass flow rate ratio is not only constrained by the achieved velocity of the gas but more important by the limiting sintering temperature and the maximum temperatures that the wall material can resist.

Other parameters were studied in the sensitivity analysis for the case where a non-uniform flux distribution is used. It was concluded that the results would be highly dependent on the aiming point and control strategy of the solar field. For the selected distribution, the temperature bed always reached the 900 °C which marks the limit where sintering of the sorbent increases. Therefore, it is necessary to optimize the solar field by using an aiming strategy that allows to homogenize the flux distribution spatially and to avoid the bed temperature to reach sintering temperatures. The results show that after 6 m height there is not a greater improvement of the molar calcination efficiency, nevertheless, the small increase occurs at the expense of the temperature of the bed.

The sensitivity study for the non-uniform heat flux showed that the effect of variating the decay factor, the gas mass flow rate and the mass fraction of CO_2 at the inlet resulted to be less significant than in case 1. The reason for this is that the peak of the flux is constrained to the first half of the reactor, where it is known that the variation of the results is not as significant as in the second half of the reactor where the temperature of the bed approaches the temperature of the wall for a significant reactor length. The results of the temperature of the bed again showed the importance of preheating the gas-solid flow. In this case, the effect on the calcination was much more significant than in the case of the constant wall temperature, i.e. 68 % point against 27 % respectively. For the flux distribution used, the calcination reaction did not proceed when the temperature of the bed at the inlet was at ambient conditions. Even though the effect of the variation of the mass fraction of CO_2 was not as significant as in case 1, this could be a result of the flux distribution selected for the analysis. The results might aggravate if a different aiming strategy is used, e.g. a flux distribution centered at the mid-height of the reactor. Therefore, it is necessary to optimize the aiming strategy accordingly to reduce the needed height for the reactor and to avoid hot-spots at the reactor wall.

The results of this master thesis show that the developed model is a tool that allows distinguishing critical issues to be considered while designing the concept proposed in this work for TCES in CSP systems. Its simplicity and fast computation time allow the user to obtain quick results while testing how different parameters could affect the performance of the reactor. This work is just the start of a project for designing and testing the CaL as TCES in CSP systems. Therefore, the limitations of this model and future research are presented in the following section.

5.1. Recommendations and Future Work

The calciner in CaL facilities nowadays uses oxy-combustion to provide heat to the reaction chamber. The additional combustion reactions of these setups do not allow the validation of the model presented in this thesis. Similarly, the usual approach for modeling the hydrodynamics is to use cold models that assume constant temperatures and mass flow rates. Therefore, it is advised to validate the proposed

model in an experimental setup alike to the one proposed. Special attention should be paid to the validation of the decay factor of the hydrodynamic model. This could be done by constructing a lab-scale reactor for high-temperature reactive systems and by measuring the pressure drop along with the height of the reactor. This will allow obtaining the solids volumetric fractions profile, therefore, allowing the validation of the hydrodynamics under these conditions.

Another limitation of the model is the assumption of a homogeneous temperature and heat flux on the polar plane. Even though it was a good start approximation, this is not expected in reality because the front part of the tube would receive most of the irradiation entering the cavity. Furthermore, Saade [80] modeled a similar geometry, i.e. a tube inside a cavity, and she concluded that most of the radiation hitting the reflective cavity exited the reactor without reaching the back of the tube. Therefore, there is an inhomogeneity to be considered that could be the subject of further work.

To allow that the current model accepts a non-homogeneous flux in the polar plane of the tube is necessary to divide each disc along with the vertical height into several wall arcs (Figure 42.a shows a scheme where the tube is divided into 2 parts). This will allow to input different fluxes at each discretized wall surface. Therefore, it would be necessary to add to the proposed model the conductive heat transfer between adjacent nodes, i.e. the nodes of the upper, lower, and lateral wall elements.

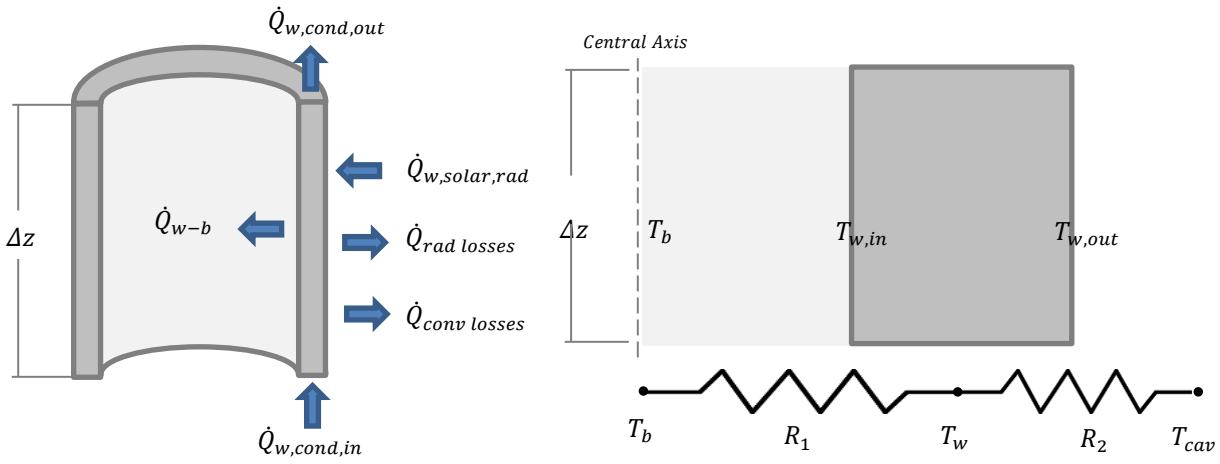

Figure 51. a) Discretization of the tube in the vertical and polar coordinates. The tube is divided into discs and the discs are divided into arcs of discs to properly input the distribution of the incident flux on the absorber wall. b) Nodes to be considered between the bed and the wall ($T_{w,in} \cong T_{w,out}$). Additionally, each wall element should take into account the conductive heat transfer between elements, both in the vertical and polar planes.

References

[1] K. Lovegrove and W. Stein, *Concentrating solar power technology*. 2012.

[2] C. Ortiz, J. M. Valverde, R. Chacartegui, L. A. Perez-Maqueda, and P. Giménez, “The Calcium-Looping (CaCO3/CaO) process for thermochemical energy storage in Concentrating Solar Power plants,” *Renewable and Sustainable Energy Reviews*, vol. 113. Pergamon, p. 109252, Oct. 2019, doi: 10.1016/j.rser.2019.109252.

[3] S. E. B. Edwards and V. Materić, “Calcium looping in solar power generation plants,” *Sol. Energy*, vol. 86, no. 9, pp. 2494–2503, 2012, doi: 10.1016/j.solener.2012.05.019.

[4] T. Hills and P. Lisbona, “SOCRATCES Project title : SOlar Calcium-looping integRAtion for Thermo- Chemical Energy Storage .,” 2020. [Online]. Available: https://socratces.eu/wp-content/uploads/SOCRATCES_D3.4_Solar-Calciner-Design.pdf.

[5] T. Hills and P. Lisbona, “SOCRATCES Project title : SOlar Calcium-looping integRAtion for Thermo- Chemical Energy Storage .,” no. 727348, pp. 1–35, 2020, [Online]. Available: https://socratces.eu/wp-content/uploads/SOCRATCES_D3.4_Solar-Calciner-Design.pdf.

[6] J. Petrasch and J. Klausner, “Integrated solar thermochemical cycles for energy storage and fuelproduction,” *WENE*, vol. 1, no. 3, pp. 347–361, Nov. 2012.

[7] G. Zsembinszki, A. Sole, C. Barreneche, C. Prieto, A. I. Fernández, and L. F. Cabeza, “Review of reactors with potential use in thermochemical energy storage in concentrated solar power plants,” *Energies*, vol. 11, no. 9, p. 2358, Sep. 2018, doi: 10.3390/en11092358.

[8] E. Alonso and M. Romero, “Review of experimental investigation on directly irradiated particles solar reactors,” *Renewable and Sustainable Energy Reviews*, vol. 41. Pergamon, pp. 53–67, Jan. 2015, doi: 10.1016/j.rser.2014.08.027.

[9] C. Tregambi, “Chemical storage of concentrated solar power.” 2016, [Online]. Available: https://www.semanticscholar.org/paper/Chemical-storage-of-concentrated-solar-power-Tregambi/cfe0ebd065688c77a677e2b6beffaf0474d354c9?p2df.

[10] A. Solé, I. Martorell, and L. F. Cabeza, “State of the art on gas-solid thermochemical energy storage systems and reactors for building applications,” *Renewable and Sustainable Energy Reviews*, vol. 47. Pergamon, pp. 386–398, Jul. 2015, doi: 10.1016/j.rser.2015.03.077.

[11] G. Flamant, D. Hernandez, C. Bonet, and J. P. Traverse, “Experimental aspects of the thermochemical conversion of solar energy; Decarbonation of CaCO3,” *Sol. Energy*, vol. 24, no. 4, pp. 385–395, Jan. 1980, doi: 10.1016/0038-092X(80)90301-1.

[12] R. A. Craig, “Investigating the use of Concentrated Solar Energy to Thermally Decompose Limestone,” 2010.

[13] V. Nikulshina, C. Gebald, and A. Steinfeld, “CO2 capture from atmospheric air via consecutive CaO-carbonation and CaCO3-calcination cycles in a fluidized-bed solar reactor,” *Chem. Eng. J.*, vol. 146, no. 2, pp. 244–248, Feb. 2009, doi: 10.1016/j.cej.2008.06.005.

[14] C. Tregambi, F. Montagnaro, P. Salatino, and R. Solimene, “Directly irradiated fluidized bed reactors for thermochemical processing and energy storage: Application to calcium looping,” in *AIP Conference Proceedings*, 2017, vol. 1850, p. 90007, doi: 10.1063/1.4984456.

[15] C. Tregambi *et al.*, “Directly irradiated fluidized bed reactor for thermochemical energy storage and solar fuels production,” *Powder Technol.*, vol. 366, pp. 460–469, Apr. 2020, doi: 10.1016/j.powtec.2020.02.045.

[16] T. Esence, H. Benoit, D. Poncin, M. Tessonneaud, and G. Flamant, “A shallow cross-flow fluidized-bed solar reactor for continuous calcination processes,” *Sol. Energy*, vol. 196, no.

August 2019, pp. 389–398, 2020, doi: 10.1016/j.solener.2019.12.029.

[17] H. Benoit, I. Pérez López, D. Gauthier, J. L. Sans, and G. Flamant, “On-sun demonstration of a 750°C heat transfer fluid for concentrating solar systems: Dense particle suspension in tube,” *Sol. Energy*, vol. 118, pp. 622–633, Aug. 2015, doi: 10.1016/j.solener.2015.06.007.

[18] A. Gallo, J. Spelling, M. Romero, and J. González-Aguilar, “Preliminary Design and Performance Analysis of a Multi-megawatt Scale Dense Particle Suspension Receiver,” in *Energy Procedia*, May 2015, vol. 69, pp. 388–397, doi: 10.1016/j.egypro.2015.03.045.

[19] X. Li *et al.*, “Hydrogen production of solar-driven steam gasification of sewage sludge in an indirectly irradiated fluidized-bed reactor,” *Appl. Energy*, vol. 261, p. 114229, Mar. 2020, doi: 10.1016/j.apenergy.2019.114229.

[20] J. M. Badie, C. Bonet, M. Faure, G. Flamant, R. Foro, and D. Hernandez, “52 Decarbonation of calcite and phosphate rock in solar chemical reactors.,” *Chem. Eng. Sci.*, vol. 35, no. 1–2, pp. 413–420, Jan. 1980, doi: 10.1016/0009-2509(80)80114-X.

[21] V. Nikulshina, M. Halmann, and A. Steinfeld, “Coproduction of syngas and lime by combined CaCO3-calcination and CH4-reforming using a particle-flow reactor driven by concentrated solar radiation,” *Energy and Fuels*, vol. 23, no. 12, pp. 6207–6212, Dec. 2009, doi: 10.1021/ef9007246.

[22] C. Tregambi *et al.*, “Jo ur l P re of,” 2020, doi: 10.1016/j.powtec.2020.02.045.

[23] C. K. Ho, “A review of high-temperature particle receivers for concentrating solar power,” *Applied Thermal Engineering*, vol. 109. Pergamon, pp. 958–969, Oct. 2016, doi: 10.1016/j.applthermaleng.2016.04.103.

[24] S. Abanades and L. André, “Design and demonstration of a high temperature solar-heated rotary tube reactor for continuous particles calcination,” *Appl. Energy*, vol. 212, pp. 1310–1320, Feb. 2018, doi: 10.1016/j.apenergy.2018.01.019.

[25] A. Steinfeld, A. Imhof, and D. Mischler, “Experimental investigation of an atmospheric-open cyclone solar reactor for solid-gas thermochemical reactions,” in *J. Sol. Energy Eng.*, Aug. 1992, vol. 114, no. 3, pp. 37–42.

[26] A. Imhof, “Decomposition of limestone in a solar reactor,” *Renew. Energy*, vol. 10, no. 2-3 SPEC. ISS., pp. 239–246, Feb. 1997, doi: 10.1016/0960-1481(96)88373-x.

[27] G. Moumin, S. Tescari, P. Sundarraj, L. de Oliveira, M. Roeb, and C. Sattler, “Solar treatment of cohesive particles in a directly irradiated rotary kiln,” *Sol. Energy*, vol. 182, pp. 480–490, Apr. 2019, doi: 10.1016/j.solener.2019.01.093.

[28] A. Imhof, “The cyclone reactor - an atmospheric open solar reactor,” *Sol. Energy Mater.*, vol. 24, no. 1–4, pp. 733–741, Dec. 1991, doi: 10.1016/0165-1633(91)90106-U.

[29] A. Meier, E. Bonaldi, G. M. Cella, W. Lipinski, D. Wuillemin, and R. Palumbo, “Design and experimental investigation of a horizontal rotary reactor for the solar thermal production of lime,” *Energy*, vol. 29, no. 5–6, pp. 811–821, Apr. 2004, doi: 10.1016/S0360-5442(03)00187-7.

[30] A. Meier, E. Bonaldi, G. M. Cella, W. Lipinski, and D. Wuillemin, “Solar chemical reactor technology for industrial production of lime,” *Sol. Energy*, vol. 80, no. 10, pp. 1355–1362, Oct. 2006, doi: 10.1016/j.solener.2005.05.017.

[31] E. Koepf, I. Alxneit, C. Wieckert, and A. Meier, “A review of high temperature solar driven reactor technology: 25 years of experience in research and development at the Paul Scherrer Institute,” *Appl. Energy*, vol. 188, pp. 620–651, 2017, doi: 10.1016/j.apenergy.2016.11.088.

[32] N. Piatkowski and A. Steinfeld, “Solar-driven coal gasification in a thermally irradiated packed-bed reactor,” *Energy and Fuels*, vol. 22, no. 3, pp. 2043–2052, May 2008, doi: 10.1021/ef800027c.

[33] Z. Sun and J. Zhu, “A consolidated flow regime map of upward gas fluidization,” *AIChE J.*, vol. 65, no. 9, pp. 1–15, 2019, doi: 10.1002/aic.16672.

[34] G. Jhon, “Contacting modes and behaviour classification of gas—solid and other two-phase suspensions,” doi: https://doi.org/10.1002/cjce.5450640301.

[35] B. Dingrong, “Flow regimes in circulating fluidized beds,” doi: https://doi.org/10.1002/ceat.270160505.

[36] M. E. Diego, I. Martínez, M. Alonso, B. Arias, and J. C. Abanades, *Calcium looping reactor design for fluidized-bed systems*. Elsevier, 2015.

[37] A. Charitos *et al.*, “Experimental validation of the calcium looping CO2 capture process with two circulating fluidized bed carbonator reactors,” *Ind. Eng. Chem. Res.*, vol. 50, no. 16, pp. 9685–9695, 2011, doi: 10.1021/ie200579f.

[38] A. M. Cormos and A. Simon, “Dynamic Modeling and Validation of Post-combustion Calcium-looping Process,” in *Computer Aided Chemical Engineering*, vol. 33, Elsevier B.V., 2014, pp. 1645–1650.

[39] A. R. Bidwe, “Hydrodynamic studies of the dual fluidized bed reactor systems for high temperature solid looping cycles,” 2017.

[40] D. P. Hanak, E. J. Anthony, and V. Manovic, “A review of developments in pilot-plant testing and modelling of calcium looping process for CO2 capture from power generation systems,” *Energy Environ. Sci.*, vol. 8, no. 8, pp. 2199–2249, 2015, doi: 10.1039/c5ee01228g.

[41] B. Arias, M. E. Diego, A. Méndez, M. Alonso, and J. C. Abanades, “Calcium looping performance under extreme oxy-fuel combustion conditions in the calciner,” *Fuel*, vol. 222, no. January, pp. 711–717, 2018, doi: 10.1016/j.fuel.2018.02.163.

[42] M. Helbig, J. Hilz, M. Haaf, A. Daikeler, J. Ströhle, and B. Epple, “Long-term Carbonate Looping Testing in a 1 MWth Pilot Plant with Hard Coal and Lignite,” *Energy Procedia*, vol. 114, no. November 2016, pp. 179–190, 2017, doi: 10.1016/j.egypro.2017.03.1160.

[43] A. A. Trendewicz, “Development of a Circulating Fluidized Bed.”

[44] Kunii and Levenspiel, *High-velocity fluidization.* 1991.

[45] D. Bai and K. Kato, “Quantitative estimation of solids holdups at dense and dilute regions of circulating fluidized beds,” *Powder Technol.*, vol. 101, no. 3, pp. 183–190, Mar. 1999, doi: 10.1016/S0032-5910(98)00159-4.

[46] R. C. Senior and C. Brereton, “Modelling of circulating fluidised-bed solids flow and distribution,” *Chem. Eng. Sci.*, vol. 47, no. 2, pp. 281–296, Feb. 1992, doi: 10.1016/0009-2509(92)80020-D.

[47] P. Kaushal and J. Abedi, “A simplified model for biomass pyrolysis in a fluidized bed reactor,” *J. Ind. Eng. Chem.*, vol. 16, no. 5, pp. 748–755, Sep. 2010, doi: 10.1016/j.jiec.2010.07.008.

[48] LUT, *Model Based Analysis of the Post- Combustion Calcium Looping Process for Carbon Dioxide Capture*. 2013.

[49] Q. Xue, D. Dalluge, T. J. Heindel, R. O. Fox, and R. C. Brown, “Experimental validation and CFD modeling study of biomass fast pyrolysis in fluidized-bed reactors,” *Fuel*, vol. 97, pp. 757–769, Jul. 2012, doi: 10.1016/j.fuel.2012.02.065.

[50] F. Sattari, M. Tahmasebpoor, J. M. Valverde, C. Ortiz, and M. Mohammadpourfard, “Modelling of a fluidized bed carbonator reactor for post-combustion CO2 capture considering bed hydrodynamics and sorbent characteristics,” *Chem. Eng. J.*, vol. 406, p. 126762, Feb. 2021, doi: 10.1016/j.cej.2020.126762.

[51] D. Kunii and O. Levenspiel, “The K-L reactor model for circulating fluidized beds,” *Chem. Eng. Sci.*, vol. 55, no. 20, pp. 4563–4570, 2000, doi: 10.1016/S0009-2509(00)00073-7.

[52] A. Błaszczuk, “Effect of flue gas recirculation on heat transfer in a supercritical circulating fluidized bed combustor,” *Arch. Thermodyn.*, vol. 36, no. 3, pp. 61–83, 2015, doi: 10.1515/aoter-2015-0022.

[53] I. Martínez, G. Grasa, R. Murillo, B. Arias, and J. C. Abanades, “Modelling the continuous calcination of CaCO3 in a Ca-looping system,” *Chem. Eng. J.*, vol. 215–216, pp. 174–181, 2013, doi: 10.1016/j.cej.2012.09.134.

[54] F. Fan, Z. S. Li, and N. S. Cai, “Experiment and modeling of CO2 capture from flue gses at high temperature in a fluidized bed reactor with ca-based sorbents,” *Energy and Fuels*, vol. 23, no. 1, pp. 207–216, 2009, doi: 10.1021/ef800474n.

[55] P. Rusheljuk, “Heat transfer in CFB,” pp. 167–174, 2006, [Online]. Available: https://pdfs.semanticscholar.org/bec3/40e68122fa8f67b0e1eca842d908523aaa74.pdf.

[56] J. C. Chen, J. R. Grace, and M. R. Golriz, “Heat transfer in fluidized beds: Design methods,” *Powder Technol.*, vol. 150, no. 2 SPEC. ISS., pp. 123–132, 2005, doi: 10.1016/j.powtec.2004.11.035.

[57] J. Li, Y. Tung, and M. Kwauk, “Energy Transport and Regime Transition in Particle-Fluid Two-Phase Flow,” in *Circulating Fluidized Bed Technology*, Elsevier, 1988, pp. 75–87.

[58] P. Basu, *Circulating fluidized bed boilers abroad*, vol. 54, no. 6. 2007.

[59] M. Q. Brewster, “Effective Absorptivity and Emissivity of Particulate Media With Application to a Fluidized Bed,” *J. Heat Transfer*, vol. 108, no. 3, pp. 710–713, Aug. 1986, doi: 10.1115/1.3247000.

[60] J. R. Grace, “HYDRODYNAMICS OF GAS FLUIDIZED BEDS,” in *Fluidized Bed Boilers*, Elsevier, 1984, pp. 13–30.

[61] A. Dutta and P. Basu, “An improved cluster-renewal model for the estimation of heat transfer coefficients on the furnace walls of commercial circulating fluidized bed boilers,” *J. Heat Transfer*, vol. 126, no. 6, pp. 1040–1043, 2004, doi: 10.1115/1.1833360.

[62] C. Moler, “Stiffness, ODE23s, ODE15s,” *MIT OpenCourseWare*. https://ocw.mit.edu/resources/res-18-009-learn-differential-equations-up-close-with-gilbert-strang-and-cleve-moler-fall-2015/solving-odes-in-matlab/stiffness-ode23s-ode15s/.

[63] C. W. Gear, *Numerical Initial Value Problems in Ordinary Differential Equations*. USA: Prentice Hall PTR, 1971.

[64] D. Level, E. Guillot, J. Sans, J. Ballestrin, and E. Guillot, “Comparisons of the spectral emissivity measurements at high temperatures of stainless steel AISI 310S,” *SFERA II Proj. FP7-INFRA-312643*, no. February, p. 32, 2014.

[65] H. Zhang *et al.*, “Particle circulation loops in solar energy capture and storage: Gas-solid flow and heat transfer considerations,” *Appl. Energy*, vol. 161, pp. 206–224, 2016, doi: 10.1016/j.apenergy.2015.10.005.

[66] T. E. Toolbox, “Emissivity Coefficient Materials.” https://www.engineeringtoolbox.com/emissivity-coefficients-d_447.html (accessed Dec. 20, 2020).

[67] M. Zeneli, A. Nikolopoulos, N. Nikolopoulos, P. Grammelis, S. Karellas, and E. Kakaras, “Simulation of the reacting flow within a pilot scale calciner by means of a three phase TFM model,” *Fuel Process. Technol.*, vol. 162, pp. 105–125, Jul. 2017, doi: 10.1016/j.fuproc.2017.03.032.

[68] A. Martínez, P. Lisbona, Y. Lara, and L. M. Romeo, “Carbonate looping cycle for CO2 capture: Hydrodynamic of complex CFB systems,” *Energy Procedia*, vol. 4, pp. 410–416, 2011, doi: 10.1016/j.egypro.2011.01.069.

[69] P. Teixeira, I. Mohamed, A. Fernandes, J. Silva, F. Ribeiro, and C. I. C. Pinheiro, “Enhancement of sintering resistance of CaO-based sorbents using industrial waste resources for Ca-looping in the cement industry,” *Sep. Purif. Technol.*, vol. 235, no. October 2019, p. 116190, 2020, doi: 10.1016/j.seppur.2019.116190.

[70] J. R. Fernandez, S. Turrado, and J. C. Abanades, “Calcination kinetics of cement raw meals under various CO 2 concentrations,” *J. Phys. Chem. C*, vol. 119, pp. 1623–1641, 2015, doi: 10.1039/c9re00361d.

[71] J. Xu *et al.*, “Effects of superficial gas velocity and static bed height on gas-solid flow characteristics in a 60-meter-high transparent CFB riser,” *Chem. Eng. J.*, vol. 334, no. September 2017, pp. 545–557, 2018, doi: 10.1016/j.cej.2017.09.131.

[72] F. J. Collado, “New one-dimensional hydrodynamics of circulating fluidized bed risers,” *Granul. Matter*, vol. 18, no. 4, pp. 1–14, 2016, doi: 10.1007/s10035-016-0674-5.

[73] H. M. Abdelmotalib, M. A. M. Youssef, A. A. Hassan, S. B. Youn, and I. T. Im, “Heat transfer process in gas-solid fluidized bed combustors: A review,” *International Journal of Heat and Mass Transfer*, vol. 89. Elsevier Ltd, pp. 567–575, Jun. 09, 2015, doi:

10.1016/j.ijheatmasstransfer.2015.05.085.

[74] A. Lasheras, J. Ströhle, A. Galloy, and B. Epple, “Carbonate looping process simulation using a 1D fluidized bed model for the carbonator,” *Int. J. Greenh. Gas Control*, vol. 5, no. 4, pp. 686–693, 2011, doi: 10.1016/j.ijggc.2011.01.005.

[75] F. Sattari, M. Tahmasebpoor, J. M. Valverde, C. Ortiz, and M. Mohammadpourfard, “Modelling of a fluidized bed carbonator reactor for post-combustion CO2 capture considering bed hydrodynamics and sorbent characteristics,” *Chem. Eng. J.*, vol. 406, no. August 2020, p. 126762, 2021, doi: 10.1016/j.cej.2020.126762.

[76] I. Martínez, G. Grasa, R. Murillo, B. Arias, and J. C. Abanades, “Kinetics of calcination of partially carbonated particles in a Ca-looping system for CO 2 capture,” *Energy and Fuels*, vol. 26, no. 2, pp. 1432–1440, 2012, doi: 10.1021/ef201525k.

[77] P. Teixeira, “Blending wastes of marble powder and dolomite sorbents for Calcium-Looping CO2 capture under realistic calcination conditions To Professor Sang-Eon Park.”

[78] M. Abreu, P. Teixeira, R. M. Filipe, L. Domingues, C. I. C. Pinheiro, and H. A. Matos, “Modeling the deactivation of CaO-based sorbents during multiple Ca-looping cycles for CO2 post-combustion capture,” *Comput. Chem. Eng.*, vol. 134, 2020, doi: 10.1016/j.compchemeng.2019.106679.

[79] M. Riaz and T. Gurr, “Solar flux density distributions on central tower receivers,” *Sol. Energy*, vol. 19, no. 2, pp. 185–194, 1977, doi: 10.1016/0038-092X(77)90057-3.

[80] M. E. Saade Saade, “MODEL PREDICTIVE CONTROL OF A SOLAR-THERMAL REACTOR,” University of Colorado, 2013.

[81] Y.-H. Kiang, “Other and emerging alternative energy technology,” in *Fuel Property Estimation and Combustion Process Characterization*, Academic Press, 2018, pp. 363–401.

[82] V. Nikulshina, D. Hirsch, M. Mazzotti, and A. Steinfeld, “CO2 capture from air and co-production of H2 via the Ca(OH)2-CaCO3 cycle using concentrated solar power-Thermodynamic analysis,” *Energy*, vol. 31, no. 12, pp. 1715–1725, Sep. 2006, doi: 10.1016/j.energy.2005.09.014.

[83] T. Melchior, C. Perkins, P. Lichty, A. W. Weimer, and A. Steinfeld, “Solar-driven biochar gasification in a particle-flow reactor,” *Chem. Eng. Process. Process Intensif.*, vol. 48, no. 8, pp. 1279–1287, Aug. 2009, doi: 10.1016/j.cep.2009.05.006.

[84] M. Neises, S. Tescari, L. de Oliveira, M. Roeb, C. Sattler, and B. Wong, “Solar-heated rotary kiln for thermochemical energy storage,” *Sol. Energy*, vol. 86, no. 10, pp. 3040–3048, Oct. 2012, doi: 10.1016/j.solener.2012.07.012.

[85] P. Haueter, S. Moeller, R. Palumbo, and A. Steinfeld, “The production of zinc by thermal dissociation of zinc oxide - Solar chemical reactor design,” *Sol. Energy*, vol. 67, no. 1–3, pp. 161–167, Jul. 1999, doi: 10.1016/s0038-092x(00)00037-2.

[86] W. C. Chueh *et al.*, “High-flux solar-driven thermochemical dissociation of CO2 and H2O using nonstoichiometric ceria,” *Science (80-.).*, vol. 330, no. 6012, pp. 1797–1801, Dec. 2010, doi: 10.1126/science.1197834.

[87] D. W. Gregg, R. W. Taylor, J. H. Campbell, J. R. Taylor, and A. Cotton, “Solar gasification of coal, activated carbon, coke and coal and biomass mixtures,” *Sol. Energy*, vol. 25, no. 4, pp. 353–364, Jan. 1980, doi: 10.1016/0038-092X(80)90347-3.

[88] M. Puig-Arnavat, E. A. Tora, J. C. Bruno, and A. Coronas, “State of the art on reactor designs for solar gasification of carbonaceous feedstock,” *Sol. Energy*, vol. 97, pp. 67–84, Nov. 2013, doi: 10.1016/j.solener.2013.08.001.

[89] Y. Yan, K. Wang, P. T. Clough, and E. J. Anthony, “Developments in calcium/chemical looping and metal oxide redox cycles for high-temperature thermochemical energy storage: A review,” *Fuel Processing Technology*, vol. 199. Elsevier, p. 106280, Mar. 2020, doi: 10.1016/j.fuproc.2019.106280.

[90] E. Koepf, S. G. Advani, A. Steinfeld, and A. K. Prasad, “A novel beam-down, gravity-fed, solar thermochemical receiver/reactor for direct solid particle decomposition: Design, modeling, and experimentation,” *Int. J. Hydrogen Energy*, vol. 37, no. 22, pp. 16871–16887, Nov. 2012, doi: 10.1016/j.ijhydene.2012.08.086.

[91] C. Wieckert, R. Palumbo, and U. Frommherz, “A two-cavity reactor for solar chemical processes: Heat transfer model and application to carbothermic reduction of ZnO,” *Energy*, vol. 29, no. 5–6, pp. 771–787, Apr. 2004, doi: 10.1016/S0360-5442(03)00183-X.

Annex

A.1 Classification based on the thermochemical material process

Zsembinszki et al. [7] suggest a classification that differentiates between two-phases reactions and solid decomposition due to heat (Figure 52).

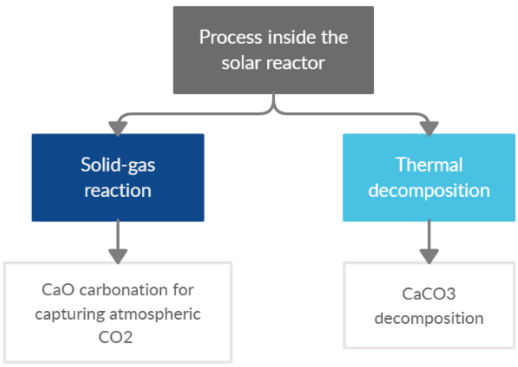

Figure 52. Classification according to the thermochemical material process.

A solid-gas reaction process is controlled by mass transfer by diffusion and can be separated into two diffusion stages: (1) the external diffusion, i.e., the diffusion from the gas to the solid surface, and (2) the internal diffusion, i.e., the diffusion from the surface of the solid to the inner part of the particle. On the other hand, in a thermal decomposition process, the reaction limiting step depends on the kinetics of the chemical reaction. The influence of diffusion and temperature difference within the particle on the reaction rate should be studied for each reaction to distinguish between a thermal decomposition process and a solid-gas reaction [7].

Understanding the reaction limiting process - if the reaction is chemically or diffusively controlled - is necessary for the reactor design. In this work, the focus is on the thermal decomposition reactions, thus this classification will not be used further.

A.2 Entrained bed reactors

Entrained bed reactors are based on creating a vortex inside the reactor by injecting the gas flow to a fixed angle that provides both horizontal and vertical velocity components. The particles then form a bed circulating around the vertical axis of the center of the reactor. In these reactors, the gases move up and solid particles move down. The advantages of this system are the high heat transfer coefficient and the possibility of being used both in continuous operation or batch mode. In counterpart, the main

disadvantage is the high sensitivity to the change in particle sizes [81].

Directly irradiated:

Imhof [25] designed an atmospheric open solar reactor to demonstrate the feasibility of the decomposition process of pure calcium carbonate with a particle size of 1-5 μm. The decision of designing an open cyclone reactor resulted from technical problems encountered with the quartz window needed in closed systems. The reactor is based on a cyclone gas separator design where the entrained particles are removed from the gas stream (

Figure 53). The particle and gas stream is injected into the system through a tangential slot. The gas stream creates a vortex with a high tangential velocity that creates a high centrifugal force that throws the particles to the cyclone wall where they descend to the bottom where the particles are removed. Then, the gas stream leaves the cyclone separator through the gas outlet duct. The reactor consisted of an open truncated cavity of 30 cm height in which inner walls were covered by a ceramic insulation layer. Below, two concentric cones form the space where the vortex develops and the gas is exhausted [8].

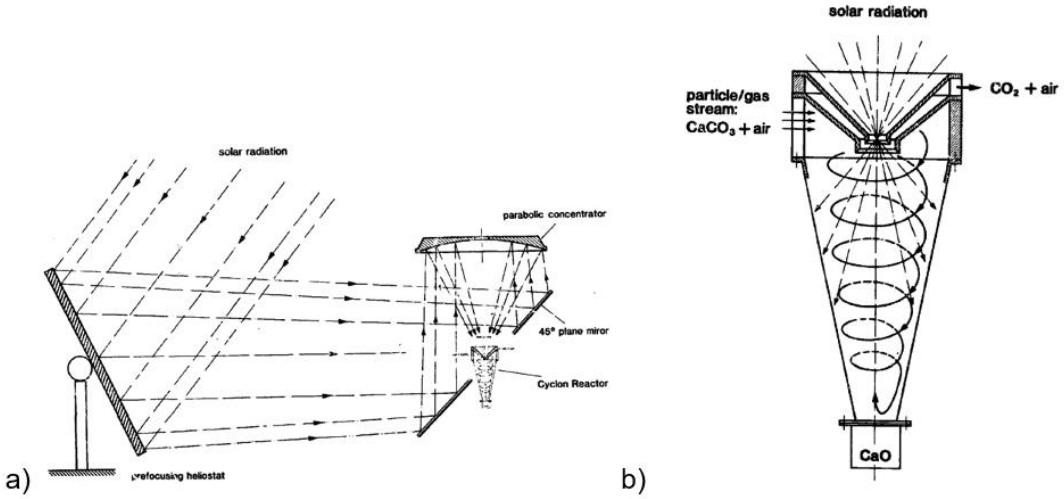

Figure 53. a) Setup of the solar furnace used in the experiment. b) Proposed design of the open cyclone reactor from Imhof [25].

Figure 54 shows the experimental setup that consisted of a gas and particle injection system, the solar reactor, a cyclone separator to collect solid products, and a heat exchanger to cool down the outlet gas stream. With this reactor design, it was possible to achieve a temperature of 1100 °C, a total efficiency of 43 % while reaching 53-94 % calcination degree [8].

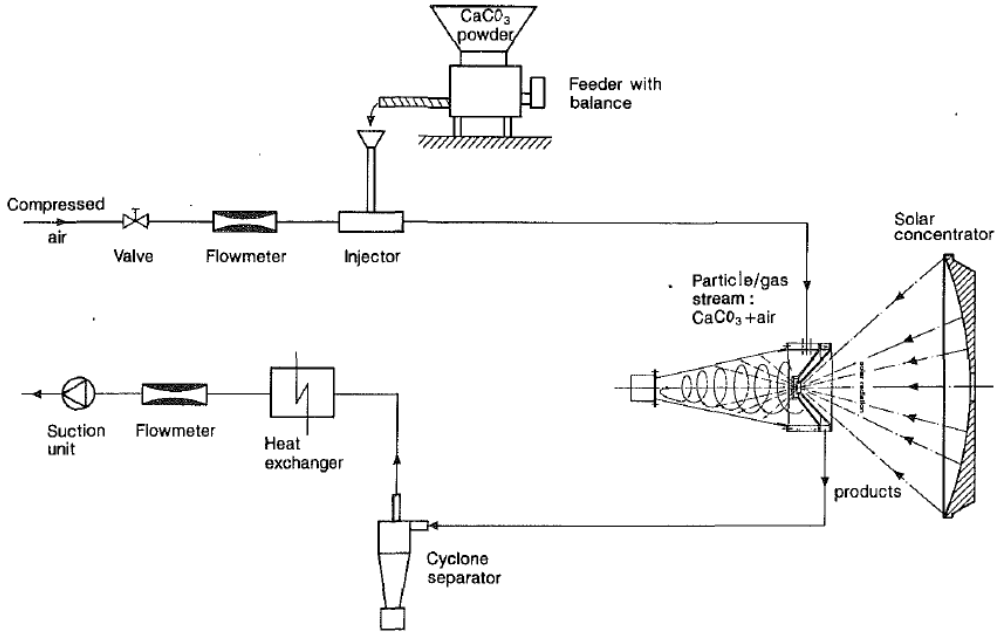

Figure 54. Experimental set-up scheme used at Paul Scherrer Institute (PSI) 17 kW solar furnace [25].

The author explains that the mean residence time of the fluidized particles must be sufficient to reach dissociation temperature. The kinetics of the thermal decomposition of limestone depends on the particle diameter, CO_2 partial pressure, and particle residence time. The open reactor proposed with low CO_2 concentration, 1100 °C, and around 100 µm particle diameter achieved a decomposition rate of 90 % for residence times of 55 s. To achieve a large variation in the particle residence time as a result of the poor optical properties of calcite for the absorption of concentrated irradiance, the author proposed the combination of the designed solar cyclone reactor with a fluidized bed reactor (Figure 55). This reactor design should be proper for processes with slow kinetics, i.e. long reaction times [28].

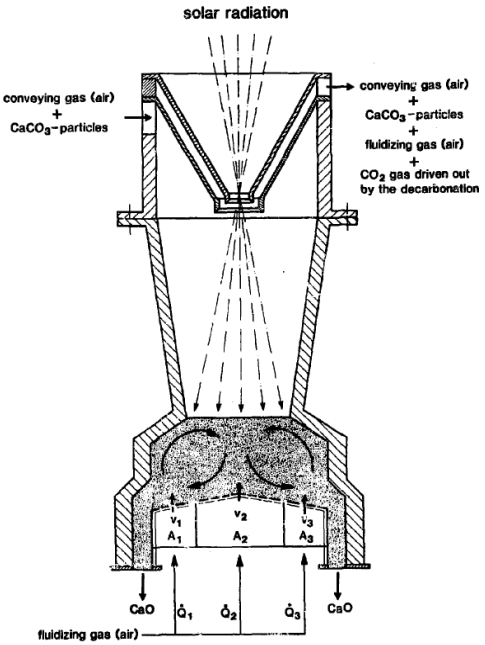

Figure 55. The proposed design combining a solar cyclone reactor and fluidized bed reactor from Imhof [25].

In later studies, Imhof et al. [26] changed the working principle of the reactor and its size was increased. The cyclone was placed vertically instead of horizontally and the irradiance entered from the bottom. The degree of calcination varied from 32-85 % with a thermal and chemical efficiency of up to 63 % and 15 % respectively.

Nikulshina et al. [82] analyzed a closed-material cycle for the capture of CO_2 from the air where a solar calciner for effecting the combined $CaCO_3$ decomposition and CH_4 reforming processes is one of the three reactors used in the cycle. The proposed reactor (Figure 56) for the combined calcination-reforming process uses a stream of CH_4 with $CaCO_3$ particles to create a vortex that is confined in the reactor cavity and that is directly exposed to the solar concentrated irradiance. The calciner operates at 1500 K and produces CaO and syngas.

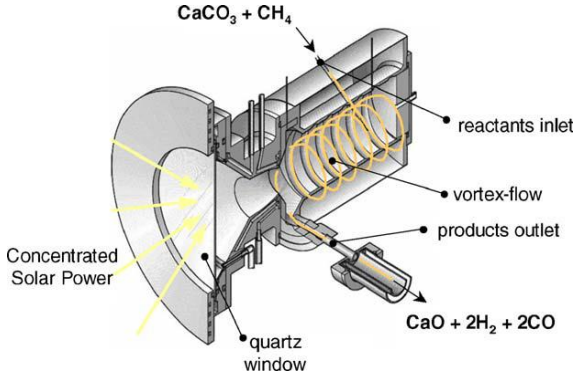

Figure 56. Schematics of the solar chemical reactor for the co-production of CaO and syngas from Nikulshina et al. [82].

Later in 2009, Nikulshina et al. [21] carried experimental tests on a 5 kW solar chemical reactor (Figure 57) achieve temperatures of 850 and 1145 °C with solar concentration up to 1884 suns. The chemical efficiency varied from 7-10 %, and the chemical conversion reached 83 % for $CaCO_3$ and 38 % for CH_4. The authors suggest that the design could be optimized by reducing the reradiation losses through the reactor aperture and conduction losses through the reactor insulation.

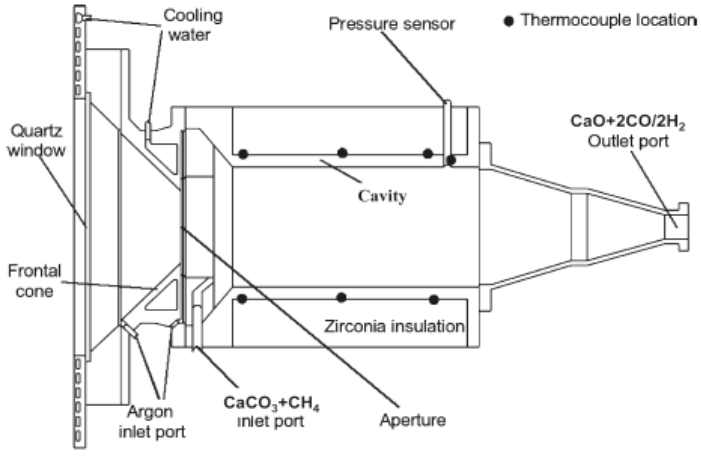

Figure 57. Cross-section of the directly irradiated solar reactor for the co-production of CaO and syngas from Nikulshina et al. [21].

Even though the SOCRATCES Project has not tested any reactor at a laboratory scale to the date where this review is written, it is worth to comment on an initial proposed design presented by Hills and Lisbona [4] on the deliverable D3.4 of the project. The authors proposed a beam-down receiver where the limestone is injected at an angle producing a cloud in the center of the receiver where is irradiated and heated up (Figure 58). By using a direct configuration, the walls of the receiver are likely to stay cooler making the receiver design simpler. However, to ensure the gas-tightness in the reactor is necessary the use of a quartz window at the aperture whose design is challenging due to two factors. Firstly, the thermal expansion coefficient of quartz is lower than that of steel which may cause stress at the connections as the reactor is heated up until the operating temperatures. Secondly, the particle fouling on the window would reduce the transparency of the window leading to inefficiencies. This could be solved by using a gas curtain, e.g. CO_2 could be used but it must be dedusted and compressed [4].

Other challenges of this design can be summarized as follows:

- This configuration is likely to have hotspots and coldspots through the cavity because the radiation of each heliostat enters the reactor on slightly different trajectories, even supposing that the secondary reflector reduces this effect to some extent. At hotspots, excessive sintering may occur while in coldspots incomplete calcination may happen leading to a reduction of the energy storage efficiency. This could be solved by introducing turbulence by gas injection or by using a conical cavity where the particles move in a helix down the reactor. Both solutions help to improve the mixing and distribution of the particles.
- Not enough residence time to achieve full calcination. This could be solved by using a splash plate or funnel in the path of the stream of limestone to increase the residence time by breaking the particle pathway and holding them for extra seconds [4].

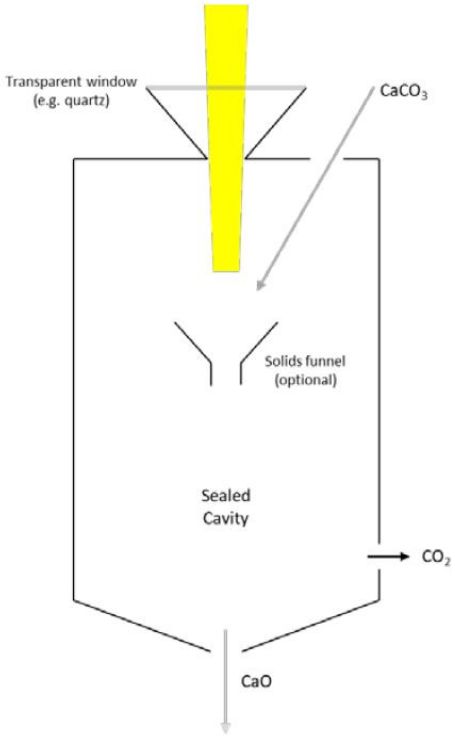

Figure 58. The direct irradiation solar calciner proposed by SOCRATCES [4].

Indirectly irradiated:

During the literature review, nine papers were consulted related to entrained flow solar reactors from which none referred to calcination using indirectly heated systems. An example of an indirectly irradiated entrained flow reactor is the work of Melchior et al. [83] who simulated and study experimentally the steam-gasification of biochar with concentrated solar radiation in a 3 kW solar reactor with a cylindrical cavity-receiver containing an opaque tubular absorber (Figure 59.a). Particles of beech charcoal are used as the biomass feedstock in a continuous steam-particle flow through the absorber. A simulation model coupling radiative, convective, and conductive heat transfer to the chemical kinetics was compared to experimental values of the temperature and carbon conversions. The same simulation was then applied to assess the performance of a scaled-up reactor of 8 absorber tubes (Figure 59.b) of 100 kW (case I) and 1M (case II) yielding chemical efficiencies of 39 % and 50 % for a mass flow rate of 250 g min^{-1} and 3250 g min^{-1} respectively. The temperature was not uniformly distributed in the absorber array. The closest tubes to the aperture showed the highest temperatures. The maximum temperature difference is 250 °C for the case I and 345 °C for case II. Conduction heat losses are reduced due to favorable volume to surface ratio. Reradiation losses through the aperture are the main source of losses.

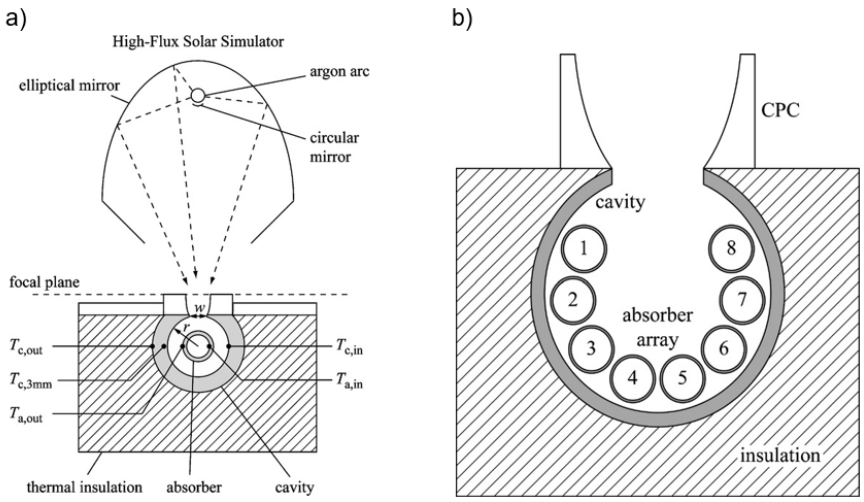

Figure 59. a) Schematics of the indirectly heated solar chemical reactor configuration. b) Schematics of the scale-up reactor containing 8 tubular absorbers from Melchior et al. [83].

Similar to indirectly heated fluidized bed reactors, the use of the indirect irradiated configuration may lead to a temperature difference among the absorber tubes. In this case, the temperature measured in each absorber tube varied based on their closeness to the aperture leading to differences in the degree of calcination among tubes.

A.3 Stacked bed reactors

Stacked bed reactors can be divided into fixed, mobile, and rotary reactors or kilns according to the classification reported by Alonso et al. [8]. Rotary reactors favor mass and heat transfer and are widely known from the experience of solid treatment using these reactors. Alternatively, fixed bed reactors are

those whose design, construction and operation are usually easier and more economic. They are normally used for preliminary laboratory tests to start studying a chemical process. Lastly, mobile bed reactors allow a better temperature distribution than fixed bed reactors and have the feature of continuous production mode that fixed bed reactors lack.

A.3.1 Rotary reactors or kilns

The working principle of solar rotary reactors is based on feeding the solid particles into a rotating receiver with an opening at the end of the vessel allowing the concentrated irradiance to enter. The rotating receiver creates a centrifugal force that moves the particles along the walls while they are irradiated [23]. Rotary reactors are widely used in many industrial processes as cement production and the food industry. This configuration requires a high amount of energy used to rotate the kiln [8].

Directly Irradiated:

Flamant et al. [11] proposed a solar rotary reactor with an inclination relative to the horizontal axis of 5 ° (Figure 60). The metallic frame of the reactor is cooled with water and rotates inside a fixed shell frame. The water cooling of the system allows measurement and control of heat losses to the wall. Inside this shell, there is an insulation layer followed by a wall made by refractory tubes of 0.09 m length and 0.024 m diameter. The particles are fed at the higher opening of the reactor and the concentrated solar rays enter through the opening at the end of the reactor. The total efficiency, considering the heating and the reaction, was between 7 and 15 % for a calcination degree from 30-60 %.

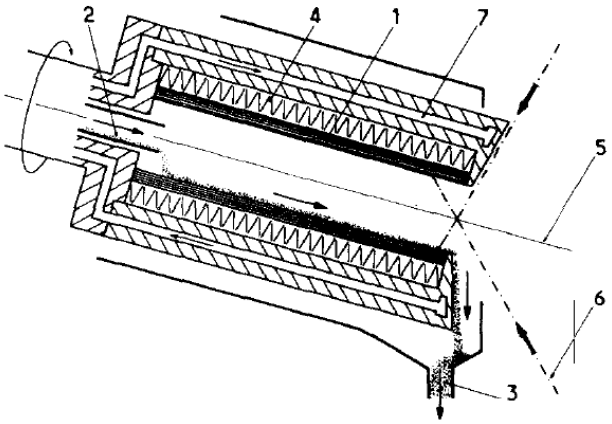

Figure 60. Scheme of solar rotary kiln. (1) refractory tube, (2) powder inlet, (3) powder outlet, (4) insulator, (5) axis of the kiln (may be tilted), (6) concentrated solar rays, and (7) water-cooled metallic shell from Flamant et al. [11].

Although not being a directly irradiated system, Badie et. al. [20] proposed a system optimization to the design of Flamant et al. [11] to enhance the kiln performance by distributing the heat inside the reactor more evenly. The enhancement consisted of using a stainless steel tube along the center axial line of the chamber. The tube was directly heated by the solar radiation, hence, the hot tube was the indirect heating source for the reactor. The authors concluded that the total efficiency was improved, however, no numbers were provided [20].

Meier et al. [29] proposed a horizontal rotary kiln reactor of 10 kW to produce high purity lime to assess the feasibility of the solar calcination process by performing experiments in a solar furnace at PSI. The small-scale prototype had a diameter of 350 mm and a length of 600 mm (Figure 61). Inside the horizontal reactor, there is a conical reaction chamber with 5 ° inclination. The reactants are preheated at the feeding side of the chamber and then transported through the conical reaction chamber until the discharging side at the front, where the concentrated solar radiation enters through an opening placed in the middle of a water-cooled aluminum front shield. The chamber is insulated with a porous ceramic fiber. Four rubber wheels, powered by an electric motor, drive the movement of the rotary kiln. The reactor operated for more than 100 h during 24 sunny days. The temperatures achieved was about 1150 °C and the degree of calcination exceeded 98 %. The reactor's chemical efficiency reached 20 % for solar flux inputs of 1200 kW m^{-2} and lime production rates of 1.3 kg h^{-1}. The authors suggested a design optimization to increase its efficiency by making design changes that enable to recover thermal energy from the products and reduce conduction heat losses through the reactor walls.

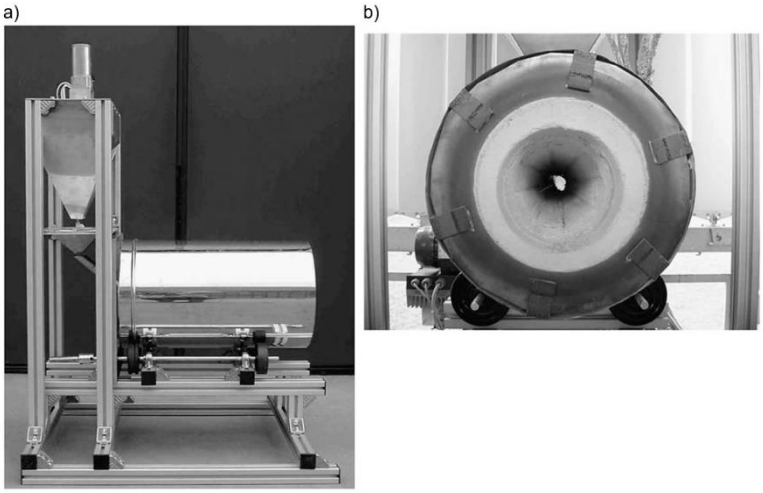

Figure 61. a) Set-up of the solar reactor showing the rotary drum and feeding system. b) The front view of the reaction chamber from Meier et al. [29].

During the literature review, fourteen papers related to rotary reactors were consulted from which seven papers were related to closed system configuration. Only one of those studied the calcination of $CaCO_3$, however, the experiment was stopped due to technical reasons. In detail, Moumin et al. [27] presented the design and experimental analysis of a solar rotary kiln to perform calcination of cement raw meal using two reactors configuration, an open and closed system. A distinction worth mentioning is that the raw meal used in cement production is constituted by cohesive particles in the form of powder, while other authors in this literature review use granular non-cohesive particles as reactants. The four components of the system are a screw feeder, the rotary kiln, the storage vessel, and the frame showed in Figure 62.

The closed system test was interrupted due to clogging issues in the suction system located at the reactor aperture. From the cold and hot test of this configuration, the authors concluded that good mixing and no dust deposition on the windows occurred during the cold test while during the hot state severe

deposition was noticed. The possible reason for deposition is the transport of fine particles by the reaction gas that evolves from the bed. It was noticed that during the feeding, the particles fall a short distance causing the formation of a dust cloud at the back of the kiln. The deposition of dust at the window was not avoided because of the clogging of the suction system, as can be seen in Figure 63. The authors state that a possible reason for clogging is the condensation of vapor inside the pipes given that the raw meal was not dried before feeding. Temperatures below 100 ° C were recorded close to the suction point. Additionally, the transmissivity of the window is reduced by 15 times due to the deposition of particles that absorbs the radiation and eventually could cause the window to melt. The improvement would be focused on changing the design of the feeding system and the gas extraction strategy [27].

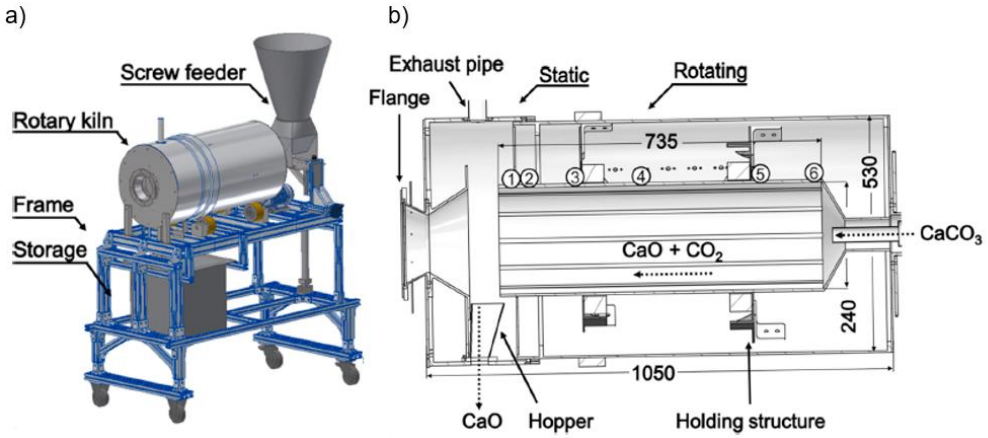

Figure 62. a) Sketch of the system and b) cross-section of the rotary kiln from Moumin et al. [27]. The solar irradiance enters through the flange.

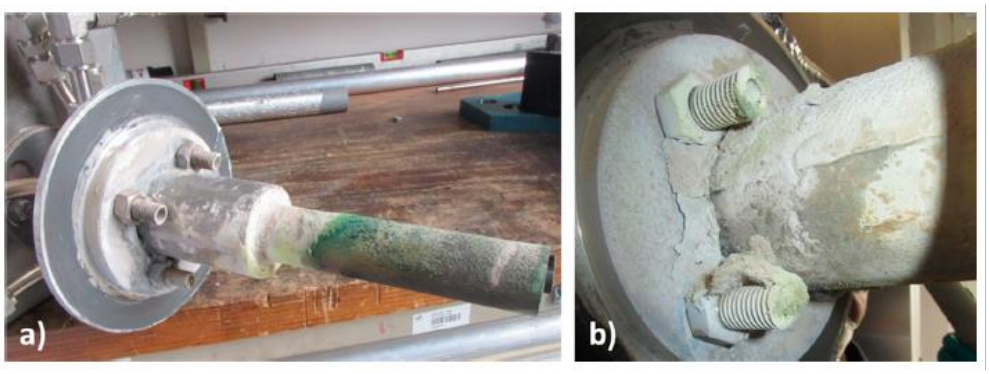

Figure 63. Suction system a) before and b) after the reactor's operation [27].

Contrarily, while testing the open configuration it was possible to finish the experiment. However, it is worth mentioning that the authors reported a visible cloud of dust that reflected part of the radiation. An outer suction system efficiently avoided the contamination of the room and the reactor's operation was possible. The calcination degree obtained ranged from 24-99 % for a rated flow of 4-12 kg h^{-1} and an input power of 14 kW. The total efficiency obtained was 19-40 %, i.e. chemical and thermal efficiency of 8-20 % and 11-20 % respectively. High temperatures result in the formation of layers due to sintering that improved the mixing of the bed. This allowed the uptake of heat into the inner part of the bed and the enhancement of the bed calcination. The authors claim that to optimize the system, the focus should

be on the rate of suction and mixing which depends on the bed height, inclination, and rotation speed inside the reactor [27].

The generation of dust and the difficulty of using a suction system that works effectively for keeping clear the window of closed rotary kilns could be the reasons why this configuration has not been further studied for limestone calcination by other authors. In contrast, the literature review showed that this configuration has been successfully used for solid oxide reduction-oxidation reactions. An example is the work of Neises et al. [84] who proposed a closed rotary reactor for the thermal reduction and oxidation of cobalt oxide which consisted of a silicon carbide cavity where radiation comes from a secondary concentrator mounted in front of the aperture of the reactor (Figure 64). A quartz window located at the entrance plane enables to work with adjustable compositions of the gas phase inside the chamber. The reactor is mounted on wheels and driven by a motor. The material was reduced at temperatures of about 900 °C, and a maximum chemical conversion for the reduction was 70 %. The author suggested that the achieved reduction of only half of the material was due to insufficient mixing of it. To improve the design, the authors advised: “to increase the particle mixing, avoid the particles loss with the gas stream, measure temperatures more accurately and analyze the behavior of the particles during the night period”. During the tests, the window remained transparent without the deposition of powder on it [8].

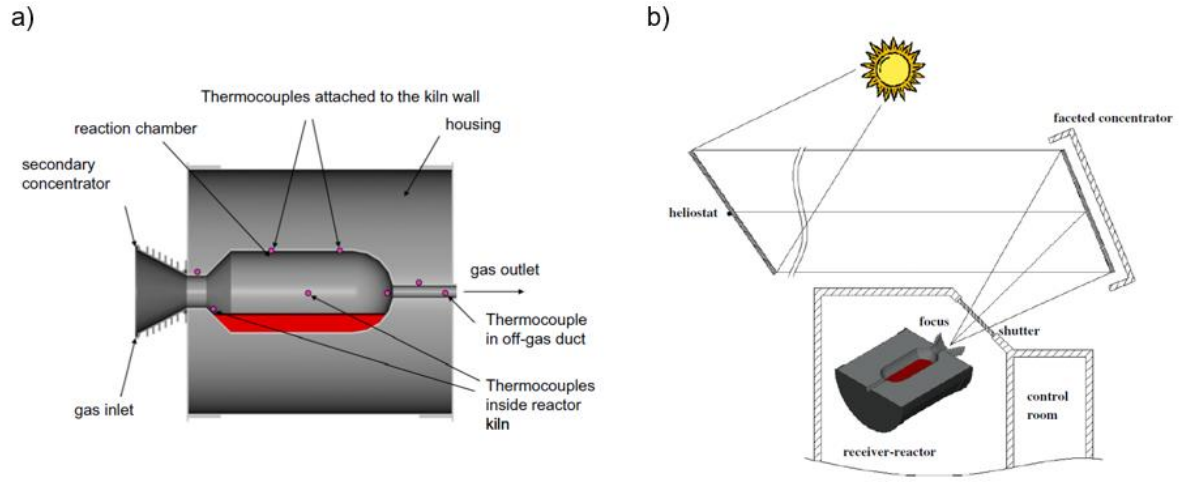

Figure 64. a) Schematic of the solar rotary kiln. b) Plant scheme in the solar furnace from Neises et al. [84].

Haueter et al. [85] tested a 10 kW rotary reactor to perform the thermal reduction of ZnO to Zn and O_2 (Figure 65). In the process, the oxide is decomposed into its elements at a temperature near 2000 K. The reactor consisted of a conical cavity with a small aperture that allowed the concentrated solar flux to enter through a water-cooled window. The reactants were fed through a screw powder at the end of the reactor and the gaseous products were removed using an inert gas flow entering tangentially at the front that also allowed to clear the particles from the window. The reactor operated at temperatures close to 2000 K with uniform distribution along with the reaction chamber and high resistance to thermal shocks [8].

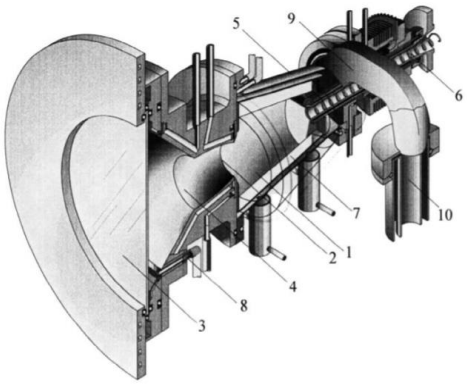

Figure 65. Schematic of the solar reactor for thermal decomposition of ZnO from Haueter et al. [85].

Indirectly Irradiated:

Meier et al. [30] proposed an indirect heating multi-tube rotary kiln for efficiently processing $CaCO_3$ particles and producing high purity CaO. The reactor scheme is depicted in Figure 66 and consists of a 10 kW rotary kiln with a multi-tube absorber and a preheating chamber. Temperatures of 1127 °C were reached with concentrated sunlight and limestone particles of 1-5 mm were efficiently calcined. The reactor's chemical efficiency was 30-35 % for solar flux inputs of about 2000 kW/m^2 and CaO production rates up to 4 kg h^{-1}. The authors stated that the efficiency of an industrial reactor would be higher if conduction losses are reduced and sensible heat is recovered for preheating the $CaCO_3$ particles. Thermal efficiencies of 45-55 % could be achieved.

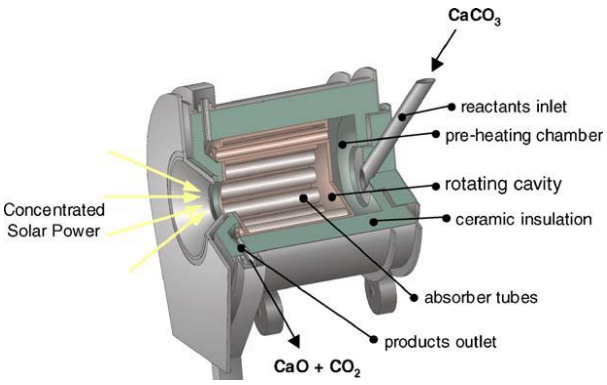

Figure 66. Schematics of the solar chemical reactor for thermal decomposition of $CaCO_3$ from Meier et al. [82].

Abanades and Andre [24] carried experiments on an indirectly heated rotary tube with a circular front aperture covered with a transparent hemispherical window that separates the cavity enclosure from the ambient atmosphere while letting solar radiation to enter the cavity (Figure 67). The separated cavity allowed to avoid the deposition of dust on the window. The authors reported no temperature gradient between the front and rear part of the tube. A high calcination degree up to 100 % was achieved for $CaCO_3$ particles size of 50-100 µm. The chemical efficiency was 10 % for a flow rate of up to 163 g h^{-1}.

a) b)

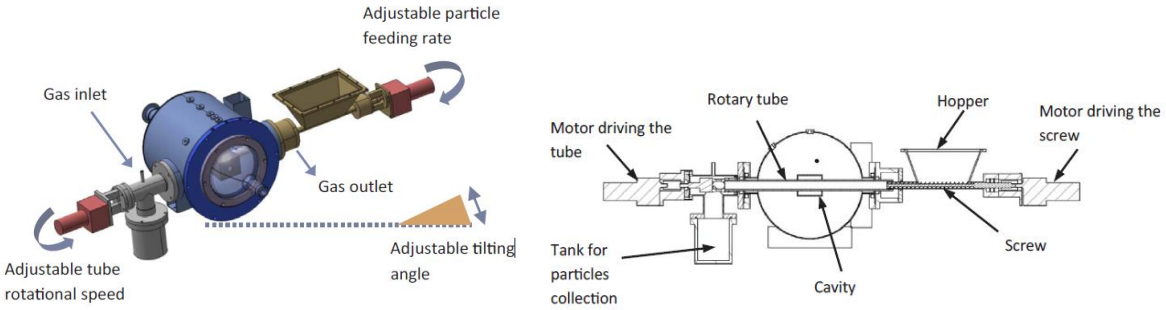

Figure 67. Reactor and feeding/collection system set-up: a) 3D and b) cross-section view from Abanades and Andre [24]. The hemispherical window separates the cavity enclosure from the ambient atmosphere while letting solar radiation to enter.

A.3.2 Fixed bed reactors

Alonso et al. [8] stated that there is a trend of using fixed bed reactors for preliminary laboratory tests to studying chemical processes. It is possible to measure the reaction temperature, to evaluate the interaction between reactants and radiation, and to develop parametric analysis and kinetic studies.

During the literature review, seven papers were consulted concerning solar fixed bed reactors from which none referred to $CaCO_3$ decomposition. Fixed bed reactors are characterized by a high thermal gradient that could lead to a non-homogeneous conversion of the reactant. Very high temperatures can be achieved on the surface while other areas do not reach reaction temperature [8]. Also, this type of reactor is not compatible with continuous operation and would require reloading of the feedstock after the $CaCO_3$ decomposition is complete [24], leading to thermal losses during cooling and heating stages before and after restocking.

Directly Irradiated:

Four papers related to closed fixed bed solar reactors were consulted from which none referred to calcination. The review showed that this configuration has been used for water-splitting for hydrogen production by thermal decomposition of zinc oxide, copper oxide, tin oxide, cerium oxide, among others. As an example, the work of Chueh et al. [86] proposed a fixed solar reactor for performing the thermochemical splitting of H_2O and CO_2 using cerium oxides. The reactor consists of a thermally insulated cavity receiver with a porous monolithic ceria cylinder (Figure 68). The solar flux enters at the top through a window and falls on the ceria wall. The reacting gas flows through the porous ceria wall to the inner cavity where the product gases are retrieved at the bottom. The generation of syngas was demonstrated over 500 cycles. Solar to fuel efficiency was 70-80 %

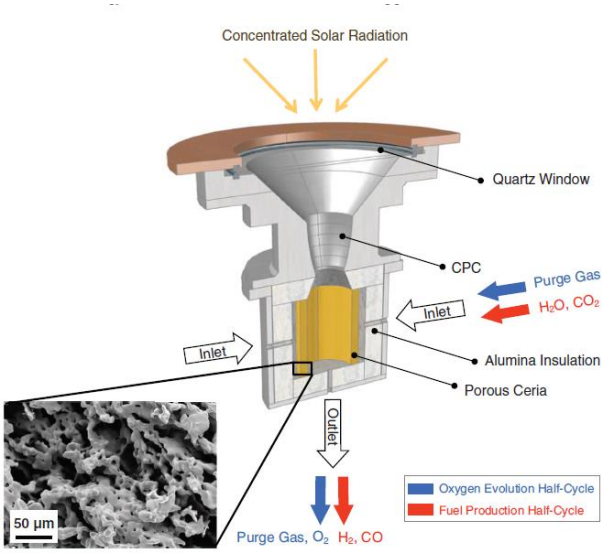

Figure 68. Schematic of a solar reactor for two-step water/carbon dioxide splitting from Chueh et al. [86].

Gregg et al. [87] studied the gasification of carbonaceous material in a packed bed gasifier. The reactor is an L-shaped tube of stainless steel where the feedstock is supplied by gravity (Figure 69). A silica window is placed at the short side of the L-shaped tube through which solar flux enters. Steam or CO_2 is injected through inlets close to the window and the outlet was placed at the top of the mixture. The maximum solar power input was 23 kW. The gas production rate of CO_2 gasification increased with solar power. The energy conversion efficiencies varied from 19-48 % for different solar powers [8].

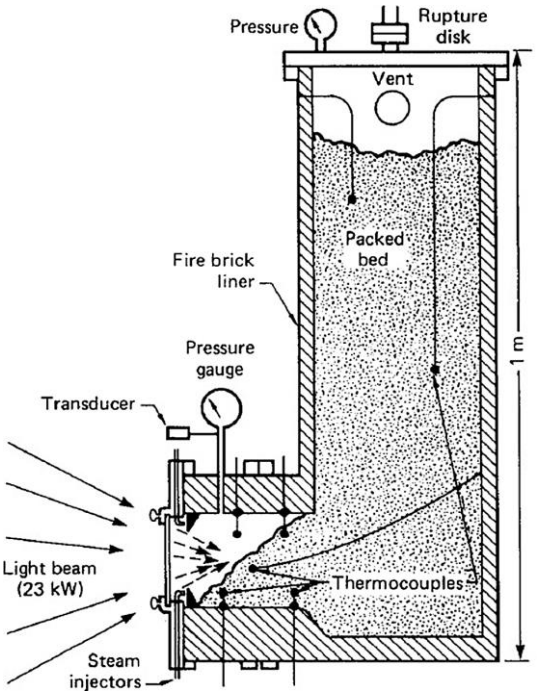

Figure 69. Packed-bed gasifier for carbonaceous material from Gregg et al. [87].

Indirectly Irradiated:

During this literature review, three papers related to indirectly heated fixed bed solar reactors were

consulted from which none referred to calcination. An example of an indirectly irradiated fixed bed reactor is the research of Piatkowski and Steinfeld [32] that designed and modeled an indirectly irradiated packed bed reactor of 5 kW consisting of two cavities separated by a radiant emitter plate (Figure 70). The upper cavity is the solar absorber and contains an aperture that allows the concentrated solar flux to enter. The lower one constitutes the reaction chamber where the bed lays. The packed bed temperature achieved 1440 K at a solar flux concentration of 2600 suns. The authors conclude that for steam gasification of coal the radiative heat transfer was the predominant mode of heat transportation and that for beds depths greater than 16 cm a higher average reaction rate is not produced [88].

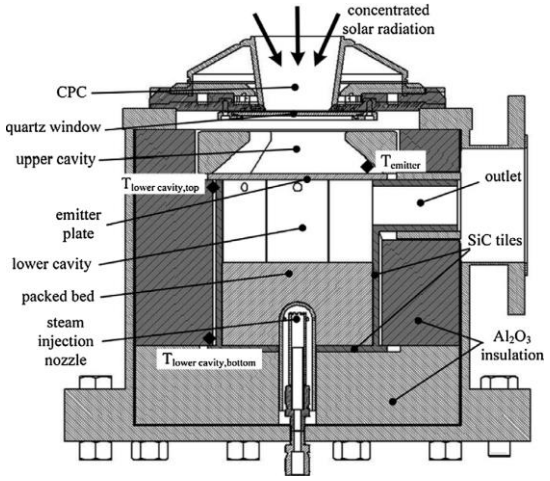

Figure 70. Cross-section view of the indirectly irradiated solar packed bed reactor from Piatkowski and Steinfeld [32].

A.3.3 Mobile bed reactors

Through the literature review, five papers were consulted related to moving bed reactors from which none referred to $CaCO_3$ decomposition. Mobile bed reactors have less impact of temperature difference than fixed beds and provide the characteristic of continuously removing particles. However, they are difficult to integrate with solar receivers leading to a non-uniform irradiance distribution on the particle flow [89].

Directly Irradiated:

From the reviewed literature, two experimental studies referred to closed directly irradiated mobile-bed reactors. An example of the use of this configuration is the work of Koepf et al. [90] who designed and tested a solar reactor for the thermal reduction of ZnO. The conical-shaped reactor is closed to the atmosphere with a quartz window (Figure 71). The surface of the cone serves to the reactant of particle size of 1 μm to descend continuously as a moving bed due to induced vibrations. After the dissociation of ZnO, the Zn product vapor flows downwards due to a vortex flow to an exit at the bottom of the cone. Experiments with high-flux solar simulator demonstrated the mechanical stability of the system achieved maximum temperatures of 1627 °C on the reaction surface.

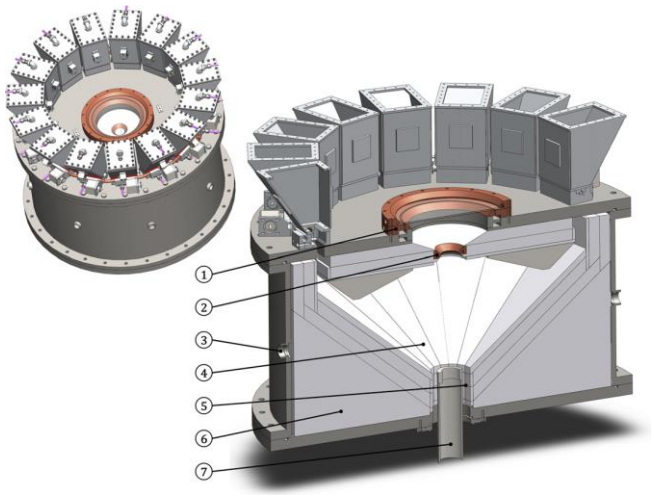

Figure 71. Moving bed reactor and cross-section (Gravity-Fed-Solar-Thermochemical Receiver/Reactor "GRAFSTRR"): (1) water-cooled window mount and vortex-flow generation, (2) water-cooled cavity aperture, (3) data-acquisition cavity access ports, (4) alumina-tile reaction surface, (5) annular solid ZnO exit, (6) bulk insulation, and cavity-shape support, and (7) central product-vapor and gas exit from Koepf et al. [90].

Even though the SOCRATCES Project has not tested any reactor at a laboratory scale to the date when this review is written, it is worth to comment on an initial proposed design presented in the project deliverable D3.4 [4]. The design consists of a long vibrating table that dispatch particles or powder of limestone through a preheating zone and then under a radiating plate where the particles calcinate. The radiating plate is the bottom of a cavity that is directly heated by the concentrated solar energy (Figure 72).

The hot CO_2 generated by the calcination reaction circulates along the preheating zone and out of the system to de-dusting and storage. The lime product continues its way beyond the radiating plate and falls into a storage system. This is possible by using a mechanical exciter that can be operated to control the residence time of the limestone. The authors highlighted that for this design it may be necessary to use particles with a larger diameter because the vibration of powders leads to their significant entrainment into the gas flows and their escape through the plate [4].

The challenges of this design can be summarized as follows:

- It is an untested design that is likely difficult to control.
- The thickness of the bed would be difficult to control. The less-dense CaO particles would tend to rise to the bed surface shielding the deeper particles in the bed. Managing to transfer enough heat to the lower particles would lead to the sintering of the upper ones.
- Possible agglomeration of particles [4].

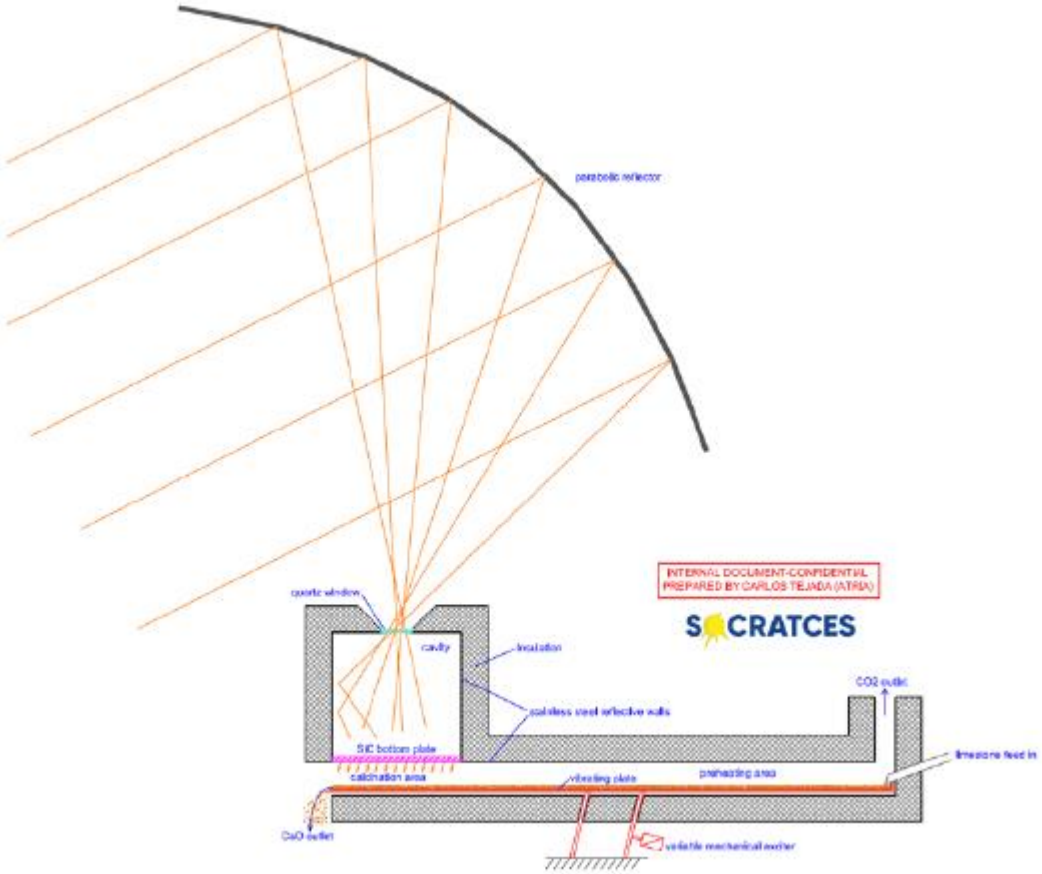

Figure 72. Vibrating table reactor design from the SOCRATCES Project [4].

Indirectly Irradiated:

Two papers from the literature review used indirectly heated mobile-bed solar reactors for the ZnO thermal reduction. An example is the work of Wieckert et al. [91] simulated and tested a 5 kW two-cavity beam-down reactor for the ZnO reduction with carbon. The concentrated sunlight enters at the top where the light is further concentrated using a compound parabolic concentrator before it goes through a quartz window at the top of the first cavity which is a cylinder closed on the end with the spherical shape made of graphite or SiC (Figure 73). At the second cavity, the ZnO/C mixture is fed using a screw feeder (10 g/min) and heated to the reaction temperature. The product gases exit the opposite side of the cavity that rotates at 7 rpm to distribute uniformly the reactants. The reactor achieved a chemical efficiency of 15 % when the solar flux entering the reactor was 1300 kW m^{-2} resulting in temperatures of 1227 °C. The thermal efficiency was 18 %.

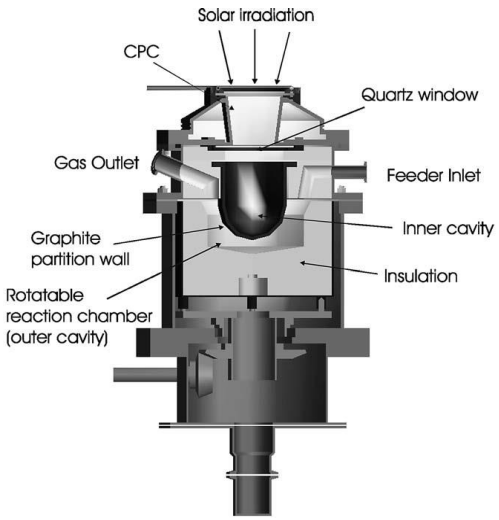

Figure 73. Two-cavity indirectly irradiated solar reactor from Wieckert et al. [91].

A similar configuration is used for the reactor design chosen by Hills and Lisbona [4] in the SOCRATCES project. In the final proposal, the limestone and the solar radiation are kept apart by modifying the design shown in Figure 58 with a windowless cavity which re-radiates the energy into the reactor chamber or annulus (Figure 74). The major challenge presented by the authors is distributing the radiation throughout the cavity. The first issue is the radiation leaving the aperture which will be the sum of a part of primary solar radiation and the radiation re-radiated by the cavity wall. Higher wall temperature implies higher heat losses through the aperture and less energy conducted to the reaction chamber. Hence a compromise most be held on the temperature of the cavity wall. Another constraint in the design would be the surface area of the cavity wall. The larger the area is for a given solar input, the cooler the wall will be. Concisely, the cavity geometry constraints limit the length of the reactor and thus the residence time of the limestone particles in the reactor. Despite the short residence time while using this configuration, this design was chosen to move forward with the next stages of the project.

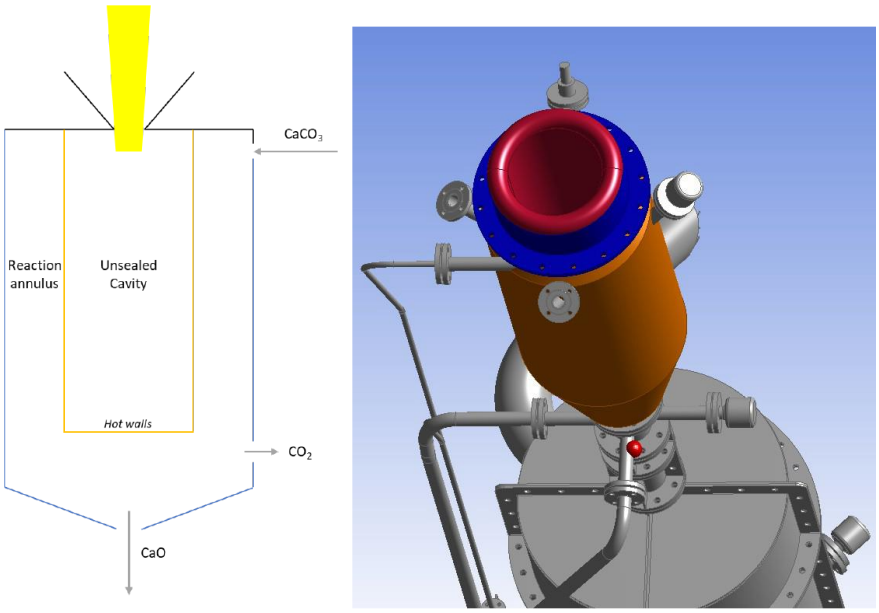

Figure 74. Sketch and isometric view of the indirect irradiation solar calciner reactor proposed by SOCRATCES [4].

A.4 Other Configurations

Hills and Lisbona [4] proposed six possible solar calciner designs from which four have already been discussed in previous sections. The following subsections aim to summarize the reasoning of the authors for rejecting the other two proposed designs.

A.4.1 Heat pipes reactor

This design employs heat pipes that contain a substance in vapor-liquid equilibrium. When heat is applied part of the liquid vaporizes and passes through the tube until the colder end where it condenses releasing its latent heat of vaporization. The authors propose to use sodium as the pipe fluid due to the aimed temperature, i.e. 900 ° C. Based on this concept two designs are proposed. The first employs receivers attached to the end of the heat tube (Figure 75). The slightly inclined tube passes through the calciner and then through a heat exchanger containing pipes for CO_2 and the heat transfer fluid. Then these gases are used in a turbine. In this design, a fraction of the heat could go straight until the heat exchanger being difficult to control the temperature inside the calciner. For this reason, a second design is proposed (Figure 75.b), where a beam-down central cavity is used for capturing the radiation [4].

The challenges of this design can be summarized as follows:

- Fouling would be a problem during calcination and carbonation.
- It is a very complex design with two sets of heat pipes which makes it difficult to scale down for testing.
- An aperture that well distributes the heat to the heat pipes is difficult to design due to shading [4].

a) b)

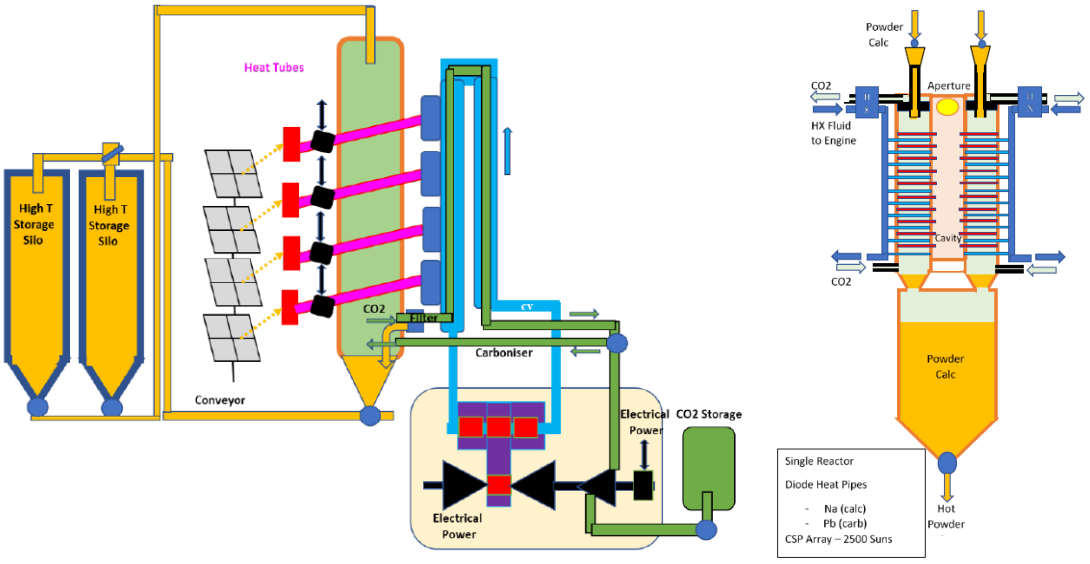

Figure 75. a) Calciner design with a single heat pipe array for calcination and carbonation. b) Dual heat pipe

calciner design. Designs proposed by SOCRATCES [4].

A.4.2 Hot CO_2 reactor

This reactor involves a volumetric receiver made with a ceramic foam that is irradiated (Figure 76). Then, the CO_2 is heated by being blown through the foam and further into the reactor to effect the limestone calcination. From the analysis, the authors concluded that:

- The amount of CO_2 needed to perform the calcination is large in volumetric terms leading to an increase in the reactor diameter.
- The receiver must reach 1200 ° C for heating the CO_2 to a proper temperature leading to high radiative losses. This could be overcome by reducing the surface area of the receiver or placing it in a cavity.
- The CO_2 must be conveyed using fans or blowers if more force is required. Even though fans are capable of operating at 1200 ° C the authors encounter it challenging finding valves and alike equipment that operates at that temperature [4].

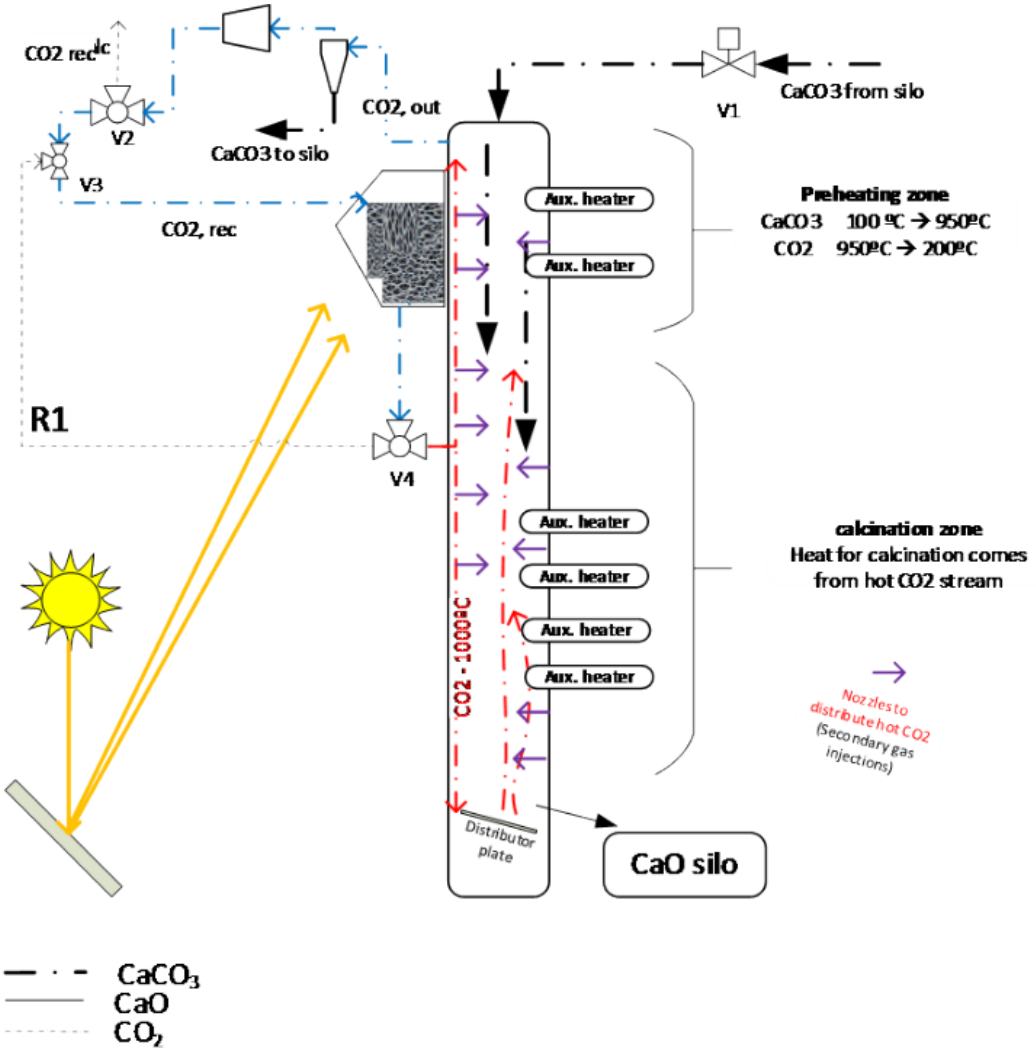

Figure 76. The hot CO_2 reactor proposed by SOCRATCES [4].

A.5 Useful identities

$$n_s = n_{CaCO_3} + n_{CaO} \tag{5.1}$$

$$m_s\ z\ = m_{CaCO_3}\ z\ + m_{CaO}\ z \tag{5.2}$$

$$c_s \equiv \frac{\delta n_s}{dV} = \frac{\delta n_{CaO}}{dV} + \frac{\delta n_{CaCO_3}}{dV} = c_{CaO} + c_{CaCO_3} \tag{5.3}$$

$$\varepsilon_g = \frac{dV_{gas}}{dV} \tag{5.4}$$

$$\varepsilon_s = \frac{dV_{solids}}{dV} = (1 - \varepsilon_g) \tag{5.5}$$

$$X_{CaO} \equiv \frac{n_{CaO}}{n_s} = \frac{c_{CaO}}{c_s} \tag{5.6}$$

$$X_{CaCO_3} \equiv \frac{n_{CaCO_3}}{n_s} = \frac{c_{CaCO_3}}{c_s} = 1 - X_{CaO} \tag{5.7}$$

$$m_a = \frac{\delta m_a U_a A}{dV} = \frac{\delta n_a M_a U_a A}{dV} \tag{5.8}$$

$$c_a = \frac{\delta n_a}{dV} = \frac{m_a}{M_a U_a A} \tag{5.9}$$

$$c_b = \frac{\delta n_b}{dV_g} = \frac{m_b}{M_b U_g A \varepsilon_g} \tag{5.10}$$

$$\frac{m_a}{m_b} = \frac{\frac{\delta m_a U_a A}{dV}}{\frac{\delta m_b U_b A}{dV}} = \frac{\delta m_a}{\delta m_b} \tag{5.11}$$

$$\frac{n_a}{n_b} = \frac{m_a}{m_b}\frac{M_b}{M_a} \tag{5.12}$$

$$\rho_{a+b} = \frac{\rho_a \rho_b}{(1 - \bar{X}_a)\rho_a + \bar{X}_a \rho_b} \tag{5.13}$$

$$\left[\frac{1}{\rho_{a+b}} = \frac{V_a + V_b}{m_a + m_b} = \frac{V_a}{m_a + m_b}\frac{m_a}{m_a} + \frac{V_b}{m_a + m_b}\frac{m_b}{b} = \frac{m_a}{m_a + m_b}\ \frac{1}{\rho_a} + \frac{m_b}{m_a + m_b}\ \frac{1}{\rho_b} = \frac{\bar{\bar{X}}_a}{\rho_a} + \frac{(1 - \bar{\bar{X}}_a)}{\rho_b}\right] \tag{5.14}$$

$$\bar{\bar{X}}_a = \frac{m_a}{m_a + m_b} = \frac{m_a}{m_a + m_b} \tag{5.15}$$

$$\rho_a = \frac{P}{R_a T} \tag{5.16}$$